Fabrication and Characterization of ZnO Related Materials

Thin Films for Optical Device Application

王大鵬

Dapeng Wang

A dissertation submitted to
Kochi University of Technology
in partial fulfillment of the requirements
for the degree of
Doctor of Philosophy

Special Course for International Students
Department of Electronic and Photonic System Engineering
Graduate School of Engineering
Kochi University of Technology
Kochi, Japan

March 2012

Fabrication and Characterization of ZnO Related Materials Thin Films for Optical Device Application

Dapeng Wang

Abstract

In this dissertation, the main work focus on the fabrication of zinc oxide (ZnO) related materials thin films (ZnO, ZnO:Mg) by using a radio frequency (RF) magnetron sputtering system for optical device applications. The influence of deposition parameters on the structural, electrical and optical properties of thin films was investigated. Based on thin film deposition technique, the novel post-treatment processes for the formation of nanostructured ZnO films were developed. As the demonstration, high quality ZnO thin film as the channel layer was applied into thin film transistors (TFTs). Nanostructured ZnO thin film as phosphor was demonstrated applies for vacuum fluorescent display (VFD). The main work and results of thesis will be exhibited by 7 chapters as follows.

Chapter 1 Introduction

The history background and current researches of ZnO material and thin films were investigated in detail. Based on the unique characteristics of ZnO, it is one of attractive candidates for optoelectronic applications. However, there are some remained issues for further commercial application. In order to solve these remained issues, the objectives of thesis were proposed and the outline of thesis was built.

Chapter 2 Fabrication equipment and characterization devices for ZnO thin films and nanostructures

The working principles, apparatus structures and parameters, and operation processes of fabrication equipment and characterization devices were introduced. ZnO related thin films with different deposition parameters were prepared by radio frequency magnetron sputtering system. The post-treatment processes were treated using commercial annealing furnace. Following the preparation of the samples, different characterization techniques were carried out to evaluate their structural and optical properties.

Chapter 3 Effects of deposition parameters on structural and optical properties of ZnO thin films

ZnO thin films were deposited onto quartz glass substrates by RF magnetron sputtering. The structural and optical properties of as-deposited ZnO films were strongly dependent on the deposition parameters including: Ar/O_2 ratio, applied power, and deposition pressure and substrate temperature. The Zn-rich or O-rich thin films can be adjusted simply by the modulation of Ar/O_2 ratio during sputtering. The film resistivity can be controlled with controlling the oxygen ratio. All the ZnO thin films show about 80% optical transmissions in the visible region. Based on the investigation of properties of ZnO films deposited under different sputtering parameters, the crystallinity and band gap of thin films can be adjusted simply as well.

Chapter 4 Fabrication and characterization of ZnO:Mg thin films

ZnMgO thin films with different Mg concentrations had been deposited on quartz or silicon substrates by using RF magnetron sputtering.

$Zn_{1-x}Mg_xO$ (x = 0.3) thin films were prepared under different deposition pressures. The crystal structure varied from hexagonal wurtzite to cubic rock-salt with decreasing deposition pressure from 9 to 1 Pa. Corresponding to the Mg concentration in the ZnMgO thin films increased due to the scattering effect. Furthermore, the band gap of the ZnMgO films increased significantly from 4.30 to 5.23 eV while the deposition pressure decreased.

$Zn_{1-x}Mg_xO$ (x = 0.1) thin film was deposited on p-type Si (100) substrate and then annealed in H_2/N_2, N_2, or O_2 ambient in a commercial furnace. The most improved crystallinity was found from the film annealed in H_2/N_2 ambient, corresponding to the increased grain size. Moreover, the PL intensity with peak range around 520-620 nm was increased remarkably for the film annealed in reducing gas.

$Zn_{1-x}Mg_xO/ZnO$ (x = 0.1) thin film were prepared on p-type Si (100) substrate with ZnO thin film as buffer layer. The hexagonal naorods were formed vertically on the ZnMgO after annealing in a reducing ambient at a low temperature. The crystallinity of ZnMgO/ZnO was improved due to Mg substitution in the ZnO film. A broaden PL emission peak from 480 to 700 nm was observed from ZnMgO/ZnO multiple layers.

Chapter 5 Fabrication and characterization of nanostructured ZnO thin films

Based on ZnO thin films fabrication, the novel post-treatment processes were carried out on forming nanostructured ZnO thin films. The effects of different post-treatment processes on the structural and optical properties on nanostructured ZnO thin films were investigated.

Nanostructured ZnO thin films were formed by optimizing the post-treatment time in reducing gas. The intense green emission is obtained from the ZnO nanostructures annealed for

the optimum annealing time of 5 h with a suitable gas ratio and temperature. Therefore, it can assume that the much more oxygen vacancies might be produced by reducing annealing and ZnO nanostructures supplied a larger area for oxygen vacancies existed.

ZnO nanorods from different thickness films were formed by annealing ZnO films in reducing ambient at a low temperature. The quantity of ZnO nanorods increased with the thickness increased, which was due to the quantity of un-react zinc atoms introduced by deposition process. PL spectra obtained from annealed films exhibited an intense deep level emission with a peak centered at about 500 nm. The strongest green luminescence was observed from the annealed film with the thickness of 1000 nm, which was attributed to the dense ZnO nanostructures which supplies much larger surface area where more oxygen vacancies existed.

A novel low-temperature multi-annealing process was proposed for forming well-arrayed ZnO nanostructures, which combines a reducing annealing process and oxygen annealing process. Well-arrayed ZnO nanostructures with the appearance of fluted reverse cones capped with hexagonal heads were obtained via a novel multi-annealing process. Oxygen annealing between the two reducing gas annealing processes contributed to efficiently introduce the oxygen into the ZnO thin films, leading to ZnO nanostructures regrown quickly.

Based on the results exhibited above, the optimized annealing time of first reducing annealing step in multi-annealing processes was investigated. The optimized condition for form the nanostructure was found for the annealing in reducing ambient first for 5 h. The ZnO nanostructures with uniform hexagonal head with diameter of 600 nm and average height of 1200 nm were formed after multi-step annealing. The intense PL emission peak centered at 505 nm was obtained from the well-arrayed ZnO nanostructures.

Chapter 6 Applications

Two kinds of potential applications were investigated based on the ZnO material. The research background and current researches of thin-film-transistors (TFTs) and vacuum fluorescent display (VFD) were studied in detail. ZnO thin film as the channel layer was applied into TFTs. Nanostructured ZnO thin film as phosphor was potentially applied for VFD application. The operation parameters and results were evaluated on above mentioned ZnO-related applications.

Chapter 7 Conclusions and outlook

The main results obtained from this research work are summarized.

Acknowledgements

List of Figures

List of Tables

Chapter 1: Introduction

Chapter 2: Fabrication equipment and characterization devices for ZnO thin films and nanostructures

Chapter 3: Effects of deposition parameters on structural and optical properties of ZnO thin films

Chapter 4: Fabrication and characterization of ZnO:Mg thin films

Chapter 5: Fabrication and characterization of nanostructured ZnO thin films

Acknowledgements

First of all, I would like to express my sincere appreciate to my supervisor Prof. Tadashi Narusawa for his guidance and supports during my Ph.D. study and research. Thank you for offering me the opportunity to study in KUT and great encouragement in my whole research work. It is my honor to be your student and I am proud of it.

I want to give my special thanks to my vice-supervisor Associate Prof. Chaoyang Li who drags me into the scientific world and keeps encouraging me both on life and science, and makes it possible when I celebrate my research achievement every time. She is considered not only as a teacher but also a family member. I will never forget what I learned from her, which will benefit my entire life.

I would like to thanks to my co-supervisor Prof. Mamoru Furuta for supporting me in the past and coming years and giving me much more effective suggestions and helps on TFTs study.

I also want to thanks my co-supervisor Prof. Takashi Hirao for offering me the chance to study in Institute of Nano-devices, Kochi University of Technology.

I would like to thanks my co-supervisor Prof. Akimitsu Hatta for his kind-hearted encouragement and instructive advices.

My sincere thanks also extend to the members in Institute of Nano-devices, to Dr. Toshiyuki Kawaharamura for his much advice in my daily research and always share his experiences with me. To other members, Associate Prof. Hiroshi Furuta, Dr. Tokiyoshi Matsuda, and Dr. Takahiro Hiramatsu, for teaching me device principle and operation.

For the SSP fellows, I cherish the great periods and the friendship with all of you.

Last but not least, I so appreciate my parents and my dear wife for their endless supporting and love and everything you have done for me. Thank you so much.

Caption of Figures

Caption of Tables

Chapter 1

Introduction

1.1 The overview of zinc oxide material

1.1.1 Background of study on zinc oxide

There is no denying that semiconductors changed the world beyond anything that could have been imagined before them. As early as in 1782, the term “semiconducting” was firstly introduced by Alessandro Volta [1]. Up to 1833, Michael Faraday observed the semiconductor effect that the resistance of silver sulfide decreased with the temperature, which was different than that of in metals [2]. Since then, the semiconductor industry has spread every corner in the world and blossomed into the daily life of human being.

The research history, with peaks occurring from time to time, is documented apart from many scientific publications by a great deal of review papers and books. As a typical II-VI compound semiconductor, the bulk zinc oxide (ZnO) crystal has been investigated extensively as early as in 1950’s. The electrical and optical properties of ZnO had been studied extensively [3,4] such as the stubborn n-type conductivity, showing absorption spectra, electroluminescence decay parameters, and so forth. In the mid 1960’s the first period of notable growth in ZnO research occurred with a series of highly-cited theoretical and characterization works. Laudise et al [5] reported that large (10 to 20 g) macroscopically sound ZnO crystals suitable for preliminary transducer and other studies have been grown hydrothermally. The topics of research and development are partly the same as in the 1970s and 1980s, such as growth, doping, linear and nonlinear optics, including the aspects of stimulated emission. In the 1970’s the manufacture and characterization of simpler ZnO devices were mainly concentrated [6,7]. In the 1980’s many growth procedures were examined in the quest for high-quality ZnO thin films [8] such as metal-organic chemical vapor deposition (MOCVD), spray pyrolysis, radio-frequency (RF) magnetron sputtering. In the 1990’s, the researchers mainly worked toward fabricating high-purity bulk ZnO wafers and had success in 1998 with the vapor phase transport growth method.

From 2000’s the researchers focused mainly on ZnO growth mechanisms and parameters for further device applications. It is well-known that ZnO can be applied into a variety of fields, such as medical and cosmetic, concrete industry, rubber manufacture, ceramic and glasses, electronic materials, paints and pigment, catalyst and so on. Among the mentioned above, the

electronic materials application is most popular one, which includes phosphor [9-11], solar cell [12-14], conductive film [15-18], light emission display (LED) [19-21] and thin film transistors (TFTs) [22-26]. Furthermore, ZnO is an attractive material for applications in electronics, photonics, acoustics, sensing, and so on. In the case of optical emitters, its high exciton binding energy (60 meV) gives ZnO an edge over other semiconductors such as GaN if reproducible and reliable p-type doping in ZnO were achieved, which currently remains to be the main obstacle for realization of bipolar devices. However, epitaxial layers and single crystals are the important for development of optoelectronic such as blue and ultraviolet light emitters and detectors, piezoelectric and spintronic devices, and combine with GaN for light source. On the electronic side, ZnO has some potential advantages in transparent thin film transistors (TFTs) due to its high optical transitivity, high conductivity and not degradation on exposure to visible light due to the wide band gap of ZnO. The other promising fields of application for ZnO are acoustic wave devices due to large electromechanical coupling of ZnO, and devices together with nanostructures such as biosensors, gas sensors and solar cells, since it is relatively easy to produce such forms of ZnO nanostructures, which have good charge carrier transport properties and high crystalline quality. Based on its performance and applications, we can say that ZnO is an essential material and has penetrated and spread to all aspects of life.

1.1.2 Properties of zinc oxide

At ambient temperature and temperature, the stable phase of ZnO is wurtzite structure, as shown in Fig. 1.1. The structure of ZnO can be treated as a number of two type planes which interpenetrate sub-lattices of Zn^{2+} and O^{2-}, such that each Zn ion is surrounded by a tetrahedral of ions, and vice-versa. The type of tetrahedral coordination in ZnO gives rise to a noncentral symmetric structure with polar symmetry along the hexagonal axis. This polarity not only induces the characteristic piezoelectricity and spontaneous polarization, but also plays a part in crystal growth, etching and defect generation. The hexagonal lattice of ZnO belongs to the space group P63mc with lattice parameters of a = 3.250 and c = 5.207 Å [27]. The Table 1 lists the basic physical parameters of bulk ZnO.

In addition to the wurtzite phase, the crystal structures of ZnO are also shared by cubic zinc blende and rocksalt (NaCl) structures [28]. The zinc-blende ZnO structure can be stabilized only by growth on cubic substrates, while the rocksalt structure may be obtained at relatively high pressures at ~10 GPa. Theoretical calculations indicate that a fourth phase, cubic caesium chloride, may be possible at extremely high temperatures, however, this phase has yet to be experimentally observed [29].

The band structure of a semiconductor is critical to determine its potential utility. Furthermore,

an accurate understanding of the band structure is very important for its related device applications. So far, several theoretical approaches of varying degrees of complexity, such as Local Density Approximation (LDA) [30], First-principles (FP) [31], and incorporating atomic self-interaction corrected pseudopotentials (SIC-PP) [32], have been performed to calculate the band structure of wurtzise ZnO. The band gap of ZnO (3.37 eV) is determined from above-mentioned methods.

For commercial applications of ZnO-based semiconductors, particularly in optoelectronic devices, an important issue is the realization of band gap engineering in a wide range. One can modulate the band gap of ZnO by alloying it with a semiconductor (Mg, Cd, S, Se, Te and so on) that has a different band gap to form a ternary compound [33-37]. The energy band gap can be increased or decreased by means of alloying with MgO and CdO, respectively.

The mechanical properties of materials involve various concepts such as hardness, stiffness, and piezoelectric constants, Young's and bulk moduli, and yield strength. ZnO is a relatively soft material with a hardness of about 5 GPa at a plastic penetration depth of 300 nm [38]. The nanoindentation method is widely used for probing the mechanical properties of ZnO over a wide range of size scales and temperatures, which indicate the information on the behavior of a material under contact induced damage. The depth-sensing indentation measurements provide the complete information on the hardness and pressure-induced phase transformation of ZnO material. Piezoelectricity is also one of crucial mechanical property. ZnO piezoelectric tensor is believed to equal to or even greater than that of GaN and AlN, which indicate that ZnO is a potential candidate for a large electromechanical coupling applications [39].

ZnO has plenty of attractive advantages in electrical properties associated with a large band gap include higher breakdown voltages, ability to sustain large electric fields, lower noise generation, and high-temperature and high-power operation. The carrier concentration of ZnO varies a lot but is usually within the range of 10^{15}-10^{17} cm^{-3}. The largest reported *n*-type doping is ~10^{20} electrons/cm^3 and the largest reported *p*-type doping is ~10^{19} holes/cm^3. However, the high levels of *p*-conductivity are questionable and have not been experimentally verified. The exciton binding energy is 60 meV at room temperature, which is one of the reasons for ZnO optoelectronic device applications. The electron Hall mobility at room temperature for low *n*-type conductivity is ~200 $cm^2V^{-1}s^{-1}$, and for low *p*-type conductivity is in the range of 5-50 $cm^2V^{-1}s^{-1}$ [40].

It is well-known that both intrinsic and extrinsic effects can contribute to the optical properties of a semiconductor. So far, the optical properties of ZnO have been studied by a variety of experimental techniques such as photoluminescence (PL), cathodoluminescence (CL), optical transmission, absorption, and reflection *et al*. In this thesis, I mainly focus on studying the PL property of ZnO-related thin films and ZnO nanostructures. The PL spectrum has

exhibited a sharp peak of ultraviolet (UV) emission and a broad peak of deep level emission (DLE), respectively. Figure 1.2 shows the schematic diagram of the energy position of some deep level that emits in the visible region [41]. The UV emission is related to the crystalline quality, which corresponds to the exciton emission from near conduction band to valence band [42]. However, the DLEs in visible region are due to intrinsic defects in the crystal structure, which demonstrate that the green emission at ~2.5 eV is related to oxygen vacancies (V_o) [43] or interstitial zinc (Zn_i) [44] and the yellow emission at ~2 eV is related to zinc vacancies (V_{Zn}) [45,46] or interstitial oxygen (O_i) [47]. In order to fabricate high efficient optoelectronic devices with defect-related emission, the origin of deep level emissions observed in visible region should be clearly investigated.

Table 1.1 Physical parameters of bulk ZnO

Physical parameters	Values
Stable phase at RT	Wrutzite
a_0	3.250 Å
c_0	5.207 Å
Density	5.7 g/cm^3
Effective mass	$0.318m_0$ (electron) $0.5m_0$ (hole)
Energy gap	3.37 eV at RT
Intrinsic carrier concentration	$<10^6$ cm^{-3} (max n-type doping$>10^{20}$ cm^{-3} electrons; max p-type doping$<10^{17}$ cm^{-3} holes)
Conductivity	>200 cm^2/Vs

1.1.3 ZnO and nanostructured ZnO thin films fabrication

In terms of ZnO related materials thin films fabrication, thin films have been prepared by various techniques such as pulsed laser deposition [48-51], molecular beam epitaxy [52-54], and radio frequency (RF) sputtering [55-57]. In my study, the RF magnetron sputtering technique was mainly used for thin films deposition, which is considered as the most convenient method to deposit reproducible and homogeneous ZnO thin films over a large-area substrate at a lower deposition temperature.

Base on the thin films deposition, the annealing treatment has been widely known as a conventional and an efficient approach to improve the crystalline quality and optical property of

as-deposited films [58,59]. Currently, among the various ZnO-related nanostructures, one dimensional ZnO nanostructures such as nanotubes [60-62], nanowires [63], nanorods [64], nanobelts [65], tetrapods [66] and nanoribbons [67] have received increasing attention due to their properties and their potential applications in nanoelectronics, nanomechanics, and flat panel displays [68,69].

Among the various ZnO-related nanostructures, well-arrayed ZnO nanostructures have received increasing attention due to their properties and their potential application for nanodevices such as solar cells, luminescent, chemical sensors, and electrical devices and a variety of display units [70-73]. In order to improve the quality and efficiency applications of the ZnO nanostructures, theirs size and shape must be well controlled. In this study, ZnO related materials thin film phosphor was formed, which is potentially applied for vacuum fluorescent display (VFD).

1.1.4 ZnO thin film phosphor

1.1.4.1 The overview of phosphors

A phosphor is a material that absorbs light and exhibits the phenomenon of luminescence. It is normally divided into two parts of phosphorescent materials, which show brightness decay less than one millisecond, and fluorescent materials, where the emission decay takes place more than tens of nanoseconds [74].

In terms of the research on phosphors, reports go back more than 100 years. In 1866, Théodore Sidot of a French chemist prepared the ZnS type phosphors. It seems to mark the beginning of scientific research and synthesis of phosphors. In the late 19th century and the early 20th century, Philip E.A. Lenard and co-workers in Germany synthesized and evaluated a variety of phosphors related with alkaline earth chalcogenides (sulfides and selenides) and zinc sulfide. In the late 1920s and 1930s, P. W. Pohl and co-workers in Germany grew single-crystal phosphors and established the configurationally coordinate model of luminescence centers which pave the way for present day luminescence physics. From the end of World War II, phosphors and solid-state luminescence have been dramatically developed because of the support of progress in solid state physics. From then on, thousands of different phosphors are produced and combined with light source equipment for luminescent devices.

For the practical use of phosphors, theirs exploration and development are keeping the pace with the times, which represent not only the classical applications [75-78] such as fluorescent lamps, television tubes, X-ray screens, but also current optoelectronic devices [79-82] such as electroluminescent displays, vacuum fluorescent displays, plasma displays, and field emission displays. The applications of phosphors can be categorized as: (1) light sources represented by

fluorescent lamps; (2) display devices represented by cathode-ray tubes; (3) detector systems represented by X-ray screens and scintillators; and (4) other simple applications, such as luminous paint with long persistent phosphorescence.

1.1.4.2 Nanostructured ZnO thin film phosphor

ZnO thin film phosphor, a potential alternative to conventional powder phosphors, has attracted much interest for next generation flat-panel display applications due to its particular advantages, such as their high luminescent efficiency, high conductivity, adhesion to the substrate, and potential using in low-voltage fluorescence applications [83-85]. After reviewing the thin film phosphor related research publications, I found it remained some difficulties for thin film phosphor application, such as low luminescence, high temperature processes, expensive fabrication cost, and small area fabrication [86-88]. It is well known that high luminescent phosphors are normally fabricated or post-treatment under high temperatures [89,90]. However, high temperature processing is not suitable for glass substrates due to the low glass transition temperatures. In this case extensive applications of thin film phosphors in industrial processes are limited. Therefore, to date it still remains a bottleneck to fabricate highly luminescent ZnO thin film phosphors under low temperatures. In my thesis, well-arrayed ZnO nanostructures with high luminescent can be formed by modulating the deposition and post-treatment parameters at low temperature.

1.2 Objectives and structure of this thesis

In my thesis, first of all, I fabricated the ZnO related materials thin films using a conventional radio frequency (RF) magnetron sputtering and then evaluated thin films by all kinds of apparatus. Based on the characterization of thin films, the bottom-gate ZnO TFTs with excellent performance were successfully demonstrated. The following research was nanostructured ZnO thin films formation by different post-treatment processes. It has been found that nanostructured ZnO thin films formed in reducing gas show the intense green emission. The final destination is to optimize ZnO thin film phosphor with high visible light emission for optoelectronic applications, especial for VFD application.

As mentioned above, ZnO thin film phosphors can be applied into optoelectronic devices. However, ZnO nanostructures formation is one of the most important techniques for applications, especially for the controllable and well-arrayed ZnO nanostructures fabrication. In order to achieve the requirements for industrial application, the main objectives are concentrated on (1) ZnO related materials thin films fabrication, (2) nanostructured ZnO thin films' formation

and (3) characterization of ZnO thin film and nanostructured ZnO thin films for thin film transistors (TFTs) and vacuum fluorescent display with low-voltage excitation, respectively

The thesis is structured as follows: Chapter 2 briefly introduces the working principles, apparatus structures and parameters, and operation processes of fabrication equipment and characterization devices. ZnO related materials thin films with different deposition parameters were prepared by radio frequency magnetron sputtering system. The post-treatment processes were treated using commercial annealing furnace. Following the preparation of the samples, different characterization techniques were carried out to evaluate their structural and optical properties. Chapters 3-5 describe a variety of experimental methods for fabricating ZnO related materials thin films and nanostructured ZnO films. The characterization analyses of samples' results were discussed in detail. Chapter 3 performs ZnO thin films deposited by rf sputtering with modulating deposition parameters. The structural and optical properties of as-deposited ZnO films were strongly dependent on the Ar/O_2 ratio, puttering power, and deposition pressure. Chapter 4 describes the results of synthesis and characterization of $Zn_{1-x}Mg_xO$ (x=0.1, 0.3) thin films with the modulation of deposition pressure for x=0.3 and different post-treatment for x=0.1. The study of optical properties of multiple layers of ZnMgO/ZnO is also carried out. Based on ZnO thin films fabrication, Chapter 5 introduces the novel post-treatment processes on forming nanostructured ZnO thin films. The effects of different post-treatment processes on the structural and optical properties on nanostructured ZnO thin films were investigated. In Chapter 6, ZnO thin film as the channel layer was applied into TFTs. Nanostructured ZnO thin film as phosphor was potentially treated for VFD application. Finally, the conclusions for this thesis are drawn in Chapter 7.

The organization chart of this thesis is shown in Fig. 1.3.

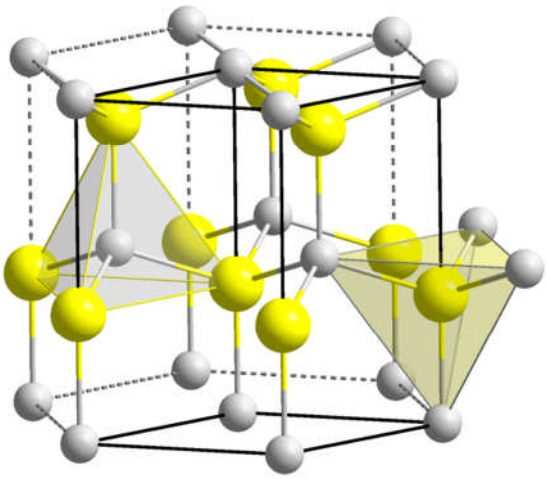

Fig. 1.1 The hexagonal wurtzite structure of ZnO. O atoms are shown as smaller white spheres and Zn atoms as large yellow spheres.

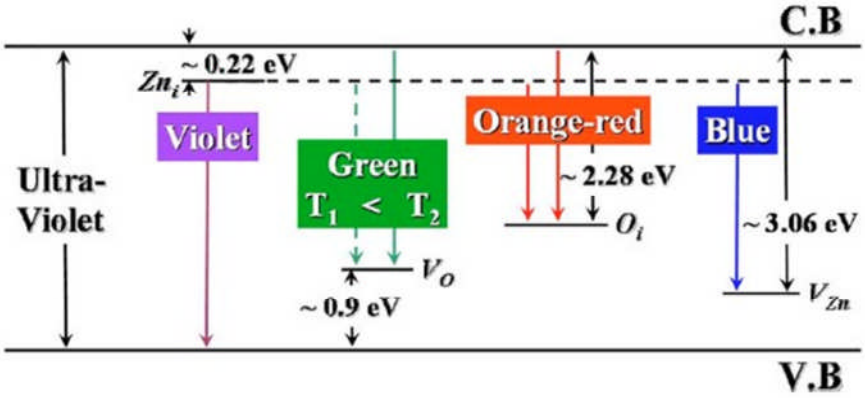

Fig. 1.2 Schematic band diagram of DLEs in ZnO.

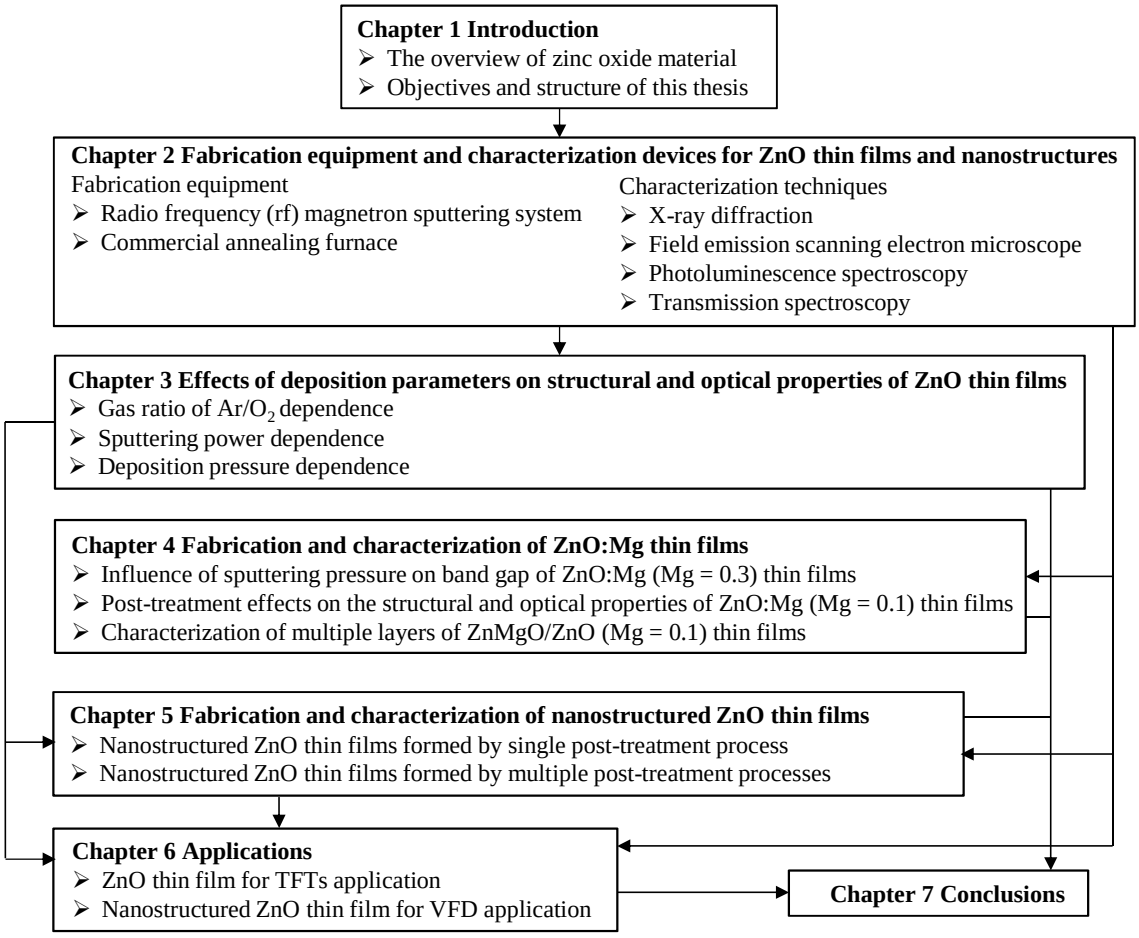

Fig. 1.3 The organization chart of this thesis.

1.3 References

[1] G. Busch, Eur. J. Phys., 10 (1989) 254.

[2] F. Laeri, F. Schuth, U. Simon, and M. Wark, "Host-Guest-Systems Based on Nanoporous Crystals", Wiley (2003).

[3] A.R. Hutson, Phys. Rev., 108 (1957) 222.

[4] G. Heiland, E. Mollwo, and F. Stochmann, Solid State Phys., 8 (1959) 193.

[5] R.A. Laudise, E.D. Kolb, and A.J. Caporaso, J. Am. Ceram. Soc., 47 (1964) 9.

[6] P.R. Emtage, J. Appl. Phys., 48 (1977) 4372.

[7] M. Inada, J. J. Appl. Phys., 17 (1978) 1.

[8] S.K. Tiku, C.K. Lau, and K.M. Lakin, Appl. Phys. Lett., 35 (1980) 318.

[9] C.H. Lin, B.S. Chiou, C.H. Chang, and J.D. Lin, Mater. Chem. Phys., 77 (2003) 647.

[10] K. Vanheusden, C.H. Seager, W.L. Warren, D.R. Tallant, and J.A. Voigt, Appl. Phys. Lett., 68 (1996) 403.

[11] Y. Hayashi, H. Narahara, T. Uchida, T. Noguchi, and S. Ibuki, Jpn. J. Appl. Phys., 34 (1995) 1878.

[12] Z.S. Wang, C.H. Huang, Y.Y. Huang, Y.J. Hou, P.H. Xie, B.W. Zhang, and H.M. Cheng, Chem. Mater., 13 (2001) 678.

[13] K. Keis, C. Bauer, G. Boschloo, A. Hagfeldt, K. Westermark, H. Rensmo, and H. Siegbahn, J. Photoch. Photobio. A, 148 (2002) 57.

[14] J. Katayama, K. Ito, M. Matsuoka, and J. Tamaki, J. Appl. Electrochem., 34 (2004) 687.

[15] T. Minami, H. Nanto, and S. Takata, Jpn. J. Appl. Phys., 23 (1984) L280.

[16] S.Y. Myong, S.J. Baik, C.H. Lee, W.Y. Cho, and K.S. Lim, Jpn. J. Appl. Phys., 36 (1997) L1078.

[17] S.J. Baik, J.H. Jang, C.H. Lee, W.Y. Cho, and K.S. Lim, Appl. Phys. Lett., 70 (1997) 3516.

[18] T. Minami, H. Nanto, and S. Takata, Thin Solid Films, 124 (1985) 43.

[19] D.K. Hwang, S.H. Kang, J.H. Lim, E.J. Yang, and J.Y. Oh, Appl. Phys. Lett., 86 (2005) 222101.

[20] J.H. Lim, C.K. Kang, K.K. Kim, I.K. Park, D.K. Hwang, and S.J. Park, Adv. Mater., 18 (2006) 2720.

[21] W.Z. Xu, Z.Z. Ye, Y.J. Zeng, L.P. Zhu, B.H. Zhao, L. Jiang, J.G. Lu, H.P. He, and S.B. Zhang, Appl. Phys. Lett., 88 (2006) 173506.

[22] H. Seo, S. Aihara, T. Watabe, H. Ohtake, T. Sakai, M. Kubota, N. Egami, T. Hiramatsu, T. Matsuda, M. Furuta, and T. Hirao, Jpn. J. Appl. Phys., 50 (2001) 024103.

[23] M. Furuta, Y. Kamada, M. Kimura, T. Hiramatsu, T. Matsuda, H. Furuta, C. Li, S. Fujita, and T. Hirao, IEEE Electr. Device L., 31 (2010) 1257.

[24] M. Kimura, Y. Kamada, S. Fujita, T. Hiramatsu, T. Matsuda, M. Furuta, and T. Hirao, Appl. Phys. Lett., 97 (2010) 163503.

[25] Y. Kamada, S. Fujita, T. Hiramatsu, T. Matsuda, H. Nitta, M. Furuta, and T. Hirao, Jpn. J. Appl. Phys., 49 (2010) 03CB03.

[26] M. Furuta, Y. Kamada, T. Hiramatsu, C. Li, M. Kimura, S. Fujita, and T. Hirao, Jpn. J. Appl. Phys., 50 (2011) 03CB09.

[27] A. Cimino, G. Mazzone, and P. Porta, Z. Phys. Chem. (NF), 41 (1964) 154.

[28] S.K. Kim, S.Y. Jeong, and C.R. Cho, Appl. Phys. Lett. 82 (2003) 562.

[29] J.E. Jaffe, J.A. Snyder, Z. Lin, and A.C. Hess, Phys. Rev. B, 62 (2000) 1660.

[30] S. Bloom and I. Ortenburger, Phys. Stat. Sol. B, 58 (1973) 561.

[31] Y.N. Xu and W.Y. Ching, Phys. Rev. B, 48 (1993) 4335.

[32] D. Vogel, P. Kruger, and J. Pollmann, Phys. Rev. B, 52 (1995) 316.

[33] F.K. Shan, B.I. Kim, G.X. Liu, Z.F. Liu, J.Y. Sohn, W.J. Lee, and B.C. Shin, J. Appl. Phys., 95 (2004) 4772.

[34] C. Yang, X.M. Li, X.D. Gao, X. Cao, R. Yang, and Y.Z. Li, J. Cryst. Growth, 312 (2010) 978.

[35] H. Tanaka, S. Fujita, and S. Fujita, Appl. Phys. Lett., 86 (2005) 192911.

[36] H. Li, Y.Z. Zhang, X.J. Pan, T. Wang, and E.Q. Xie, J. Alloys Compd., 472 (2009) 208.

[37] T. Kawaharamura, Dr. Thesis, “Study on mist CVD method and its application to the growth of ZnO thin films” Kyoto-Univ., 2008.

[38] S.O. Kucheyev, J.E. Bradby, J.S. Williams,C. Jagadish, and M.V. Swain, Appl. Phys. Lett., 80 (2002) 956.

[39] A. Dal Corso, M. Posternak, R. Resta, and A. Baldereschi, Phys. Rev. B, 50 (1994) 10715.

[40] S.J. Pearton, D.P. Norton, K. Ip, Y.W. Heo, and T. Steiner, Prog. in Mater. Sci., 50 (2005) 293.

[41] C.H. Ahn, Y.Y. Kim, D.C. Kim, S.K. Mohanta, and H.K. Cho, J. Appl. Phys., 105 (2009) 013502.

[42] C.T. Lee, Materials, 3 (2010) 2218.

[43] P.H. Kasai, Phys. Rev., 130 (1963) 989.

[44] M. Willander, O. Nur, J.R. Sadaf, M.I. Qadir, S. Zaman, A. Zainelabdin, N. Bano, and I. Hussain, Materials, 3 (2010) 2643.

[45] M. Liu, A.H. Kitai, and P. Mascher, J. Lumin., 54 (1992) 35.

[46] E.G. Bylander, J. Appl. Phys., 49 (1978) 1188.

[47] J. Zhong, A.H. Kitai, P. Mascher, and W. Puff, J. Electrochem. Soc., 140 (1993) 3644.

[48] X.L. Guo, J.H. Choi, H. Tabata, and T. Kawai, Jpn. J. Appl. Phys., 40 (2001) L177.

[49] H. Ohta, M. Orita, M. Hirano, and H. Hosono, J. Appl. Phys., 89 (2001) 5720.

[50] A. Tsukazaki, M. Kubota, A. Ohtomo, T. Onuma, K. Ohtani, H. Ohno, S.F. Chichibu, and M. Kawasaki, Jpn. J. Appl. Phys., 44 (2005) L643.

[51] J. Nishii, A. Ohtomo, K. Ohtani, H. Ohno, and M. Kawasaki, Jpn. J. Appl. Phys., 44 (2005) L1193.

[52] S. Sasa, M. Ozaki, K. Koike, M. Yano, and M. Inoue, Appl. Phys. Lett., 89 (2006) 053502-1.

[53] H. Tampo, K. Matsubara, A. Yamada, H. Shibata, P. Fons, M. Yamagata, H. Kanie, and S. Niki, J. Cryst. Growth, 301-302 (2007) 358.

[54] K. Hirano, M. Fujita, M. Sasajima, T. Kosaka, and Y. Horikoshi, J. Cryst. Growth, 301-302 (2007) 370.

[55] Q.P. Wang, D.H. Zhang, H.L. Ma, X.H. Zhang, and X.J. Zhang, Appl. Surf. Sci., 220 (2003) 12.

[56] K. Ito and T. Nakazawa, Jpn. J. Appl. Phys., 22 (1983) L245.

[57] T. Minami, H. Sato, H. Nanto and S. Takata, Jpn. J. Appl. Phys., 24 (1985) L781.

[58] Y. Lin, J. Xie, H. Wang, Y. Li, C. Chavez, S.Y. Lee, S.R. Foltyn, S.A. Crooker, A.K. Burrell, T.M. McCleskey, and Q.X. Jia, Thin Solid Films, 492 (2005) 101.

[59] Y. Caglar, S. Ilican, M. Caglar, F. Yakuphanoglu, J.S. Wu, K. Gao, P. Lu, and D.F. Xue, J. Alloy. Compd., 481 (2009) 885.

[60] H.D. Yu, Z.P. Zhang, M. Y. Han, X.T. Hao, and F.R. Zhu, J. Am. Chem. Soc., 127 (2005) 2378.

[61] G.W. She, X.H. Zhang, W.S. Shi, X.F. Jack, C. Chang, C.S. Lee, S.T. Lee, and C.H. Liu, Appl. Phys. Lett., 92 (2008) 053111.

[62] Y.J. Xing, Z.H. Xi, Z.Q. Xue, X.D. Zhang, J.H. Song, R.M. Wang, J. Xu, Y. Song, S.L. Zhang, and D.P. Yua, Appl. Phys. Lett., 83 (2003) 1689.

[63] M.H. Huang, S. Mao, H. Feick, H.G. Yan, Y.Y. Wu, H. Kind, E. Weber, R. Russo, and P.D. Yang, Science, 292 (2001) 1897.

[64] L. Vayssieres, Adv. Mater., 15 (2003) 464.

[65] Z.W. Pan, Z.R. Dai, Z.L. Wang, Science, 291 (2001) 1947.

[66] Y. Qiu and S. Yang, Adv. Func. Mater., 17 (2007) 1345.

[67] X. Fan, M.L. Zhang, I. Shafig, W.J. Zhang, C.S. Lee, S.T. Lee, Adv. Mater., 21 (2009) 2393.

[68] M.J. Zheng, L.D. Zhang, G.H. Li, and W.Z. Shen, Chem. Phys. Lett., 363 (2002) 123.

[69] Q.F. Zhang, C.S. Dandeneau, X.Y. Zhou, G.Z. Cao, Adv. Mater., 21 (2009) 4087.

[70] D.M. Bagnall, Y.F. Chen, Z. Zhu, T. Yao, S. Koyama, M.Y. Shen, and T. Goto, Appl. Phys. Lett., 70 (1997) 2230.
[71] B. Sang, A. Yamada, and M. Konagai, Jpn. J. Appl. Phys., 37 (1998) L206.
[72] N.J. Dayan, S.R. Sainkar, R.N. Karekar, and R.C. Aiyer, Thin Solid Films, 325 (1998) 254.
[73] C.R. Gorla, N.W. Emanetoglu, S. Liang, W.E. Mayo, Y. Lu, M. Wraback, and H. Shen, J. Appl. Phys., 85 (1999) 2595.
[74] M.Y. William, S. Shionoya, and H. Yamamoto, "Phosphor Handbook", CRC Press, New York (2006).
[75] J.K. Park, C.H. Kim, S.H. Park, H.D. Park, and S.Y. Choi, Appl. Phys. Lett., 84 (2004) 1647.
[76] H. Masui, S. Nakamura, and S.P. Denbaars, Jpn. J. Appl. Phys., 45 (2006) L910.
[77] R.M. Nishikawa and M.J. Yaffe, Med. Phys., 17 (1990) 894.
[78] R. Raue, A.T. Vink, and T. Welker, Philips Tech. Rev., 44 (1989) 335.
[79] S. Gupta, J.C. McClure, and V.P. Singh, Thin Solid Films, 299 (1997) 33.
[80] C.C. Wu, K.B. Chen, C.S. Lee, T.M. Chen, and B.M. Cheng, Chem. Mater., 19 (2007) 3278.
[81] H. Jiao, F. Liao, S. Tian, and X. Jing, J. Electrochem. Soc., 151 (2004) J39.
[82] B.S. Jeon, G.Y. Hong, Y.K. Yoo, and J.S. Yoo, J. Electrochem. Soc., 148 (2001) H128.
[83] M.H. Huang, S. Mao, H. Feick, H. Yan, Y. Wu, H. Kind, E. Weber, R. Russo, and P. Yang, Science, 292 (2001) 1897.
[84] J.H. Park, S.J. Jang, S.S. Kim, and B.T. Lee, Appl. Phys. Lett., 89 (2006) 121108.
[85] T. David, S. Goldsmith, and R.L. Boxman, Thin Solid Films, 447-448 (2004) 61.
[86] Y. Nakanishi, A. Miyake, H. Tatsuoka, H. Kuwabara, and Y. Hatnaka, Appl. Surf. Sci., 244 (2005) 359.
[87] S. Fujihara, Y. Ogawa, and A. Kasai, Chem. Mater., 16 (2004) 2965
[88] H. Song and Y.J. Kim, J. Eur. Ceram. Soc., 27 (2007) 3745.
[89] J. Zhong, A.H. Kitai, and P. Mascher, J. Electrochem. Soc., 140 (1993) 3644.
[90] K. Vanheusden, W.L. Warren, C.H. Seager, D.R. Tallant, J.A. Vougt, and B.E. Gnade, J. Appl. Phys., 79 (1996) 7983.

Chapter 2

Fabrication equipment and characterization devices for ZnO thin films and nanostructures

In this chapter, the formation and evaluation equipment were briefly described on the fabrication and characterization of ZnO related materials thin film and nanostructures. In terms of samples preparation, radio frequency magnetron sputtering system and commercial annealing furnace were mainly used. Following the preparation of the samples, different characterization techniques were carried out to evaluate their structural and optical properties. The crystal structure of the samples was characterized using an X-ray diffraction system (XRD). The surface morphologies of the samples were observed by a field emission scanning electron microscope (FE-SEM) system. The different luminescent characteristics of the samples were measured by photoluminescence (PL) measurement. Optical transmission spectra measurements were performed using an UV-visible spectrophotometer. We will introduce all techniques one by one.

2.1 Fabrication equipment

2.1.1 Radio frequency magnetron sputtering system

Sputter deposition is a physical vapor deposition (PVD) method for depositing thin films, which is one of the most popular growth techniques due to its low cost, simplicity, large area, and low deposition temperature [1]. Sputtering means to eject material from a target and then deposit it on the substrate. Magnetron sputtering can be classified into direct current (DC) and radio frequency (RF) modes. The target of DC sputtering should be conducting materials because of the positive charge will build up on the target and stop sputtering process. However, the target of RF sputtering can be conducting or non-conducting materials. Therefore, in this thesis, we selected RF sputtering technique for ZnO related materials films deposition.

In this thesis, ZnO related materials films were deposited on variety of substrates by a conventional 13.56 MHz rf magnetron sputtering system, as shown in Fig. 2.1 of diagrammatic sketch of sputtering apparatus [2-4]. The Table 2.1 lists the deposition parameters of RF magnetron sputtering. The source materials of target are located on a cathode keeping a distance away from the substrate stage. Substrates are placed in a vacuum chamber pumped down to a prescribed process pressure using a turbo molecular pump. The working gases are introduced

into the chamber controlled by mass flow meters. Sputtering happens when a negative charge is applied to the target material causing a plasma or glow discharge. Positive charged gas ions generated in the plasma region are attracted to the negatively biased target plate at a very high speed. This collision results into a momentum transfer and the ejected species including the sputtered adatoms and ion clusters from the target experience collisions and scatterings with the sputtering gas atoms prior to reach to substrate [5,6]. These ejected species are finally deposited as a thin film on the surface of the substrates.

Table 2.1 Deposition parameters of RF magnetron sputtering.

Target (4 inch)	ZnO (5N), ZnO/MgO (90/10, 70/30 wt.%), ZnO/Al_2O_3 (98/2 wt.%)
Substrates	Quartz glass, p-type Silicon(100) (0.02 Ω·cm)
Working distance	60, 88 mm
Temperature	Room temperature-250 ^oC
Deposition pressure	1, 3, 5, 7, 9 Pa
Ar gas flow rate	0-30 sccm
O_2 gas flow rate	0-30 sccm
RF power	60-240 W (0.8-3.1 W/cm^2)

The kinetic energy loss of ejected species from the target to substrate is affected by the deposition parameters, special for sputtering pressure in my research. The kinetic energy of species is inversely proportional to the deposition pressure. Here, the mean free path can help us understand the phenomenon [7]. The mean free path (λ) of a molecule is the average distance the particle travels between collisions with other moving particles, which can be expressed as below equations.

$$\lambda = \frac{1}{\sqrt{2}\pi\sigma^2 n} \tag{2.1}$$

where σ is the diameter of working gas, n is molecular density.

$$\lambda = \lambda_0 \left(\frac{T}{273}\right)\frac{1}{p} \tag{2.2}$$

λ_0 is a constant at 1 Torr and 0 ^oC. Take the argon gas as an example, the λ_0 is 0.48. When the thin films are deposited under high deposition pressure, ejected species will suffer much more collisions to shrink the mean free path, resulting in the more kinetic energy loses.

In terms of magnetron sputtering system, magnets are used to increase the percentage of electrons that take part in ionization of events and thereby increase the probability of electrons

striking the argon atoms, increase the length of the electron path, and hence increase the ionization efficiency significantly, as shown in Fig. 2.2 of the schematic diagram of magnetron sputtering. During sputtering process, the ejected species with high energy can contribute to (1) increase substrate temperature, and hence influent the crystallinity of thin film; (2) cause the damage of substrate or/and films.

2.1.2 Commercial annealing furnace

After the samples deposition, the annealing treatment has been widely known as a conventional and an efficient approach to improve the crystalline quality and optical property of as-deposited films [8,9]. Commercial annealing furnace, one of oven type equipment, is used for types of materials' post-treatment. It is most often utilized in laboratories as a compact means of creating suitable post-treatment temperature atmospheres. The furnace can be fine turned to hold very accurate and stable temperatures with very little variance. It is used to test the characteristics of materials at these extremely high and accurate temperatures.

In my research, a conventional furnace annealing system was carried out. Annealing furnace is large temperature atmospheric range from room temperature up to 800 ^{o}C, which make of pure quartz that allow for the introduction and mixing of gases (N_2, Ar, O_2 and forming gas (H_2 in N_2: 1.9%)). A quartz tube, 20 cm in diameter and 75 cm in length, is brought up and maintained at a requested temperature by means of a heating element surrounded by an insulating material. A quartz boat supports ZnO related materials thin films while they are placed in the center of a quartz tube, as shown in Fig. 2.3. The post-treatment conditions in my study are listed in table 2.2.

Table 2.2 Post-treatment parameters of furnace in this study.

Substrates	Quartz glass, p-type Silicon(100) (0.02 Ω·cm)
Gas flow rate	N_2 or O_2: 100 sccm, Forming gas (H_2 in N_2: 1.9%): 165 sccm.
Temperature	430-500 ^{o}C
Annealing pressure	N_2 or O_2: 10 KPa, Forming gas: 50 KPa.
Annealing time	2-8 h

2.2 Characterization techniques

2.2.1 X-ray diffraction

In my experiments, the crystal structure of the ZnO related materials films and nanostructures were characterized using an X-ray diffraction system (Rigaku ATX-G diffractometer), employing a Cu Kα tube (λ = 0.154178 nm) radiation (50 kV, 300 mA). The schematic diagram of X-ray diffractometer optical system is cited in Fig. 2.4 [10].

It is well-known that X-ray is one kind of electromagnetic radiation with the wavelength of 1 Å, which is in the region between gamma-rays and ultraviolet. X-ray diffraction is one of most popular non-destructive experimental techniques for probing the crystalline structure at atomic level.

A crystal lattice is a regular three-dimensional distribution of atoms in space. These are arranged to form a series of parallel planes separated with a distance d, which varies according to the structural and physical information of the material. Figure 2.5 illustrates the schematic diagram of Bragg diffraction from two parallel planes. When a monochromatic X-ray with the wavelength of λ interacts with a crystal sample at an angle θ, the diffraction from parallel planes of atoms occurs according to Bragg's law [11].

$$n\lambda = 2\mathrm{d}sin\theta \qquad (2.3)$$

Where n is integer that represents the order of the reflection, λ is the wavelength of X-ray beam. By modulating the angle θ, in terms of Bragg's law, the characteristic of the materials can be evaluated in detail.

The XRD patterns include peak position and intensity of the diffracted beam, which provides a variety of information of the films. Angles are used to calculate the interplanar atomic spacing. Until now, over 80,000 materials have been enrolled into the International Powder Diffraction File (PDF) database as the Joint Committee for Powder Diffraction Standards (JCPDS) [12,13]. Once the XRD patterns are provided, comparing with the standard data, the results of the crystal, phase composition, grain size, and lattice strain can be easily calculated. All in all, X-ray diffraction is a powerful tool and indispensable to materials science.

2.2.2 Field emission scanning electron microscope

A field emission scanning electron microscope (FE-SEM) system (JEOL-JSM7400F) was used to observe the surface morphologies of the samples. The chamber pressure is about 10^{-8} Pa. The gun voltage range is from 1 to 30 kV. A max resolution of about 1.5 nm can be achieved. The SEM reveals topographic features of the samples, which help us to evaluate the diameter, length, shape and density of the ZnO nanostructures [14].

The scanning electron microscope (SEM) uses a focused beam of high-energy electrons to generate a variety of signals at the surface of solid specimens. The signals derived from electron-sample interactions reveal the sample information including external morphology,

chemical composition, crystalline structure, and orientation of materials. These signals include secondary electrons, backscattered electrons (BSE), diffracted backscattered electrons (EBSD), photons (characteristic X-rays), visible light (cathodoluminescence), and heat.

The schematic diagram of SEM is exhibited in Fig. 2.5 [15]. A stream of monochromatic electrons is represented at the top of microscopy by heating up the filament. The electron stream is condensed by the first condenser lens. This lens is used to both form the beam and limit the amount of current in the beam. It works in conjunction with the condenser aperture to eliminate the high-angle electrons from the beam. The beam is then constricted by the condenser aperture, eliminating some high-angle electrons. The second condenser lens forms the electrons into a thin, tight, coherent beam. Finally, the beam hits the sample; the signals such as backscattered or secondary are ejected from the sample. The instruments count the number of e^- interactions and display to the screen whose intensity is determined by this number, producing the SEM image.

The elemental composition of the specimen can be identified by energy dispersive X-ray spectroscopy (EDX). The EDX analysis system works as an integrated feature of a scanning electron microscope (SEM), and cannot operate on its own without the latter.

2.2.3 Photoluminescence spectroscopy

In my thesis, the different luminescent characteristics of as-deposited ZnO-related films and ZnO nanostructures after annealing process were measured by photoluminescence (PL) measurement, which was performed with an iHR320 Micro-PL/Raman spectroscope (Horiba Ltd.). A He-Cd laser with a wavelength of 325 nm at a power of 20 mW was used as an excitation light source. The basic scheme of PL spectroscopy experimental set-up is illustrated in Fig. 2.6 [16].

Photoluminescence (PL) is a couple of processes in which a substance absorbs photons and then re-radiates photons. It means that an excitation to a higher energy state and then a return to a lower energy state accompanied by the emission of a photon. The information of the energy band structure of semiconductor could be obtained from the analysis of PL spectra. To date, there are many different type lasers have been widely used in the PL setup, for example, He-Cd laser with 325 nm, Ar^+ laser with 316nm/514 nm/488 nm, Nd:YAG pulsed laser with 266 nm , tunable solid state lasers and so on [17,18].

Photoluminescence is an important technique for measuring the purity and crystalline quality of semiconductors. Several variations of photoluminescence exist, including photoluminescence excitation (PLE). Time-resolved photoluminescence (TRPL) is a method where the sample is excited with a light pulse and then the decay in photoluminescence with respect to time is measured [19,20]. This technique is useful in measuring the minority carrier lifetime of

semiconductors.

A variety of material properties can be obtained by PL measurement, which will be listed as follows: (1) Band gap determination; (2) Impurity levels and defect detection; (3) Recombination mechanisms; (4) Material optical quality.

The results of PL spectrum covered the whole visible region varied from 300 to 1000 nm. The PL spectrum has exhibited a sharp peak of ultraviolet (UV) emission and a broad peak of deep level emission (DLE), respectively. The UV emission is related to the crystalline quality, which corresponds to the exciton emission from near conduction band to valence band. However, the DLEs in visible region are due to intrinsic defects in the crystal structure. In my study, ZnO nanostructures exhibit a broad green emission of about 500 nm due to the oxygen vacancies in the ZnO thin films.

2.2.4 Transmission spectroscopy

In this thesis, optical transmission spectra measurements of samples were performed using an Ultraviolet-Visible-Infrared (UV-Vis-IR) spectrophotometer (U-4100, Hitachi Corp.). It is possible to construct a non-destructive system which satisfies various analyses. The measurement region permits measurement from 175 up to 2600 nm. The spectrophotometer is useful to characterize the absorption, transmission, and reflectivity of all kinds of technologically important materials. The application, such as pigments, coatings, windows, and filters, usually requires recording at least a portion of the optical spectrum for evaluation of the optical or electronic properties of materials.

Transmission spectroscopy is mainly interrelated to absorption spectroscopy. Here, light passes through the sample such as solid, liquid, and gas sampling and compared to light that has not. The output result depends on the path length or sample thickness, the absorption coefficient of the sample, the reflectivity of the sample, the angle of incidence, the polarization of the incident radiation, and, for particulate matter, on particle size and orientation.

Figure 2.7 shows the optical system of U-4100 UV-Vis-IR spectrophotometer [21]. An incident light beam from tungsten lamp (UV, visible and IR) and deuterium lamp (deep UV) is split into a monochromatic, and then reach a sample, part of the beam is reflected and part of the beam is transmitted through the medium which is measured by the photomultiplier and recorded by the computer, and the rest of the beam will be absorbed. Absorption of photons arises due to the transition of the electrons from the lower to the higher energy levels. The absorption coefficient decides its absorption ability of a mater. Absorption coefficient α for a uniform medium can be defined in terms of the intensity change of a monochromatic light beam in unit distance that the beam traveled in the medium.

$$\frac{dI(\lambda)}{dx} = -\alpha(\lambda)I(\lambda) \quad (2.4)$$

So the beam intensity as a function of the distance *x* can be expressed as:

$$I(\lambda) = I_0(\lambda)e^{-\alpha(\lambda)x} \quad (2.5)$$

In classical electromagnetic theory, absorption coefficient is related to the imaginary part of the complex index of refraction $\mathbf{n_c=n-ik}$ with

$$\alpha = \frac{4\pi\nu}{c} \quad (2.6)$$

where *v* is the frequency of the light. The imaginary part of the complex index of refraction, k is also called the extinction coefficient.

The relationship between the absorption coefficient and the photon energy can be expressed as following equation [22]:

$$(\alpha h\nu)^2 = A(h\nu - E_g) \quad (2.7)$$

where *A* and E_g represent the constant and the band gap of a film. The absorption coefficient (α) could be obtained from the transmittance T = Aexp(-αd), where A and d are constant and thickness of the film, respectively. The band gap (E_g) is determined by extrapolation of the linear portion to the photon energy axis at $(\alpha h\upsilon)^2 = 0$.

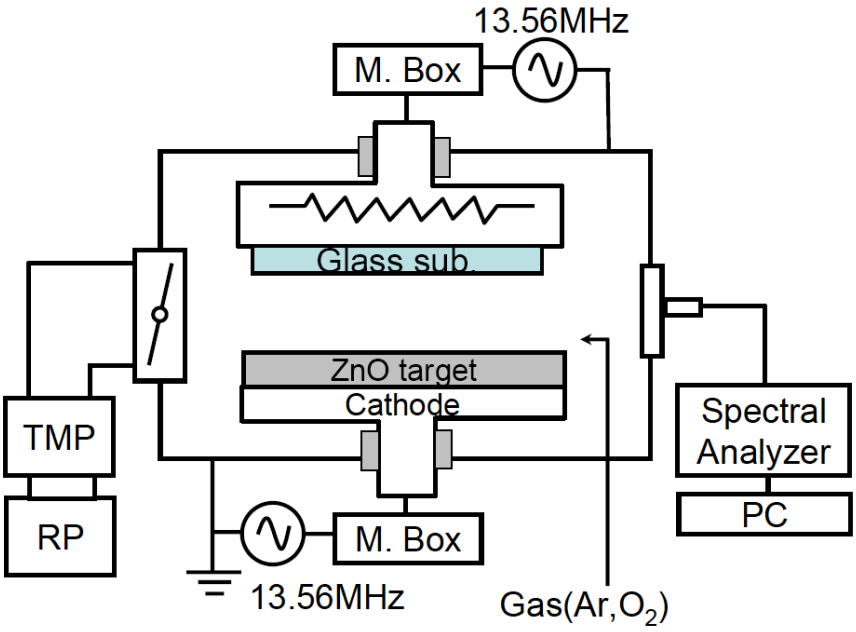

Fig. 2.1 The diagrammatic sketch of sputtering apparatus.

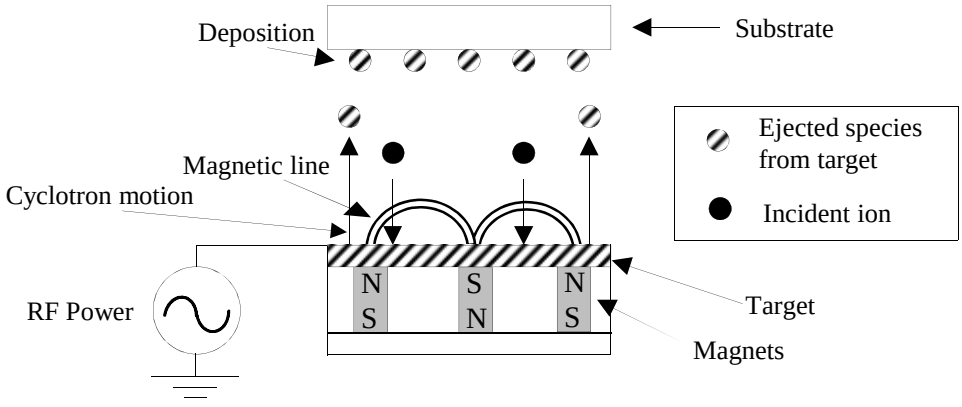

Fig. 2.2 The schematic diagram of magnetron sputtering.

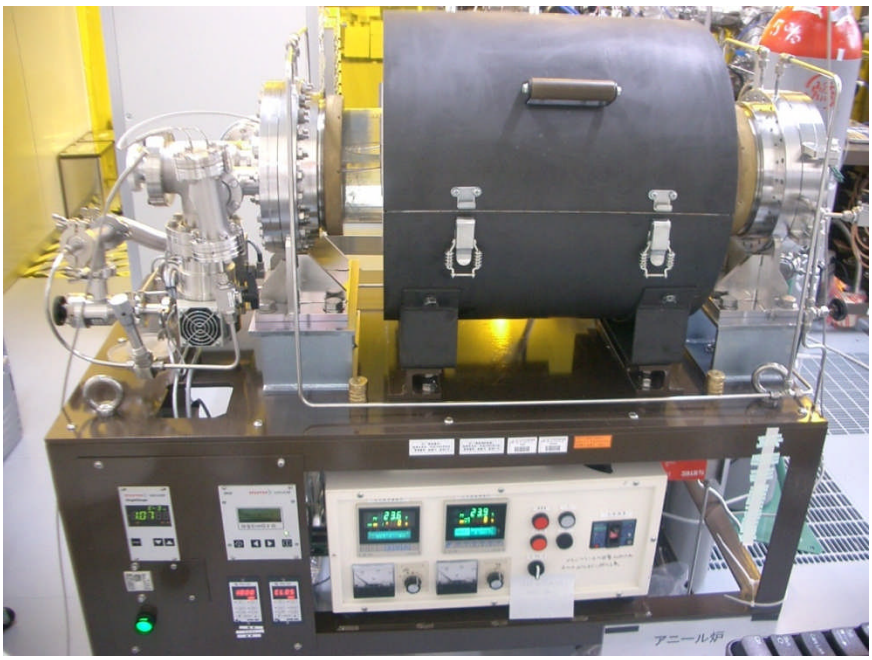

(a)

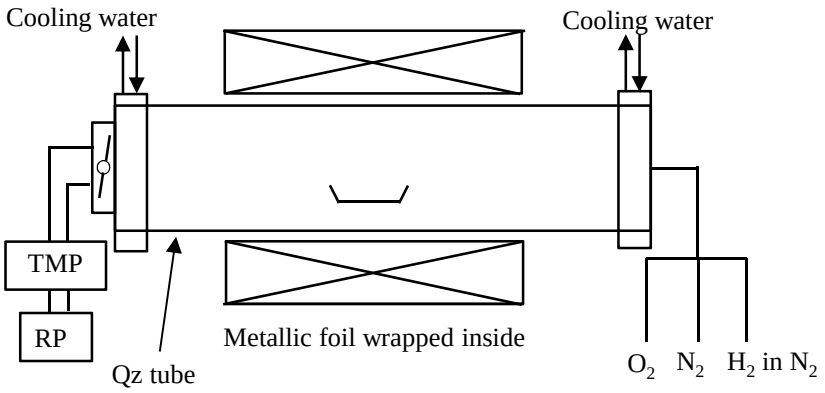

(b)

Fig. 2.3 (a) The furnace system, and (b) a schematic diagram of furnace.

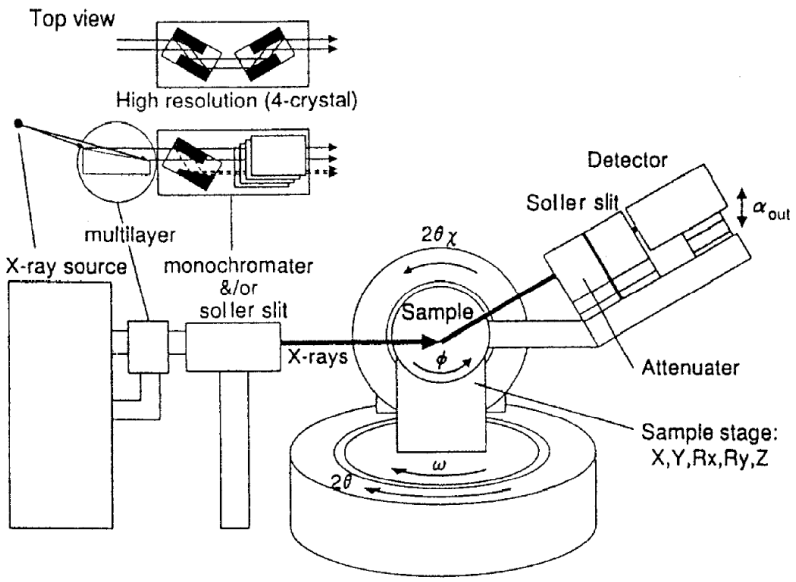

Fig. 2.4 The schematic diagram of X-ray diffractometer optical system.

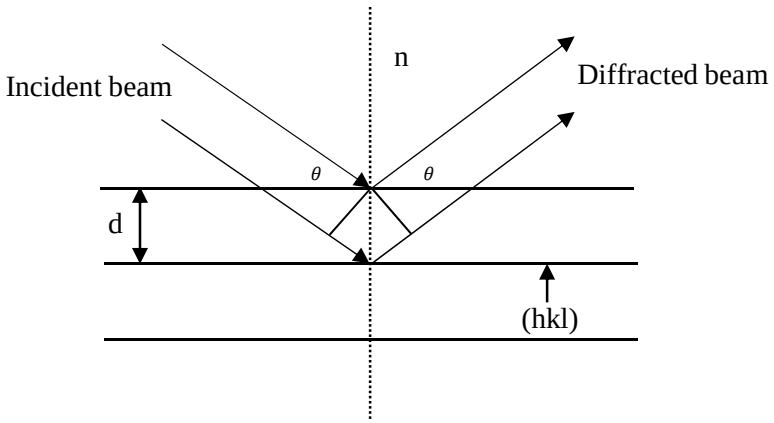

Fig. 2.5 The schematic diagram of Bragg diffraction from two parallel planes.

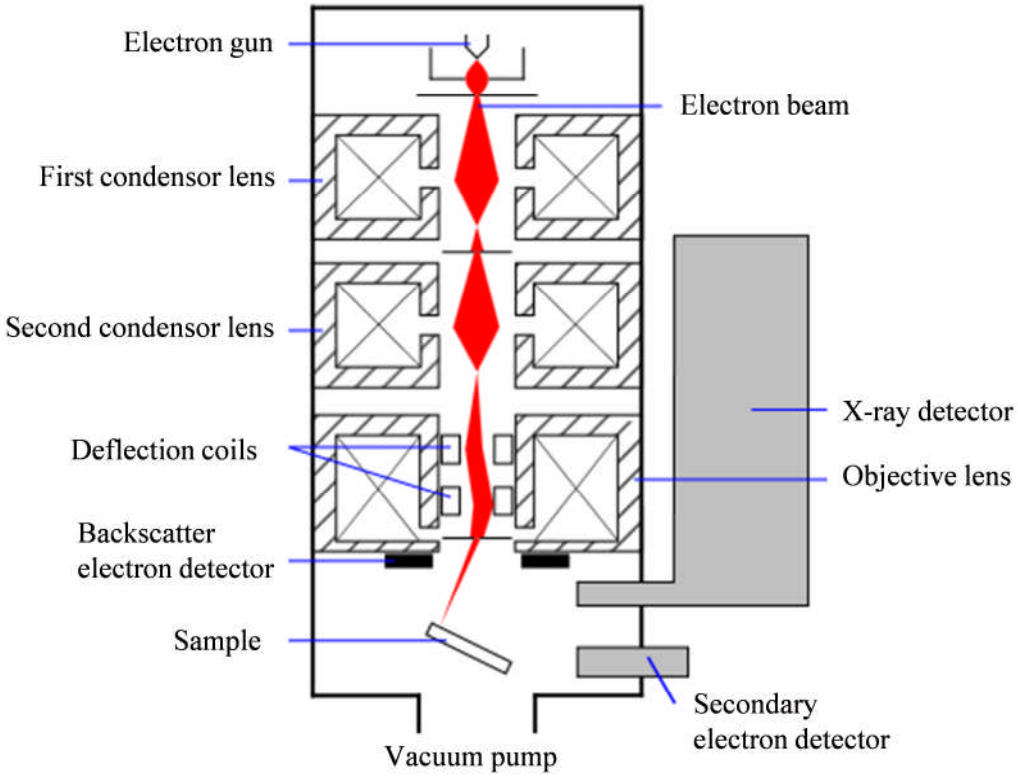

Fig. 2.6 Schematic image of SEM.

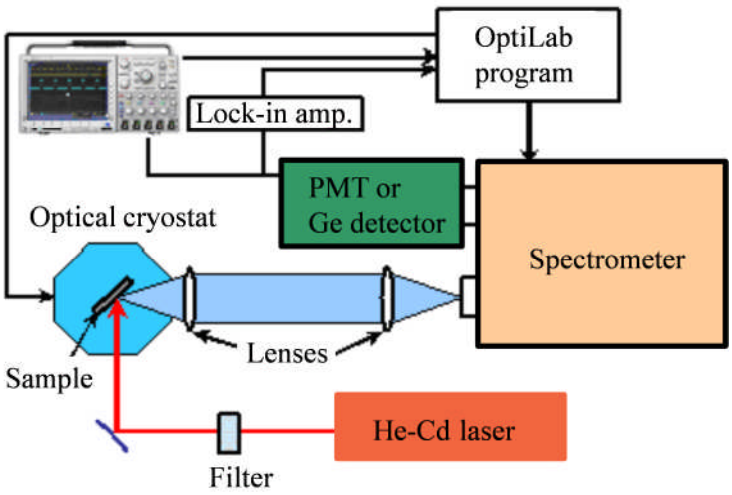

Fig. 2.7 The basic scheme of PL spectroscopy experimental set-up.

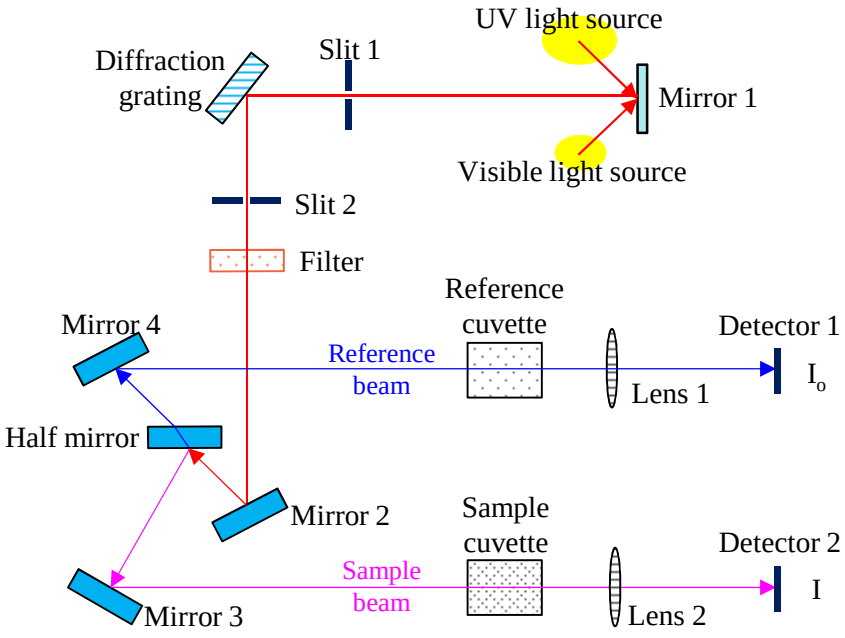

Fig. 2.8 Optical system of U-4100 UV-Vis-IR spectrophotometer

2.3 References

[1] J.L. Vossen, Phys. Thin Films, 9 (1977) 1.

[2] T. Matsuda, M. Furuta, T. Hiramatsu, H. Furuta, C. Li, and T. Hirao, Appl. Surf. Sci., 256 (2010) 6350.

[3] M. Furuta, T. Hiramatsu, T. Matsuda, C. Li, H. Furuta, and T. Hirao, J. Non-Cryst. Solids, 354 (2008) 1926.

[4] T. Hiramatsu, M. Furuta, H. Furuta, T. Matsuda, and T. Hirao, Jpn. J. Appl. Phys., 46 (2007) 3319.

[5] P. Misra, P. Bhattacharya, K. Mallik, S. Rajagopalan, L.M. Kukreja, and K.C. Rustagi, Solid State Commun., 117 (2001) 673.

[6] D. Wang, T. Narusawa, T. Kawaharamura, M. Furuta, and C. Li, J. Vac. Sci. Technol. B, 29 (2011) 051205-1.

[7] B.A. Gurney, V.S. Speriosu, J.P. Nozieres, H. Lefakis, D.R. Wilhoit, and O.U. Need, Phys. Rev. Lett., 71 (1993) 4023.

[8] C. Li, T. Kawaharamura, T. Matsuda, H. Furuta, T. Hiramatsu, M. Furuta, and T. Hirao, Appl. Phys. Express, 2 (2009) 091601.

[9] Y. Lin, J. Xie, H. Wang, Y. Li, C. Chavez, S.Y. Lee, S.R. Foltyn, S.A. Crooker, A.K. Burrell, T.M. McCleskey, and Q.X. Jia, Thin Solid Films, 492 (2005) 101.

[10] “Advanced thin film X-ray system-Grazing incidence in-plane diffractometer”, The Rigaku Journal, 16 (1999) 54.

[11] J.M. Jensen, A.B. Oelkers, R. Toivola, and D.C. Johnson, J.W. Elam, and S.M. George, Chem. Mater., 14 (2002) 2276.

[12] J. Zhang, L. Sun, C. Liao, and C. Yan, Chem. Comm., (2002) 262.

[13] B. Cheng and E.T. Samulski, Chem. Comm., (2004) 986.

[14] L.L. Yang, Dr. Thesis, “Synthesis and characterization of ZnO nanostructures” Linkoping-Univ. Sweden, 2010.

[15] http://en.wikipedia.org/wiki/Scanning_electron_microscope.

[16] http://www.itst.ucsb.edu/~vinhnguyen/Time-Frequency_Spectroscopy.htm

[17] Q. Wan, Q.H. Li, Y.J. Chen, T.H. Wang, X.L. He, X.G. Gao, and J.P. Li, Appl. Phys. Lett., 84 (2004) 3085.

[18] D. Kan, T. Terashima, R. Kanda, A. Masuno, K. Tanaka, S.C. Chu, H. Kan, A. Ishizumi, Y. Kanemitsu, and Y. Shimakawa, Nat. Mater., 4 (2005) 816.

[19] S.W. Jung, W.I. Park, H.D. Cheong, G.C. Yi, H.M. Jang, S. Hong, and T. Joo, Appl. Phys. Lett., 80 (2002) 1924.

[20] S. Hong, T. Joo, W. Park, Y.H. Jun, and G.C. Yi, Appl. Phys. Lett., 83 (2002) 4157.
[21] http://bouman.chem.georgetown.edu/S00/handout/spectrometer.htm
[22] H. Li, Y.Z. Zhang, X.J. Pan, T. Wang, and E.Q. Xie, J. Alloys Compd., 472 (2009) 208.

Chapter 3

Effects of deposition parameters on structural and optical properties of ZnO thin films

3.1 Introduction

In terms of optoelectronic applications, ZnO is one of the most attractive semiconductors due to its promising properties, including a wide band gap of 3.37 eV at room temperature, a large excitation binding energy of 60 meV, chemical stability, and transparency, etc. The crystal quality is one of important issues which influence the commercial applications of ZnO based semiconductors. So far, a variety of techniques, such as pulsed laser deposition, molecular beam epitaxy, sputtering, and chemical vapor deposition, have been attempted to deposit high crystalline ZnO films. Among these deposition techniques the radio frequency (RF) magnetron sputtering is considered as the most convenient method to deposit reproducible and homogeneous ZnO thin films over a large-area substrate at a lower deposition temperature. It is found that the characteristics of ZnO films are generally affected by RF sputtering parameters, such as oxygen partial pressure [1-6], sputtering power [7-11], and deposition pressure [12,13], etc. Up to date, there are several publications regarding the effect of sputtering parameters on the properties of ZnO films. However, there has been short of report on the modulation of Zn-rich and O-rich films. Furthermore, there are few of systematical research on the band gap of ZnO film with different sputtering parameters. In this chapter, in order to solve the above issues, we reveal the effects of deposition parameters on the structural and optical properties of ZnO thin films, the deposition parameters dependence, such as gas ratio of Ar/O_2, sputtering power, and deposition pressure are carried out.

3.2 Gas ratio of Ar/O_2 dependence

3.2.1 Experiments

ZnO thin films with the thickness of 500 nm were deposited onto quartz glasses substrate by an rf (13.56 MHz) magnetron sputtering system. The deposition parameters of ZnO films are shown in Table 3.1. A 4-inch ZnO (5N) ceramic target was located on a cathode 60 mm away from the substrate stage. The substrate on an anode was heated and kept at 150 ºC before and during deposition and the chamber was evacuated to 7×10^{-5} Pa with a turbo molecular pump

and was kept at 1 Pa during all the depositions. During the sputtering process, an RF power was set consistently at 180 W, a mixture gas of argon and oxygen was introduced. The gas flows were controlled by mass flow meters to reveal the effects of gas ratio. I modified the Ar/O_2 ratio of 30/0, 10/5, 10/10, 10/30, and 0/30 sccm, respectively.

Table 3.1 Deposition parameters of ZnO thin films deposited at different Ar/O_2 ratios.

Target	ZnO (4 inch, 5N)
Substrates	Quartz glass
Working distance	60 mm
Temperature	150 ^oC
Deposition pressure	1 Pa
Ar/O_2 gas flow rate	30/0, 10/5, 10/10, 10/30, 0/30 sccm
RF power	180 W (2.4 W/cm^2)

3.2.2 Results and discussion

The deposition rates of the ZnO thin films remarkably decrease with the increase in the oxygen flow ratio corresponding to 13.77 nm/min for the deposition in pure argon approach to 5.02 nm/min for that in pure oxygen, as shown in Fig. 3.1. It might be due to that the bombardment effect of sputtering ions was weakened with increasing the oxygen flow ratio.

Figure 3.2(a) shows the XRD patterns of ZnO films deposited at different Ar/O_2 ratios. All as-deposited films exhibit a (002) diffraction peak, indicating that as-deposited films have a hexagonal wurtzite structure and are preferentially oriented along the c-axis perpendicular to the plane of the substrates. The intensity of (002) peak is significantly increased with the increase of oxygen ratio. Correspondingly, the full width at half-maximum (FWHM) of the (002) peak decreases as the oxygen ratio increases. The XRD result indicates that the crystallinity of the as-deposited ZnO films is improved with the increase oxygen ratio. The crystallite sizes in the c-axis, calculated using Scherrer's formula [14], increases from 21.0 nm for pure oxygen to 39.0 nm for pure argon deposition, as shown in Fig. 3.2(b).

The stress σ in films is calculated according to the following equation [15]:

$$\sigma = \left(2C_{13} - \frac{C_{11} + C_{12}}{C_{13}} \times C_{33}\right)\frac{c - c_0}{c_0} \qquad (3.1)$$

where c is the lattice parameter of c-axis of the films, c_0 is the lattice parameter of ZnO powder (c_0 = 5.206) [16], and C_{ij} are elastic stiffness constants. For ZnO, we obtain the values of C_{11} =

209.7 GPa, C_{12} = 121.1 GPa, C_{33} = 210.9 GPa, and C_{13} = 105.1 GPa. The values of *c* of films with hexagonal structure are extrapolated from the following relation:

$$d_{hkl} = \frac{1}{\sqrt{\frac{4}{3a^2(h^2+hk+k^2)} + \frac{l^2}{c^2}}} \quad (3.2)$$

where a and c are the lattice constants, and d_{hkl} is the lattice spacing of (*hkl*). The d_{hkl} can be calculated using the equation of $2d_{hkl}\sin\theta = \lambda$, where θ is the Bragg diffraction angle of the XRD peak and λ is the X-ray wavelength, β is the value of FWHM, respectively.

Figure 3.2(c) shows the peak position and deduced stress of ZnO films deposited at different Ar/O_2 ratios. The (002) peak of film deposited in pure argon ambient locates at $2\theta = 34.36^o$, which indicates that the film suffers compressive stress between the film and quartz substrate comparing with that of ZnO powder ($2\theta = 34.42^o$). The residual stress may be originated from the different thermal expansion coefficients between the film and substrate and intrinsic stress such as interstitial zinc and oxygen vacancy during depositing process [17]. When the oxygen is introduced into chamber during sputtering process, the peak position of ZnO thin films shifts to high angle of about 34.42^o compared with that of pure argon condition, which implies that the residual stress in ZnO films can be effectively reduced by introducing oxygen.

The morphologies of the as-deposited ZnO films are examined using an FE-SEM system, as shown in Fig. 3.3. It can be clearly observed that the as-deposited ZnO films have a uniform and smooth surface. The average grain size of the as-deposited films decreases from 170 to 60 nm with the oxygen ratio increases.

The resistivity of ZnO films was evaluated using conventional four-point probe technique with a resistivity meter (MCP-T610, Mitsubishi Chemical Corp.). The films resistivity decreases from 10^9 Ω cm for that in pure oxygen to 10^3 Ω cm for the deposition in pure argon. The decrease of oxygen ratio results in decreasing the film resistivity due to the much more un-reacted zinc atoms remained in formed film with the only argon gas sputtering ambient during the deposition process.

The transmittance spectra of ZnO films deposited at different Ar/O_2 ratios are shown in Fig. 3.4. The average transmittance of all ZnO films on the quartz glass is 80% in the visible region. The absorption edge obtained from ZnO thin films shifts to shorter wavelength with oxygen concentration increases. The optical band gap (E_g) of films can be determined by extrapolating the plot of $(\alpha hv)^2$ versus *hv*, as shown in Fig. 3.5. The evaluated band gaps of the as-deposited ZnO films are 3.285, 3.297, 3.297, 3.289, and 3.288 eV corresponding to the films deposited at Ar/O_2 ratio of 30/0, 10/5, 10/10, 10/30, and 0/30, respectively, which indicates that the band gap energy of the ZnO films is affected by the Ar/O_2 ratio.

3.2.3 Summary

ZnO films were deposited onto quartz glass substrates by RF magnetron sputtering. The structural, electrical, and optical properties of as-deposited ZnO films were strongly dependent on the Ar/O_2 ratio. The ZnO films had a hexagonal wurtzite structure and the crystallinity improved whereas the *c*-axis crystalline size increases with the increase of oxygen ratio. The film resistivity decreases with decreasing of oxygen ratio. All the ZnO thin films show about 80% optical transmissions in the visible region. The optical absorption edge is found to shift to the shorter wavelength with the increase of the oxygen ratio. Based on the investigation of properties of ZnO films deposited under different Ar/O_2 ratio, the Zn-rich or O-rich thin films can be adjusted simply during sputtering.

3.3 Sputtering power dependence

3.3.1 Experiments

ZnO thin films with the thickness of 500 nm were deposited onto quartz glasses substrate by an rf magnetron sputtering system. The deposition parameters of ZnO films are shown in Table 3.2. In order to investigate the effects of deposition power on the properties of ZnO films, the deposition power was varied from 60 to 240 W at an interval of 60 W.

Table 3.2 Deposition parameters of ZnO thin films deposited at different sputtering powers.

Target	ZnO (4 inch, 5N)
Substrates	Quartz glass
Working distance	60 mm
Temperature	150 ^oC
Deposition pressure	1 Pa
Ar/O_2 gas flow rate	10/30 sccm
RF power	60, 120, 180, 240 W

3.3.2 Results and discussion

The deposition rates of the ZnO thin films remarkably increase with the increase of sputtering power from 1.974 nm/min for the deposition at 60 W to 19.013 nm/min for the deposition at 240 W, as shown in Fig. 3.6. Figure 3.7(a) shows the XRD patterns of ZnO films deposited at

different sputtering power. All ZnO films exhibit a (002) diffraction peak, indicating that as-deposited films have a hexagonal wurtzite structure and are preferentially oriented along the c-axis perpendicular to the plane of the substrates. The intensity of (002) peak is significantly decreased with the increase of sputtering power. The peak position of films shifts from 34.25^{o} for the deposition power of 60 W to 34.00^{o} for the deposition power of 240 W. According to the (002) peak position of unstrained ZnO powder (2θ = 34.42^{o}), the all as-deposited films suffer the compressive stress. The FWHM of the (002) peak increases as the sputtering power increases. Correspondingly, the crystallite sizes in the c-axis decreases from 29.6 nm for the deposition at 60 W to 20.1 nm for the deposition at 240 W, as shown in Fig. 3.7(b). The XRD result indicates that the crystallinity of the as-deposited ZnO films is improved with the decrease sputtering power.

The morphologies of the as-deposited ZnO films are examined using an FE-SEM system, as shown in Fig. 3.8. It can be clearly observed that the as-deposited ZnO films have a uniform and smooth surface. The average grain size of the as-deposited films increases from 50 to 80 nm with the sputtering power increases from 60 to 240 W.

The transmittance spectra of ZnO films deposited at different sputtering power are shown in Fig. 3.9. The average transmittance of all ZnO films on the quartz glass is 80% in the visible region. The absorption edge obtained from ZnO thin films shifts to shorter wavelength with sputtering power increases. The optical band gap (E_g) of films can be determined by extrapolating the plot of $(\alpha hv)^2$ versus hv, as shown in Fig. 3.10. The evaluated band gaps of the as-deposited ZnO films are 3.267, 3.253, 3.244, and 3.248 eV corresponding to the films deposited uder the power of 60, 120, 180, and 240 W, respectively, which indicates that the band gap energy of the ZnO films is affected by the sputtering power.

3.3.3 Summary

ZnO films were deposited onto quartz glass substrates by RF magnetron sputtering. The ZnO films had a hexagonal wurtzite structure and the crystallinity improved whereas the *c*-axis crystalline size increases with the decrease of sputtering power. All the ZnO thin films show about 80% optical transmissions in the visible region. The optical absorption edge is found to shift to the shorter wavelength with the increase of the sputtering power. Based on the investigation of properties of ZnO films deposited under different sputtering power, the crystallinity and band gap of thin films can be adjusted simply during sputtering.

3.4 Deposition pressure dependence

3.4.1 Experiments

ZnO thin films with the thickness of 500 nm were deposited onto quartz glasses substrates. The deposition parameters of ZnO films are shown in Table 3.3. In order to investigate the effects of deposition pressure on the properties of ZnO films, the deposition pressure was varied from 1 to 7 Pa at an interval of 2 Pa.

Table 3.3 Deposition parameters of ZnO thin films deposited at different sputtering pressures.

Target	ZnO (4 inch, 5N)
Substrates	Quartz glass
Working distance	60 mm
Temperature	150 ^{o}C
Deposition pressure	1, 3, 5, 7 Pa
Ar/O_2 gas flow rate	10/30 sccm
RF power	180 W (2.4 W/cm^2)

3.4.2 Results and discussion

The deposition rate of the ZnO thin films remarkably decreases from 11.89 to 6.16 nm/min with the increase of the deposition pressure from 1 to 7 Pa, as shown in Fig 3.11, which might be due to that the bombardment effect of sputtering ions was weakened with increasing the sputtering pressure.

Figure 3.12(a) shows the XRD patterns of ZnO films deposited at different sputtering pressure. All ZnO films exhibit a (002) diffraction peak, indicating that as-deposited films have a hexagonal wurtzite structure and are preferentially oriented along the c-axis perpendicular to the plane of the substrates. The intensity of (002) peak is significantly increased with the increase of sputtering pressure. The peak position of films shifts from 33.94^{o} for the deposition pressure of 1Pa to 34.43^{o} for the deposition pressure of 7 Pa. According to the (002) peak position of unstrained ZnO powder (2θ = 34.42^{o}), the compressive stress is confirmed to be released with increasing sputtering pressure. The FWHM of the (002) peak decreases as the sputtering pressure increases. Correspondingly, the crystallite sizes in the c-axis decreases from 14.4 nm for the deposition at 1 Pa to 40.3 nm for the deposition at 7 Pa, as shown in Fig. 3.12(b). The XRD result indicates that the crystallinity of the as-deposited ZnO films is improved with the increase sputtering pressure.

The morphologies of the as-deposited ZnO films are examined using an FE-SEM system, as

shown in Fig. 3.13. It can be clearly observed that the as-deposited ZnO films have a uniform and smooth surface. The average grain size of the as-deposited films increases with the sputtering pressure increases, which is in well agreement with XRD measurements.

The transmittance spectra of ZnO films deposited at different sputtering pressure are shown in Fig. 3.14. The average transmittance of all ZnO films on the quartz glass is 80% in the visible region. The absorption edge obtained from ZnO thin films shifts to shorter wavelength with sputtering pressure increases. The optical band gap (E_g) of films can be determined by extrapolating the plot of $(\alpha hv)^2$ versus hv, as shown in Fig. 3.15. The evaluated band gaps of the as-deposited ZnO films are 3.244, 3.269, 3.273, and 3.271 eV corresponding to the films deposited uder the pressure of 1, 3, 5, and 7 Pa, respectively, which indicates that the band gap energy of the ZnO films is affected by the sputtering pressure.

3.4.3 Summary

ZnO films were deposited onto quartz glass substrates by RF magnetron sputtering. The ZnO films had a hexagonal wurtzite structure and the crystallinity improved whereas the *c*-axis crystalline size increases with the increase of sputtering pressure. All the ZnO thin films show about 80% optical transmissions in the visible region. The optical absorption edge is found to shift to the shorter wavelength with the increase of the sputtering pressure. Based on the investigation of properties of ZnO films deposited under different sputtering pressure, the band gap of thin films can be adjusted from 3.244 to 3.271 eV with sputtering pressure increase from 1 to 7 Pa.

3.5 Conclusions

In this chapter, ZnO films were deposited onto quartz glass substrates by RF magnetron sputtering. The structural and optical properties of as-deposited ZnO films were strongly dependent on the Ar/O_2 ratio, puttering power, and deposition pressure. The XRD patterns show that the ZnO films had a hexagonal wurtzite structure and the crystallinity can be controlled by adjusting deposition parameters. All the ZnO thin films show about 80% optical transmissions in the visible region. Based on the investigation of properties of ZnO films deposited under different deposition parameters, the Zn-rich or O-rich thin films can be adjusted simply during sputtering.

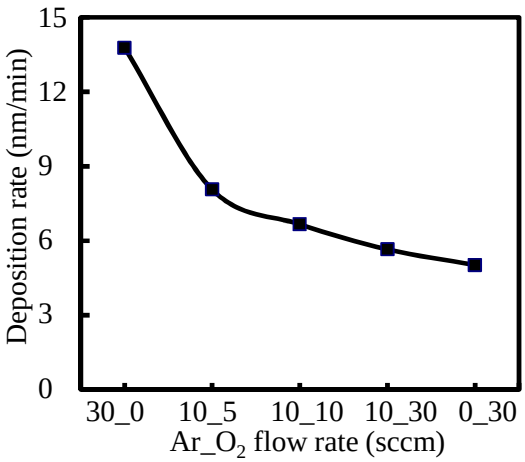

Fig. 3.1 Deposition rates of the ZnO thin films deposited at different Ar/O_2 ratios.

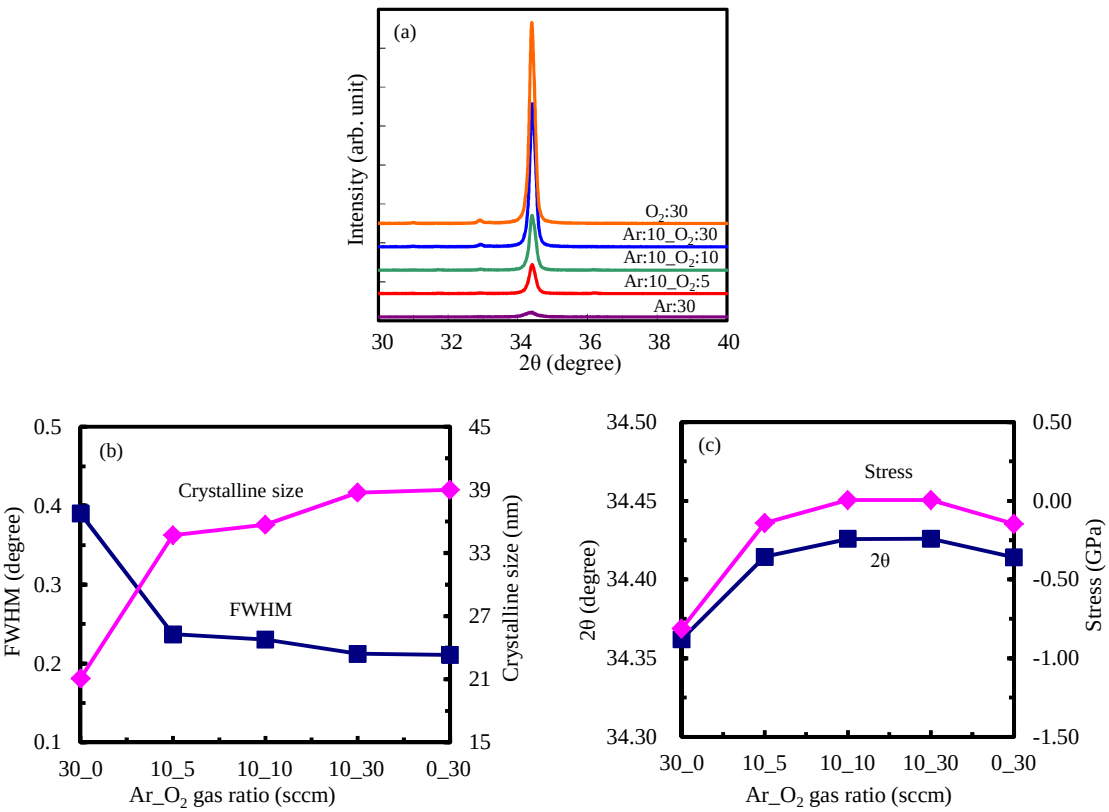

Fig. 3.2 (a) XRD patterns (b) FWHM and c-axis crystalline size (c) the peak position and deduced stress of ZnO films deposited at different Ar/O_2 ratios.

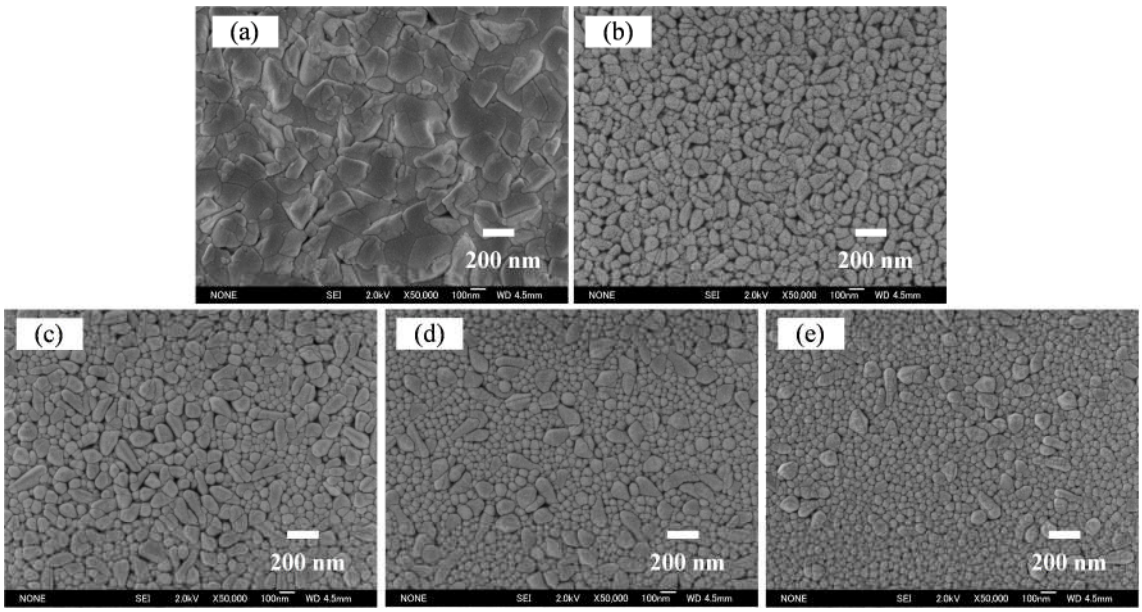

Fig. 3.3 SEM images of the ZnO thin films deposited at different Ar/O_2 ratios of (a) 30/0 (b) 10/5 (c) 10/10 (d) 10/30 and (e) 0/30.

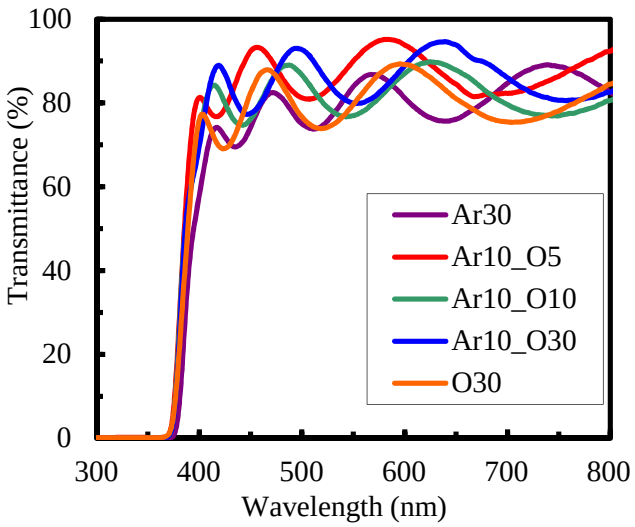

Fig. 3.4 The transmittance spectra of the ZnO thin films deposited at different Ar/O_2 ratios.

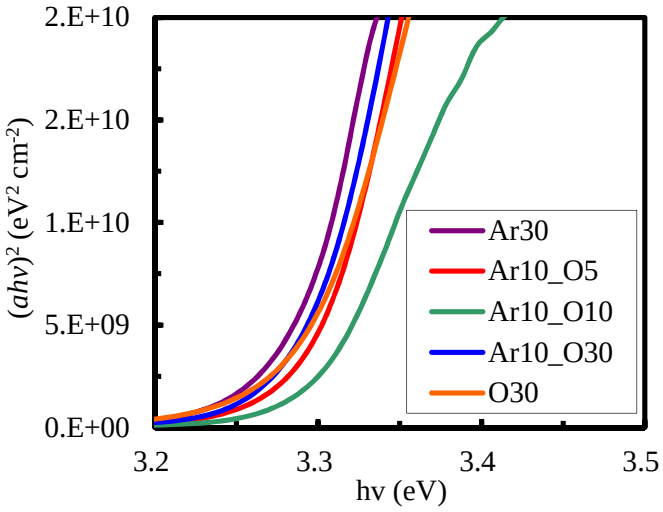

Fig. 3.5 Variation of $(\alpha h\upsilon)^2$ of the ZnO thin films deposited at different Ar/O_2 ratios as a function of the photon energy ($h\upsilon$).

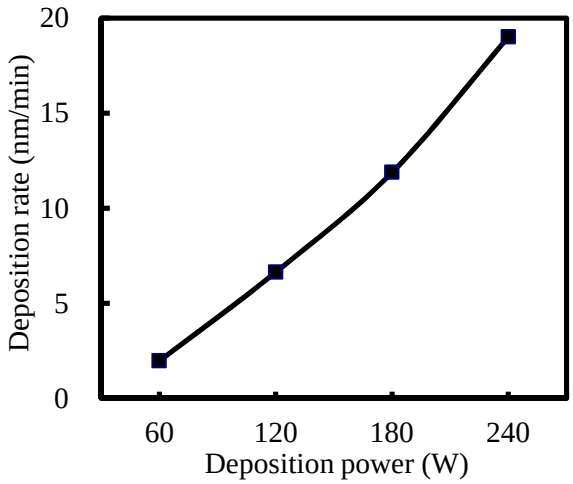

Fig. 3.6 Deposition rates of the ZnO thin films deposited at different sputtering powers.

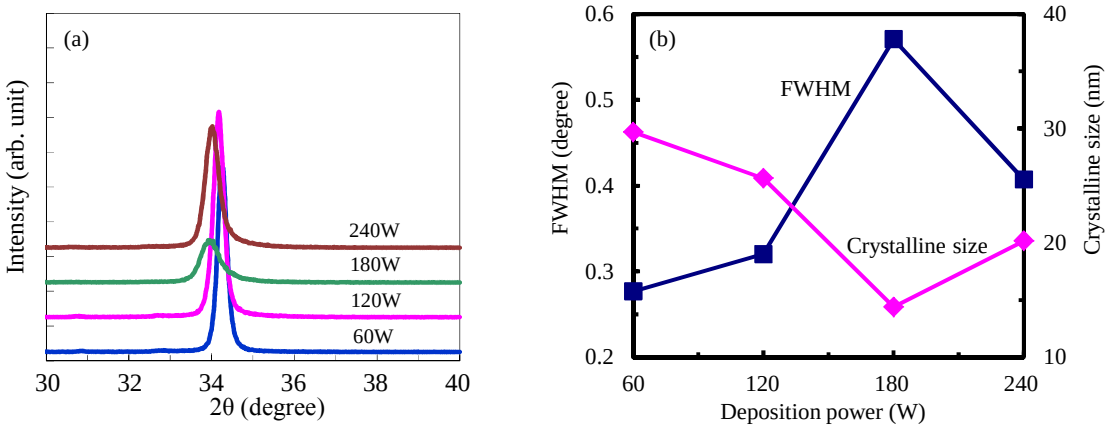

Fig. 3.7 (a) XRD patterns and (b) FWHM and c-axis crystalline size of ZnO films deposited at different sputtering powers.

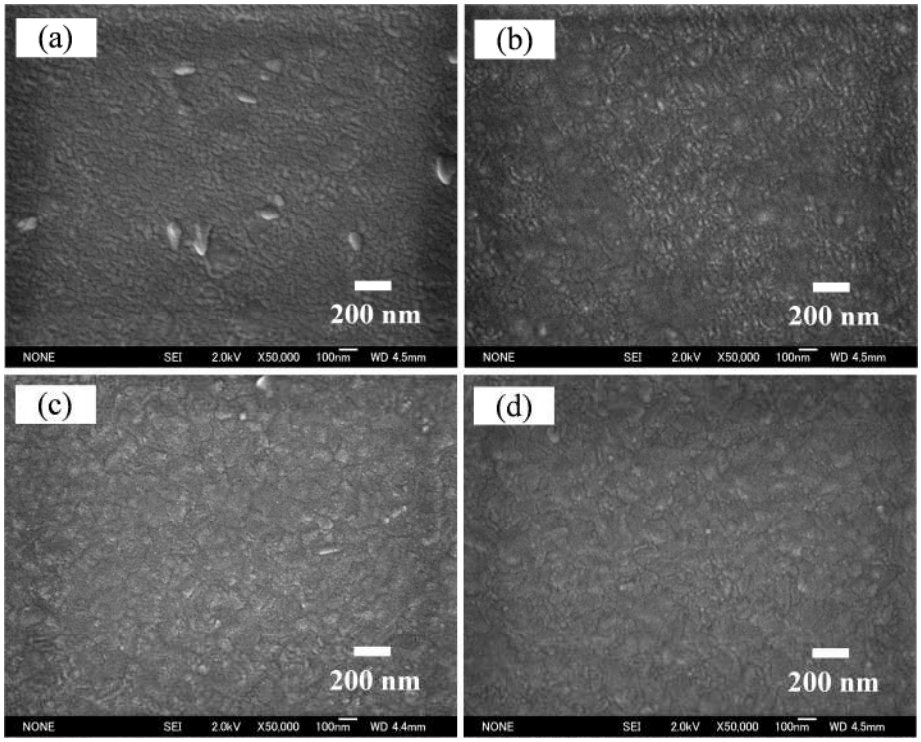

Fig. 3.8 SEM images of the ZnO thin films deposited at different sputtering powers of (a) 60 W (b) 120 W (c) 180 W and (d) 240 W.

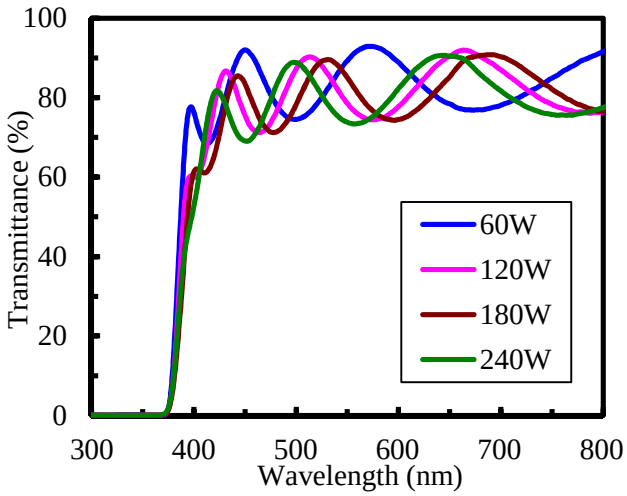

Fig. 3.9 The transmittance spectra of the ZnO thin films deposited at different sputtering powers.

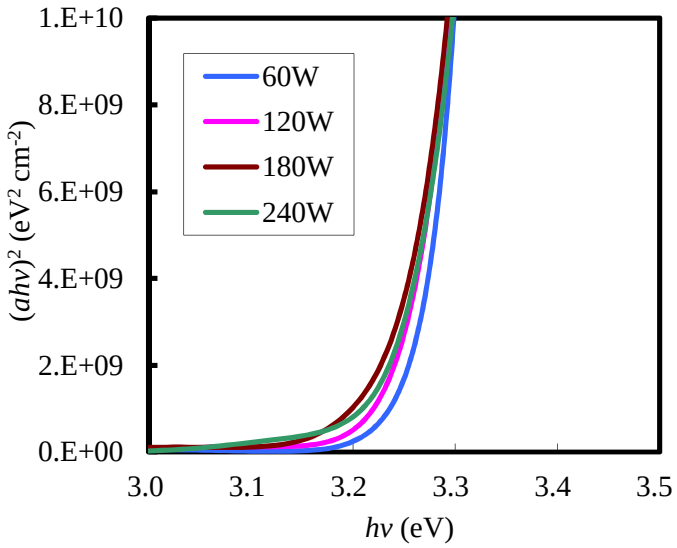

Fig. 3.10 Variation of $(\alpha h\upsilon)^2$ of the ZnO thin films deposited at different sputtering powers as a function of the photon energy ($h\upsilon$).

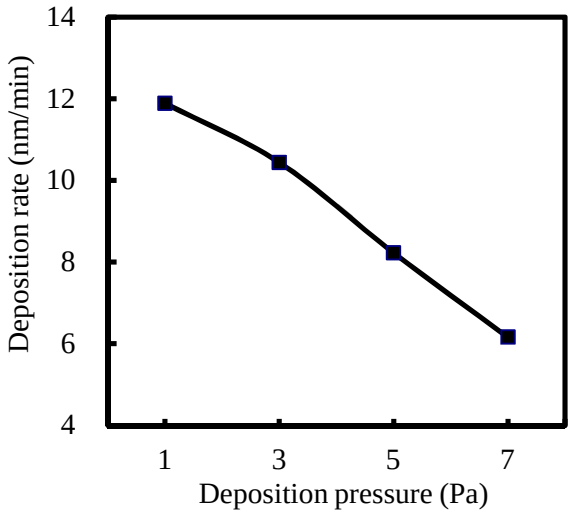

Fig. 3.11 Deposition rates of the ZnO thin films deposited at different sputtering pressures.

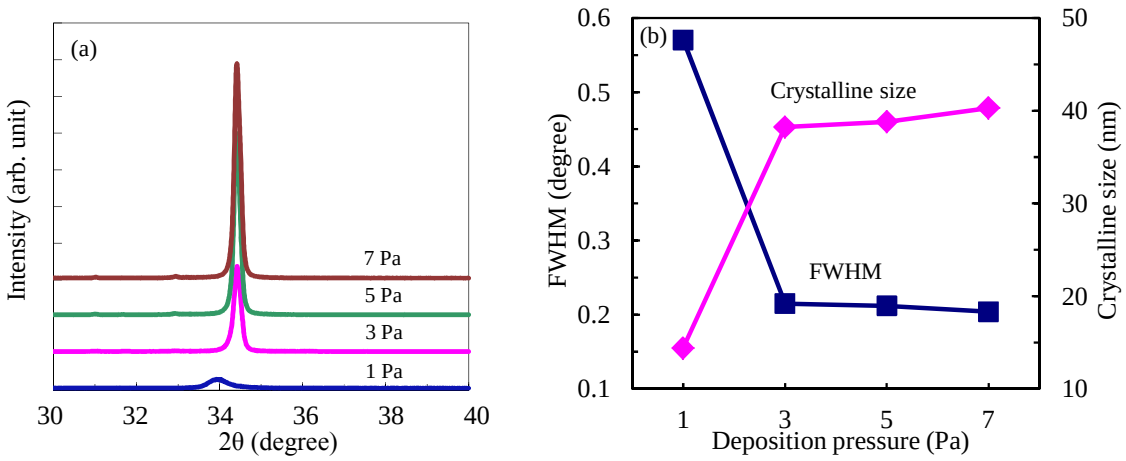

Fig. 3.12 (a) XRD patterns and (b) FWHM and c-axis crystalline size of ZnO films deposited at different sputtering pressures.

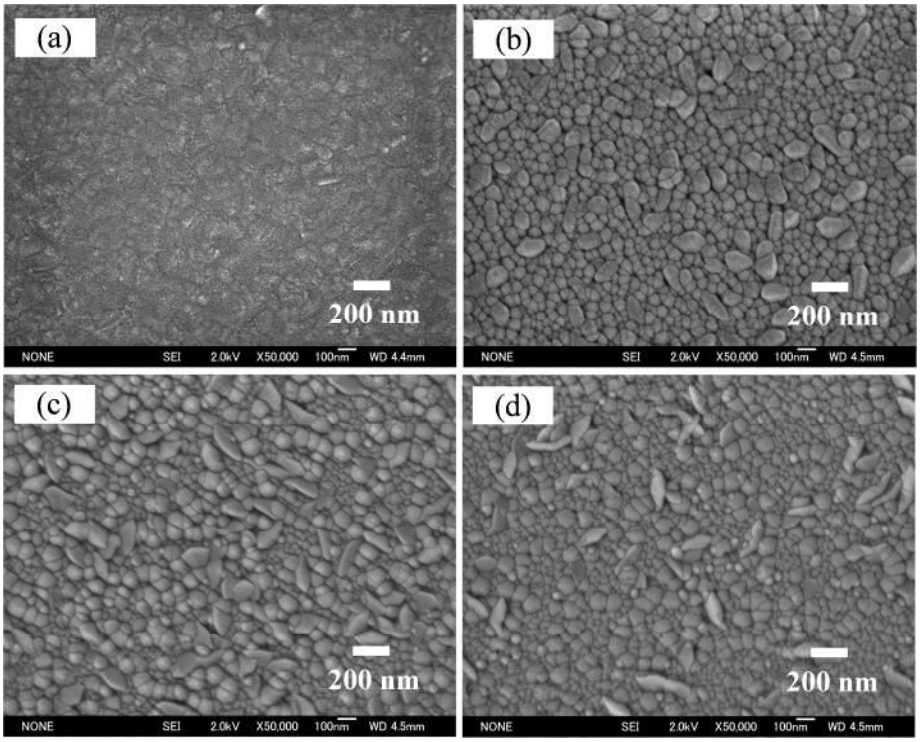

Fig. 3.13 SEM images of the ZnO thin films deposited at different sputtering pressures of (a) 1 Pa (b) 3 Pa (c) 5 Pa and (d) 7 Pa.

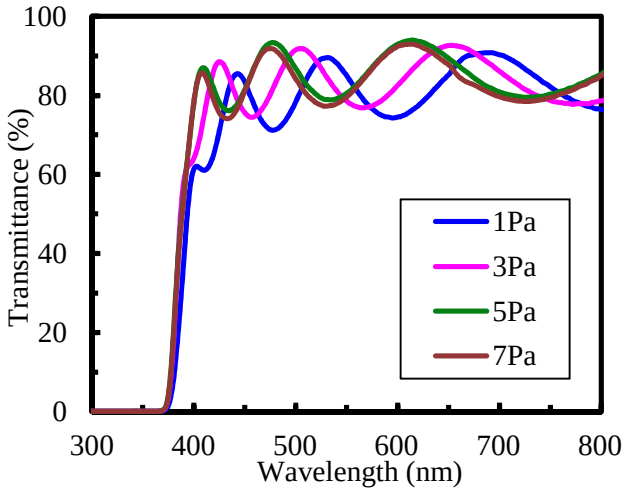

Fig. 3.14 The transmittance spectra of the ZnO thin films deposited at different sputtering pressures.

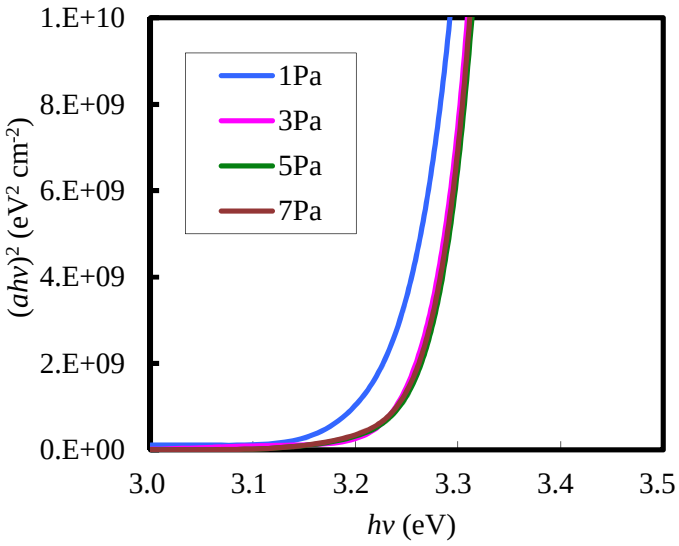

Fig. 3.15 Variation of $(\alpha h\upsilon)^2$ of the ZnO thin films deposited at different sputtering pressures as a function of the photon energy ($h\upsilon$).

3.6 References

[1] T. Tsuji and M. Hirohashi, Appl. Surf. Sci., 157 (2000) 47.

[2] R. Hong, H. Qi, J. Huang, H. He, Z. Fan, and J. Shao, Thin Solid Films, 473 (2005) 58.

[3] Y. Ma, G.T. Du, T.P. Yang, D.L. Qiu, X. Zhang, H.J. Yang, Y.T. Zhang, B.J. Zhao, and X.T. Yang, J. Cryst. Growth, 255 (2003) 303.

[4] A.V. Singh, R.M. Mehra, A. Wakahara, and A. Yoshida, J. Appl. Phys., 93 (2003) 396.

[5] P. Singh, A.K. Chawla, D. Kaur, and R. Chandra, Mater. Lett., 61 (2007) 2050.

[6] J.J. Chen, Y. Gao, F. Zeng, D.M. Li, and F. Pan,

[7] X. Yu, J. Ma, F. Ji, Y. Wang, X. Zhang, C. Cheng, and H. Ma, J. Cryst. Growth, 274 (2005) 474.

[8] Y.M. Lu, W.S. Hwang, W.Y. Liu, and J.S. Yang, Mater. Chem. Phys., 72 (2001) 269.

[9] J. Lee, D. Lee, D. Lim, and K. Yang, Thin Solid Films, 515 (2007) 6094.

[10] K. Ahn, Y. Yang, and M.A. Jassim, J. Vac. Sci. Technol. B, 25 (2007) L23.

[11] X. Yu, J. Ma, F. Ji, Y. Wang, X. Zhang, C. Cheng, and H. Ma, Appl. Surf. Sci., 239 (2005) 222.

[12] O. Kluth, B. Rech, L. Houben, S. Wieder, G. Schope, C. Beneking, H. Wagner, A. Loffl, H.W. Schock, Thin Solid Films, 351 (1999) 247.

[13] S.B. Krupanidhi and M. Sayer, J. Appl. Phys., 56 (1984) 3308.

[14] V. Gupta and A. Mansingh, J. Appl. Phys., 80 (1996) 1063.

[15] D. Singh and Y.P. Varshni, Phys. Rev. B, 24 (1981) 4340.

[16] R.D. Vispute, V. Talyansky, S. Choopun, R.P. Sharma, T. Venkatesan, M. He, X. Tang, J.B. Halpern, M.G. Spencer, Y.X. Li, L.G. Salamanca-Riba, A.A. Iliadis, and K.A. Jones, Appl. Phys. Lett., 73 348 (1998) 348.

[17] B.L. Zhu, X.Z. Zhao, F.H. Su, G.H. Li, X.G. Wu, J. Wu, and R. Wu, Vacuum, 84 (2010) 1280.

Chapter 4

Fabrication and characterization of ZnO:Mg thin films

4.1 Introduction

ZnO has attracted considerable attentions in optoelectronic applications such as light emitting devices, UV sensors and laser diodes due to its promising properties including a wide band gap of 3.37 eV at room temperature and a large excitation binding energy of 60 meV, a chemical stability and a transparency, etc. For commercial applications of ZnO based semiconductors, an important issue is the realization of band gap engineering in a wide range. One can modulate the band gap of a ZnO by alloying it with a semiconductor that has a different band gap to form a ternary compound. $Zn_{1-x}Mg_xO$ has been widely investigated because its band gap can be modulated from 3.37 (for wurtzite ZnO) to 7.9 eV (for rock-salt MgO). The similarity of the ionic radius between Mg^{2+} (0.57 Å) and Zn^{2+} (0.60 Å) allows the substitution of one another without causing significant changes in a lattice structure [1]. So far, ZnMgO films have been prepared by various techniques, such as pulsed laser deposition (PLD), molecular beam epitaxy (MBE), RF sputtering etc. Among these techniques RF sputtering is considered as a technique to fabricate high quality thin film over a large-area substrate at a lower deposition temperature. Han *et al*. [2] have realized a high Mg concentration between 0.70 to 0.84 by changing RF power. Li *et al*. have investigated the effects of thermal annealing on Mg concentration ($0.10 \leq x \leq 0.14$) in $Zn_{1-x}Mg_xO$ films. Although RF sputtering method is extensively applied for modulating Mg concentration in a ZnMgO film, there are few reports on the effects of deposition pressure on structural and optical properties of $Zn_{1-x}Mg_xO$ thin films deposited at a low temperature.

After reviewing the ZnMgO related publications, I found that many studies have been concentrated on controlling the Mg ratio, high temperature treatment, etc. Nevertheless, a high temperature process is not suitable for the process on glass substrates due to the low glass transition temperatures. In this case, extensive applications of ZnMgO thin film in industrial processes are limited. Therefore, there is still much work remaining for process improvement of preparing ZnMgO thin film.

In this research, we deposited the different $Zn_{1-x}Mg_xO$ thin films with different Mg content ceramic targets by RF magnetron sputtering. $Zn_{1-x}Mg_xO$ (x=0.3) thin films under a variable deposition pressure were prepared. The effects of deposition pressure on the structural and

optical properties of ZnMgO thin films were investigated. For the $Zn_{1-x}Mg_xO$ (x=0.1) thin films, there are two ways to treat ZnMgO thin films. One is to study the effects of different post-annealing ambient on structural and optical properties of ZnMgO films. Another is to investigate the optical properties of ZnMgO thin film with ZnO as buffer layer has been carried out to explore its characteristics as a luminescent material for display devices. ZnO and ZnMgO thin films were also fabricated for comparison.

4.2 Influence of sputtering pressure on band gap of ZnO:Mg (Mg = 0.3) thin films

4.2.1 Experiments

$Zn_{1-x}Mg_xO$ films (500 nm in thickness) were deposited onto quartz glass by an RF (13.56 MHz) magnetron sputtering system using a 4-inch ZnO/MgO (70/30 wt %) ceramic target. The deposition parameters of ZnMgO films are shown in Table 4.1. The substrate on an anode was heated and kept at 150 ºC before and during deposition and the chamber was evacuated to 8×10^{-5} Pa with a turbo molecular pump. During the sputtering process, an RF power was set consistently at 180 W, a mixture gas of oxygen and argon was introduced at a flow ratio of Ar/O_2 = 10sccm/30sccm, controlled by mass flow meters. In order to investigate the effects of deposition pressure on the properties of $Zn_{1-x}Mg_xO$ films, the deposition pressure was varied from 1 to 9 Pa at an interval of 2 Pa.

Table 4.1 Deposition parameters of ZnMgO thin films deposited at different sputtering pressures.

Target	ZnO/MgO (70/30 wt.%, 4 inch)
Substrates	Quartz glass
Working distance	88 mm
Temperature	150 °C
Deposition pressure	1, 3, 5, 7, 9 Pa
Ar/O_2 gas flow rate	10/30 sccm
RF power	180 W (2.4 W/cm^2)

4.2.2 Results and discussion

Figure 4.1 shows the dependence of deposition rate on the deposition pressure. It was observed that the deposition rate of the $Zn_{1-x}Mg_xO$ thin films remarkably decreased from 4.50 to 2.06 nm/min with the increase of the deposition pressure from 1 to 9 Pa, which might be due to that the bombardment effect of sputtering ions was weakened with increasing sputtering pressure [3,4].

Figure 4.2 shows the XRD patterns of the $Zn_{1-x}Mg_xO$ thin films prepared under different deposition pressures. The ZnMgO films exhibit single rock-salt cubic structure and only the (200) peak can be observed from the films deposited under a low pressure (1 - 5 Pa). With the decrease of the deposition pressure, the MgO (200) peak shifts to a higher diffraction angle with the increase of the Mg concentration, indicating that Zn^{2+} ions are successfully substituted by Mg^{2+} ions. When the films deposited under a high pressure (7 and 9 Pa), only the (002) peak of the ZnMgO film was observed, indicating that the ZnMgO alloy exhibited the ZnO hexagonal wurtzite structure and MgO phase separation was not formed. With deposition pressure decreases, the ZnMgO (002) peak slightly shifts to a higher diffraction angle. This shift suggests that the c-axis lattice constant decreased with the increase in Mg concentration because of the relatively lower ionic radii of Mg.

Rutherford backscattering/ion channeling techniques were used to determine the chemical composition. The Rutherford backscattering (RBS) was taken using a probe beam of 2.0 MeV He^+ ions, with a surface barrier detector positioned at 165º. Figure 4.3 shows the typical RBS spectra of the $Zn_{1-x}Mg_xO$ thin films deposited with changing pressure. It is found that the $Zn_{1-x}Mg_xO$ films are composed of O, Zn and Mg. The composition of the films was then determined from the Mg/Zn peak height ratios in RBS spectrum by quantitative analysis [5]. Figure 4.4 shows the calculated atomic ratios of Mg concentration *x* in all films as a function of the deposition pressure. The RBS results reveal that the Mg concentration in the $Zn_{1-x}Mg_xO$ thin films decreased from 0.531 to 0.472 as the deposition pressure increased from 1 to 5 Pa, and then further decreased from 0.478 to 0.467 as the deposition pressure increased from 7 to 9 Pa. Therefore, the RBS results demonstrate that the Mg concentration in the ZnMgO films could be modulated by varying the deposition pressure.

The Mg concentration change in the $Zn_{1-x}Mg_xO$ thin films prepared under different deposition pressures is in well agreement with the crystallite phase transformation from wurtzite to cubic structure obtained from the XRD measurement. The decrease of the Mg concentration in the ZnMgO thin films with the increase in the deposition pressure can be considered due to the scattering effect. During the deposition processes, the Mg related species can be scattered more easily than that of Zn in the sputtering gas ambient due to the relative atomic mass of Mg (24.31) is lighter than that of Zn (65.39). Under a lower sputtering pressure (1 - 5 Pa) the ejected species including the sputtered ions and ion clusters from the target experience fewer collisions and

scatterings with the sputtering gas atoms prior to collision with substrate, leading to higher deposition rate and Mg concentration in ZnMgO films. In contrast, the increased collisions and scatterings under a higher deposition pressure (7 and 9 Pa) contribute to the decrease in the deposition rate and Mg concentration, result in less Mg occupation of the position of Zn, corresponding to reduction of Mg incorporation efficiency, meanwhile, increase of Zn concentration in the films. The Mg concentration of the ZnMgO film deposited under 7 Pa is the critical value, from which the crystal structure of hexagonal wurtzite changed to cubic rock-salt structure in the sputtering processes. This tendency of the Mg concentration changing in the ZnMgO films agrees with the results of XRD measurements.

The transmittance spectra of the $Zn_{1-x}Mg_xO$ films prepared under different deposition pressures are shown in Fig. 4.5. The transmittances for all the ZnMgO films on the quartz glass are around 85% in visible region. The absorption edge obtained from the ZnMgO films shifts to higher wavelengths with the decrease of Mg concentration. It is observed that the slope becomes gentle near the absorption edges as the deposition pressure becomes lower than 5 Pa. However, the films deposited under a higher pressure (7 and 9 Pa) exist a sharp absorption edge in the UV region.

The absorption edge could be used to evaluate the band gap of the $Zn_{1-x}Mg_xO$ films. The relationship between the absorption coefficient and the photon energy can be expressed as following equation:

$$(\alpha h\nu)^2 = A(h\nu - E_g) \qquad (4.1)$$

where A and E_g represent the constant and the band gap of a film. The absorption coefficient (α) could be obtained from the transmittance $T = A\exp(-\alpha d)$, where A and d are constant and thickness of the film, respectively. The band gap (E_g) is determined by extrapolation of the linear portion to the photon energy axis at $(\alpha h\upsilon)^2 = 0$.

Figure 4.6 shows $(\alpha h\upsilon)^2$ plots of the ZnMgO films as a function of the photon energy ($h\upsilon$). The evaluated band gaps of the $Zn_{1-x}Mg_xO$ thin films are 5.23, 5.16, 5.10, 4.33 and 4.30 eV corresponding to the deposition pressure of 1, 3, 5, 7 and 9 Pa, respectively, which indicates that the band gap energy of the ZnMgO thin films decreases with increasing deposition pressure. Particularly, the band gap energy decreases to approach that of a ZnO film when the deposition pressure increases to 7 and 9 Pa. Therefore, modulation of the band gap of the ZnMgO thin films could be achieved by controlling the deposition pressure during the RF sputtering process.

4.2.3 Summary

The deposition pressure was found to be an important parameter on the structural and optical properties of the $Zn_{1-x}Mg_xO$ films which were prepared on quartz substrates by RF magnetron

sputtering. The Mg concentration in the ZnMgO thin films increased with decreasing deposition pressure from 9 to 1 Pa, and the crystal structure varied from hexagonal wurtzite to cubic rock-salt correspondingly when Mg concentration $x \geq 0.482$. Furthermore, the band gap of the ZnMgO films increased from 4.30 to 5.23 eV significantly while the deposition pressure decreased. Therefore, it was possible to control the crystalline structure and the band gap of the ZnMgO films by simply adjusting the deposition pressure in the RF magnetron sputtering process.

4.3 Post-treatment effects on the structural and optical properties of ZnO:Mg (Mg = 0.1) thin films

4.3.1 Experiments

ZnMgO thin films with a nominal thickness of 300 nm were deposited onto silicon (100) substrate using a RF (13.56 MHz) magnetron sputtering system. ZnO/MgO (90/10 wt.%) target (4-inch) was located on the cathode which was 88 mm away the substrate stage. Prior to deposition, the chamber was evacuated to 10^{-5} Pa with a turbo molecular pump and the substrate on anode was preheated at 150 °C for one hour. A gas mixture of Ar/O_2 (10/30 sccm) was used as working gases. The composition was regulated by mass flow controllers. The RF power and working pressure were kept constant as 180 W and 1 Pa, respectively.

Table 4.2 Deposition and post-treatment parameters of ZnMgO thin films.

Target	ZnO/MgO (90/10 wt.%, 4 inch)
Substrates	p-type Silicon(100) (0.02 Ω·cm)
Temperature	150 °C
Deposition pressure	1 Pa
Ar/O_2 gas flow rate	10/30 sccm
RF power	180 W (2.4 W/cm^2)
Annealing gas	O_2, N_2, Forming gas (H_2 in N_2: 1.9%)
Temperature	500 °C
Annealing time	5 h

After Three kinds of atmospheres including O_2, N_2, or forming gas (H_2 in N_2: 1.9%) were respectively compared at the same annealing condition. The annealing temperature was

increased from room temperature to 500 °C at 25°C/min and was kept for 5 h under a pressure of 10 kPa, and then it was decreased to the ambient temperature. The Deposition and post-treatment parameters of ZnMgO films are shown in Table 4.2.

4.3.2 Results and discussion

Figure 4.7(a) shows the θ/2θ XRD patterns of $Zn_{0.9}Mg_{0.1}O$ films on Si (100) substrates both as-deposited and annealed under different ambient. It was found that only ZnO (002) diffraction peak was observed for both as-deposited and annealed films, implying a polycrystalline wurtzite crystal structure with a highly preferred *c*-axis orientation due to low content of Mg. The 2θ diffraction angle of 33.84° for as-deposited ZnMgO thin film indicated that the film is homogeneously distorted due to large lattice mismatch and thermal expansion coefficient differences between substrate and film. However, 2θ diffraction angles for annealed ZnMgO thin films were 34.68°, 34.52° and 34.54°, corresponding to the films annealed in H_2/N_2, N_2 and O_2 ambient, which might be attributed to the decrease in lattice spacing after annealed at 500°C except the annealing defect recovery effect [6]. The intensities were improved gradually in the films annealed in N_2, O_2, H_2/N_2 ambient, and the integral intensity of ZnMgO film annealed in H_2/N_2 was ten times stronger than that of as-deposited film. Furthermore, the FWHM value obtained from ZnMgO film annealed in H_2/N_2 was 0.2801°, which was smaller than those values obtained from as-deposited and films annealed in N_2 and O_2, as shown in Fig. 7(b). It revealed that an improved crystallinity can be obtained from the H_2/N_2 annealing than those from N_2 and O_2 annealing ambient. Crystallite size could be calculated by means of the Scherrer's equation. It was found that the crystallite sizes of ZnMgO followed the increased order of as-deposited, annealed in N_2, O_2, and H_2/N_2 ambient, the corresponding values as 9.17, 20.53, 22.27 and 29.38 nm, respectively. These results confirmed that increased crystallite size was attributed to the improved crystallinity due to suitable post-treatment.

Figure 4.8 shows the surface morphologies of as-deposited ZnMgO thin film and annealed films at different ambient at 500 °C for 5 h. Dense and textured microstructures could be observed for all films. It is clearly observed that alloyed ZnMgO grains were distributed randomly on films after annealing, which indicated that ZnMgO alloy coalesced easily after annealing. The film annealed in H_2/N_2 showed the most uniformly and largest average grain size of about 70 nm comparing with those from as-deposited film (50 nm), which revealed that the crystallinities of annealed ZnMgO thin films were improved. The results, together with the XRD results, indicated that crystallinity was influenced by annealing ambient.

Figure 4.9 shows PL spectra obtained from ZnMgO films from both as-deposited and annealed in different gas ambient. The PL results indicate that post-annealing contributes to the

enhancement of PL intensity. All of annealed films exhibited both emission peaks from a narrow near band edge emission (NBE) and a broad deep level emission (DLE). The two superimposed peaks were shown in visible light range of annealing films, at 520 nm and 620 nm. The 620 nm peak corresponds to the red emission from the silicon background [7]. The green emission at 520 nm was contributed by transition from energy levels caused by oxygen vacancies related defect centers. The introduction of Mg into ZnO film could not change the defects level position in the forbidden band, and the corresponding position of visible emission did not change either except the intensity. The intensity of the visible light emission was significantly enhanced from the ZnMgO film annealed in the forming gas H_2/N_2 comparing with those from N_2, or O_2 annealing ambient, which implied that native defects decreased and the larger number of oxygen vacancies increased due to reducing gas annealing. The ZnMgO thin film annealed in N_2 ambient indicated that the oxygen vacancies were not easily degraded during annealing. As ZnMgO thin film annealed in O_2 ambient, more oxygen was introduced into the film and compensated the oxygen defects, so that the intensity of visible emission became weaker. A considerably enhanced NBE (365 nm) emission was also observed for the film annealed in H_2/N_2 ambient, which might be attributed to a decrease of nonradiative recombination defects and an increase of nonradiative recombination lifetime due to H_2/N_2 annealing. However, the NBE emission was suppressed from the ZnMgO films annealed in N_2, or O_2 ambient. The ratio of NBE emission peak intensity to DLE peak intensity was considerably large in film annealed in H_2/N_2 ambient compared to those of films annealed in N_2, or O_2 ambient, which indicated that the crystal quality of film improved under H_2/N_2 annealing.

4.3.3 Summary

The $Zn_{0.9}Mg_{0.1}O$ thin film was deposited on silicon (100) substrate using the RF magnetron sputtering. The effects of post-annealing in H_2/N_2, N_2, or O_2 atmospheres on structural and optical properties of ZnMgO films were studied. The most improved crystallinity was found from the film annealed in H_2/N_2 ambient at 500 °C for 5 h, corresponding to the increased grain size. Moreover, the PL intensities with peak range around 520-620 nm was increased remarkably for the film annealed in reducing gas as well.

4.4 Characterization of multiple layers of ZnMgO/ZnO (Mg = 0.1) thin films

4.4.1. Experiments

ZnMgO film with ZnO buffer layer (200/100 nm in thickness), ZnMgO and ZnO with a thickness of 300 nm were respectively deposited onto a p-type Si (100) substrate by a conventional 13.56 MHz RF magnetron sputtering system using a 4-inch $Zn_{0.9}Mg_{0.1}O$ target. The ZnO buffer layer was deposited using the same rf system except for using ZnO target (5N). The background pressure in the sputtering chamber was evacuated to about 5×10^{-5} Pa with a turbo molecular pump and kept at a constant deposition pressure of 1 Pa during all the depositions. The deposition processes were performed in an ambient of oxygen and argon mixture. The gas ratio (Ar/O_2: 10/30 sccm) was controlled by a mass flow meter to compare the effect of the different gas ratios. The RF sputtering was performed at a power of 180 W for each deposition. The substrate temperature on the anode was preheated to 150 ^oC for 1 h prior to deposition and was kept during the deposition processes.

Table 4.3 Deposition and post-treatment parameters of ZnMgO/ZnO thin films.

Target	ZnO (5N, 4 inch) ZnO/MgO (90/10 wt.%, 4 inch)
Substrates	p-type Silicon(100) (0.02 Ω·cm)
Temperature	150 ^oC
Deposition pressure	1 Pa
Ar/O_2 gas flow rate	10/30 sccm
RF power	180 W (2.4 W/cm^2)
Annealing gas	Forming gas (H_2 in N_2: 1.9%)
Temperature	500 ^oC
Annealing time	2 h

After the preparation, above three kinds of thin films, ZnMgO/ZnO, ZnMgO, and ZnO, were annealed in a conventional furnace annealing system. After evacuated to 5×10^{-3} Pa, a forming gas (H_2 in N_2: 1.9%) was introduced into the furnace from room temperature to 500 ^oC at 10 ^oC/min and kept for 2 h at a stable annealing pressure of 10 kPa, and then cooled down to the ambient temperature in the vacuum chamber. The Deposition and post-treatment parameters of ZnMgO/ZnO films are shown in Table 4.3.

4.4.2. Results and discussion

Figure 4.10 shows a comparison of the XRD patterns of the as-deposited and films annealed

in the forming gas for 2 h. Both the as-deposited and annealed films were found to have a c-axis orientation and all exhibited a single phase of ZnO hexagonal wurtzite structure without MgO signals. According to Fig. 4.10(a), the ZnMgO/ZnO and ZnMgO thin films had better crystallinization than that of ZnO because the bond energy between Mg and O_2 (531.2 eV) is large than that between Zn and O_2 (530.2 eV). As a result, Mg is easier to bond with O_2. Figure 4.10(b) shows that the crystallinities of all the annealed samples were enhanced, with the higher angle shifted for ZnMgO/ZnO (34.56^o) and ZnMgO (34.66^o) thin films compared to ZnO, which means that Zn^{2+} ions in the ZnO lattice were replaced partially with Mg^{2+} ions due to their smaller radius, the decrease of the lattice constant along the c-axis resulted in the higher angle shift. Considering the full-width at half-maximum (FWHM), the ZnMgO/ZnO (0.34^o) which might due to the superposition of ZnO (002) and ZnMgO (002) diffraction peaks. The formation of the ZnMgO/ZnO heterostructure was confirmed.

Figure 4.11 shows the morphologies of the as-deposited and annealed samples examined with a FE-SEM. It was found that all the as-deposited thin films, as shown in Fig. 4.11(a)-(c), exhibited uniform and flat surface. Unexpectedly, nanostructures appeared vertically on the ZnMgO film with ZnO as buffer layer after annealing in the reducing gas. From the top view, it was found the nanorods with uniform hexagonal heads (diameter about 100 nm) densely distributed on the ZnO film. The average length of the nanorods was about 300 nm which was obtained from the scratched nanorods on the surface, as shown in an insert plot of Fig. 4.11(e). There were no nanostructures observed except that the grain size slightly increased on the ZnMgO thin film. There were also nanostructures with random orientations formed on the ZnO thin film, however the crystal grains were destroyed by the reactions between ZnO and H_2 during the annealing process, compared with the annealed thin films, as shown in Fig. 4.11(e)-(f). From the comparison of above SEM images, it was obviously that the formation of the hexagonal nanorods was contributed by the ZnO buffer layer on which the ZnMgO thin film served as a suitable protection layer.

During the annealing process, the ZnO buffer layer would be easily dissociated than ZnMgO would be due to the difference in the melting points (ZnO: 420 ^{o}C, ZnMgO: 630 ^{o}C). It was possible that zinc ions (from reduced ZnO) or atoms (from as-deposited film) would diffuse into the upper layer of the ZnMgO thin film when annealed at 500 ^{o}C. The zinc particles would serve as catalyst particles, distributing among the ZnMgO particles for ZnO re-crystallization growth. Meanwhile, the ZnO vapor species were absorbed on the top of the formed nanorods, as it was the energetically favored area. The hexagonally structural heads arose to maintain the minimum surface energy and the crystal symmetry of the wurtzied ZnO.

Figure 4.12 shows a comparison of PL measurement results obtained from the three kinds of annealed thin films. Apparently, the near band edge emission peak of 357 nm from ZnMgO/ZnO

was significantly suppressed and shifted to higher band energies compared to that from the ZnO of 375 nm. Unexpectedly, there were very broaden peaks with wavelength from 480 to 700 nm observed for both ZnMgO thin film with ZnO as buffer layer as well as ZnMgO thin film annealed in the reducing ambient, which was nearly in white color from naked eyes, implying that an increased number of Mg diffused into the ZnO film to create acceptors to trap holes and to produce enhanced luminescence.

4.4.3. Summary

ZnMgO thin film was prepared on p-type Si (100) substrate with ZnO thin film as buffer layer using RF magnetron sputtering method. It was found hexagonal naorods with 100 nm in diameter and 300 nm in length could be formed vertically on the ZnMgO after annealing in a reducing ambient at a low temperature about 500 ^{o}C for 2 h. The crystallinity of ZnMgO on ZnO was improved due to Mg substitution in the ZnO film. A broaden PL emission peak (around 480-700nm) was observed from ZnMgO/ZnO multiples structures. In contrast, the band to band emission was suppressed.

4.5 Conclusions

In this work, ZnMgO thin films with different Mg concentrations had been deposited on quartz or silicon substrates by using RF magnetron sputtering.

1) ZnMgO (Mg = 0.3) thin films were prepared under deposition pressure from 1 to 9 Pa at an interval of 2 Pa. XRD patterns indicated that the crystal structure varied from hexagonal wurtzite to cubic rock-salt with decreasing deposition pressure from 9 to 1 Pa. Corresponding to the Mg concentration in the ZnMgO thin films increased from 0.467 to 0.531 due to the scattering effect, which were confirmed by RBS measurement. Furthermore, the band gap of the ZnMgO films increased from 4.30 to 5.23 eV significantly while the deposition pressure decreased. Therefore, the crystalline structure and the band gap of the ZnMgO films can be simply adjusted by modulating the deposition pressure in the RF magnetron sputtering process.

2) ZnMgO (Mg = 0.1) thin film was deposited on p-type Si (100) substrate. After the preparation, the effects of post-annealing in H_2/N_2, N_2, or O_2 atmospheres on structural and optical properties of ZnMgO films were studied. The most improved crystallinity was found from the film annealed in H_2/N_2 ambient at 500 °C for 5 h, corresponding to the increased grain size. Moreover, the PL intensity with peak range around 520-620 nm was increased remarkably for the film annealed in reducing gas.

3) ZnMgO/ZnO, ZnO, ZnMgO (Mg = 0.1) thin film were prepared on p-type Si (100) substrate with ZnO thin film as buffer layer. The hexagonal naorods with 100 nm in diameter and 300 nm in length were formed vertically on the ZnMgO after annealing in a reducing ambient at a low temperature of 500 ^{o}C for 2 h. The crystallinity of ZnMgO/ZnO was improved due to Mg substitution in the ZnO film. A broaden PL emission peak from 480 to 700nm was observed from ZnMgO/ZnO multiple layer while the near band emission was suppressed. These results revealed that ZnMgO/ZnO multiple layer will be a potential candidate for white-light LED, displays, and other optical devices.

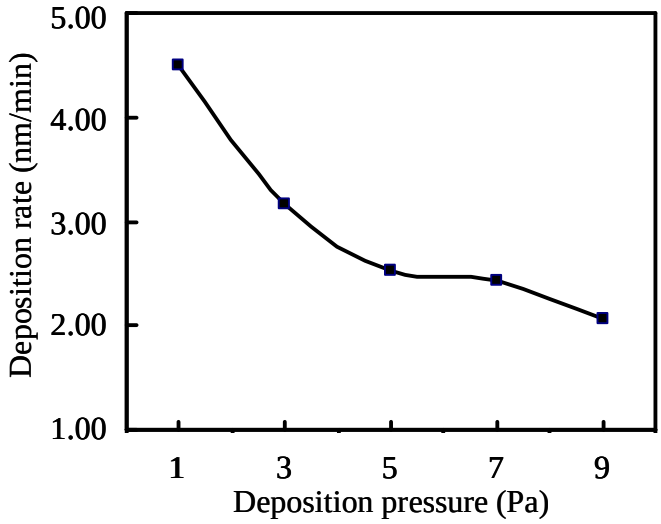

Fig. 4.1 Dependence of the deposition rate of the $Zn_{1-x}Mg_xO$ films on the deposition pressure.

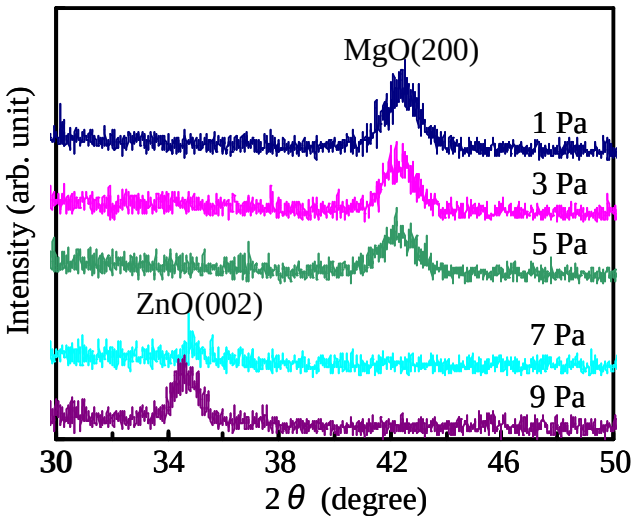

Fig. 4.2 XRD spectra of the $Zn_{1-x}Mg_xO$ thin films prepared on the quartz substrates under the deposition pressure from 1 to 9 Pa.

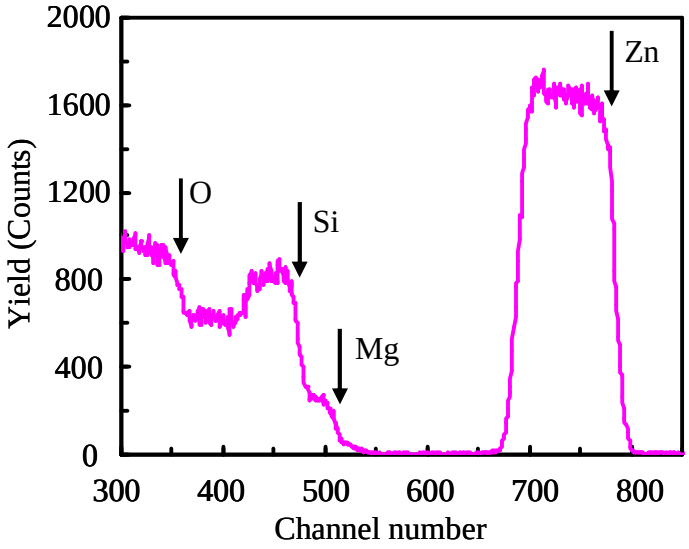

Fig. 4.3 RBS spectra of the $Zn_{1-x}Mg_xO$ thin films deposited under different pressures.

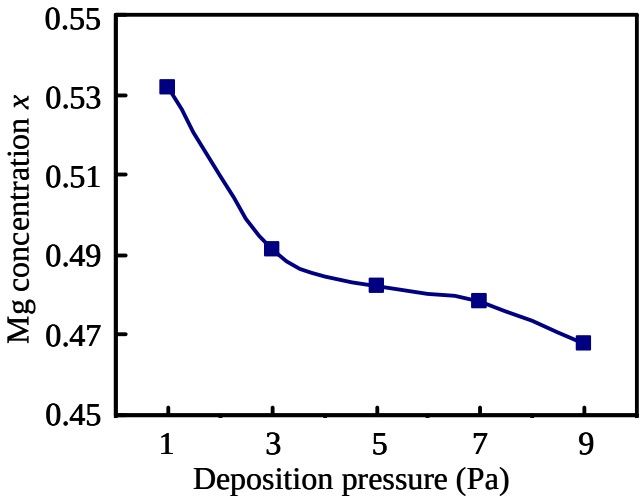

Fig. 4.4 The calculated Mg concentration of the $Zn_{1-x}Mg_xO$ films on the deposition pressure.

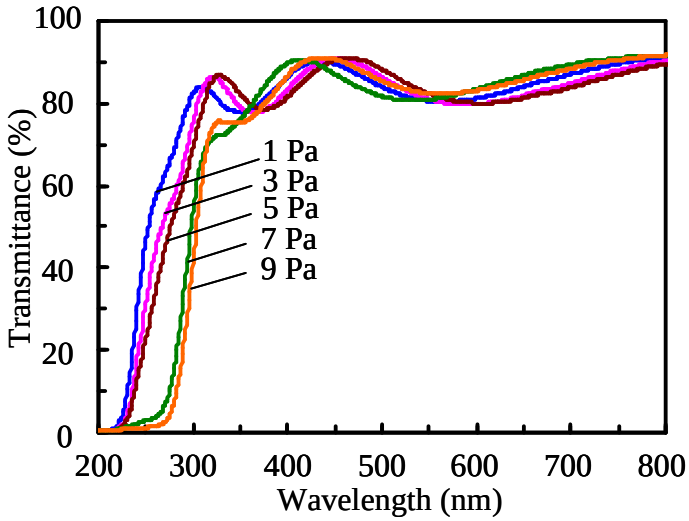

Fig. 4.5 Transmittance spectra of the $Zn_{1-x}Mg_xO$ thin films prepared under different deposition pressures.

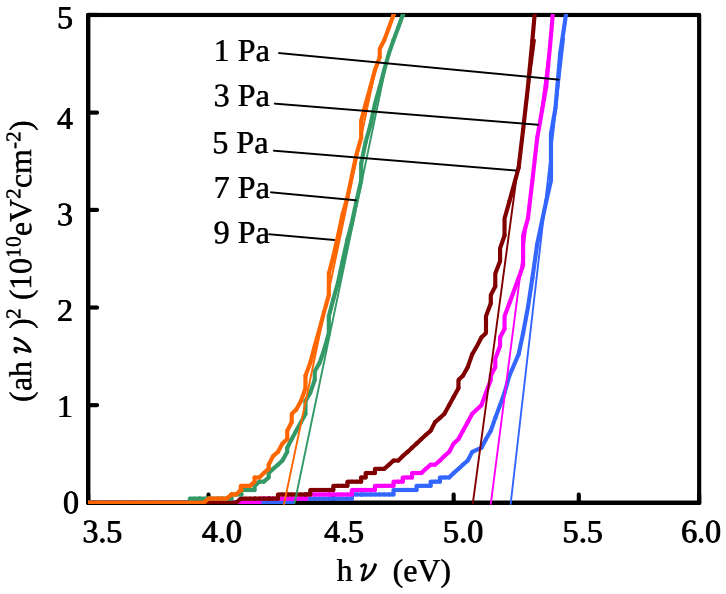

Fig. 4.6 Variation of $(\alpha h\upsilon)^2$ of the $Zn_{1-x}Mg_xO$ thin films as a function of the photon energy ($h\upsilon$).

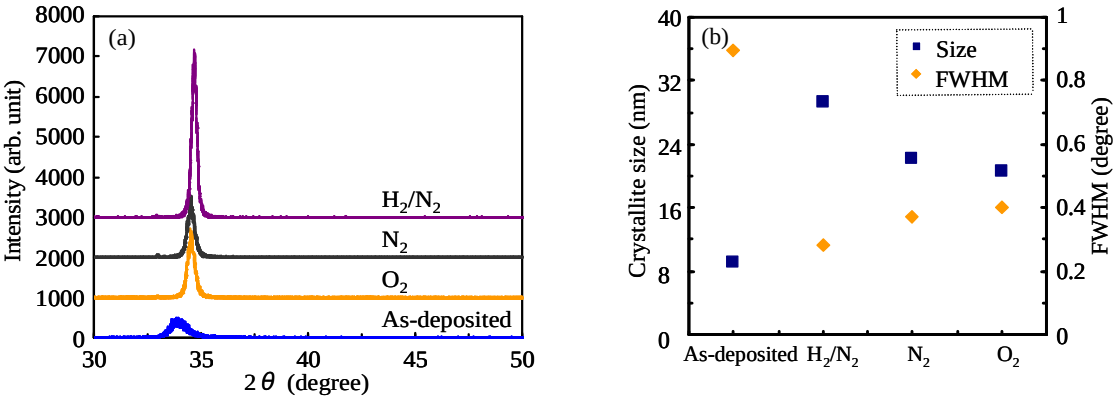

Fig. 4.7 (a) XRD patterns (b) comparison of c-axis crystallite size, FWHM, peaks and intensities values of as-deposited and annealed ZnMgO thin films in H_2/N_2, N_2 and O_2 ambient at 500 ^oC for 5 h.

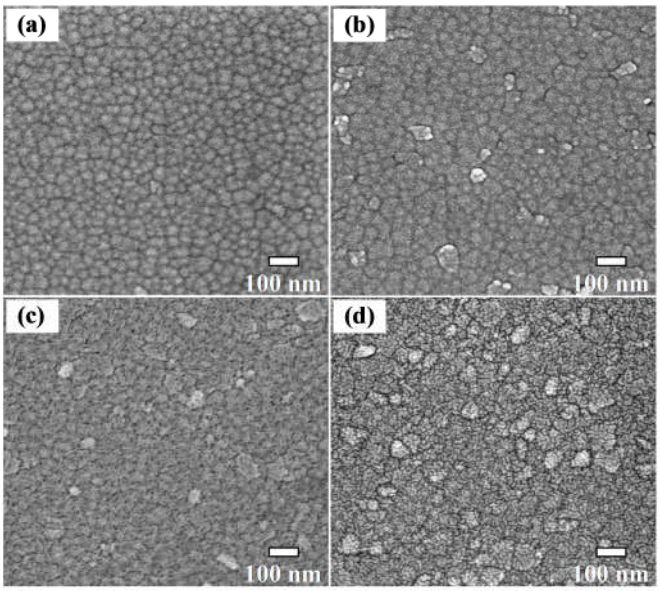

Fig. 4.8 SEM images of the ZnMgO thin films (a) as-deposited, and annealed in different ambient (b) H_2/N_2, (c) N_2 and (d) O_2 at 500 ^oC for 5 h.

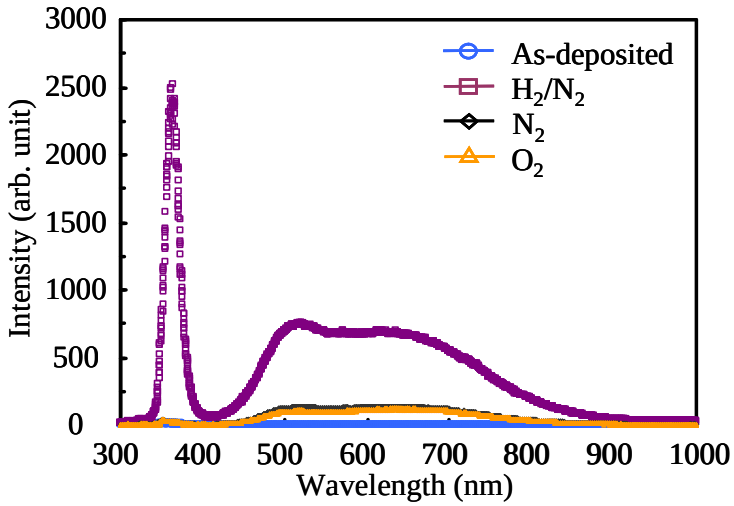

Fig. 4.9 PL spectra of the ZnMgO thin films obtained from as-deposited and annealed in different ambient at 500 ºC for 5 h.

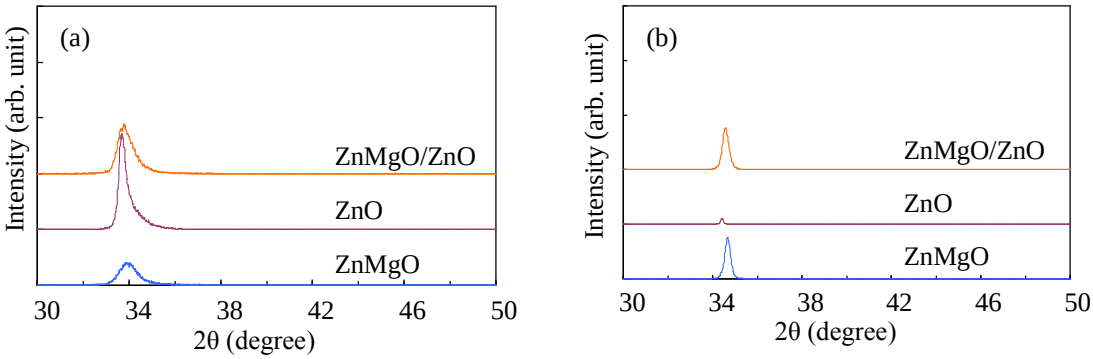

Fig. 4.10 XRD patterns of ZnMgO/ZnO, ZnO, ZnMgO films deposited on Si (100) substrates (a) as-deposited (b) annealed in forming gas (N_2 in H_2: 1.9%) at 500 ºC for 2 h.

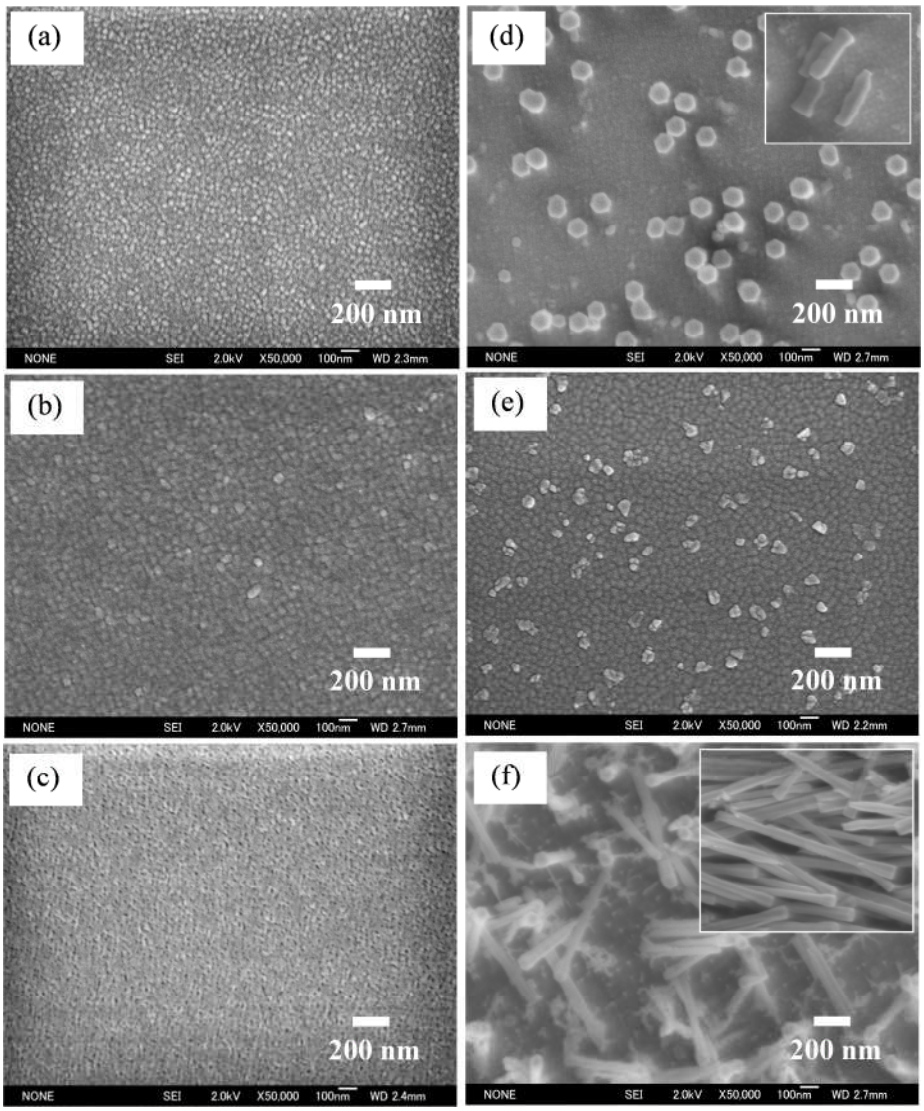

Fig. 4.11 SEM images of as-deposited thin films (a) ZnMgO/ZnO (b) ZnMgO (c) ZnO and annealed in forming gas (N_2 in H_2: 1.9%) at 500 ºC for 2 h (d) ZnMgO/ZnO (e) ZnMgO (f) ZnO.

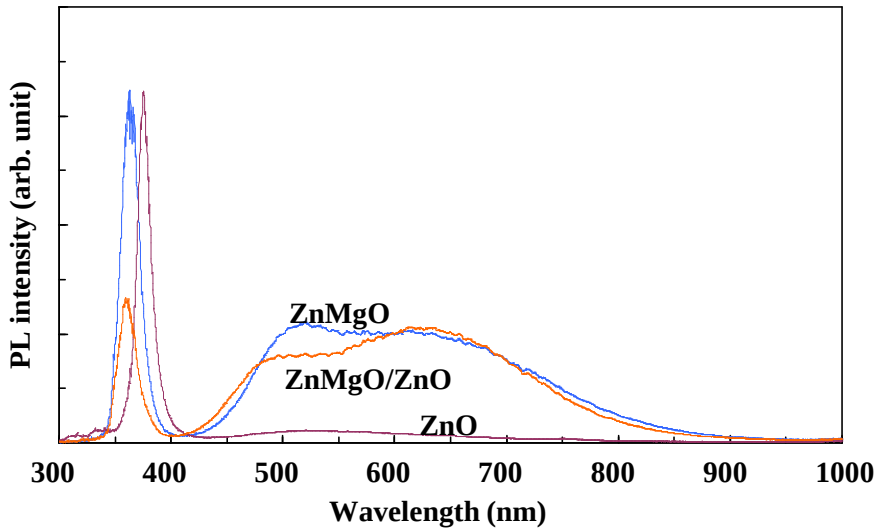

Fig. 4.12 PL spectra of ZnMgO/ZnO, ZnO and ZnMgO thin films annealed in forming gas at 500 ºC for 2 h.

4.6 References

[1] R.D. Shannon, Acta Crystallogr. Sect. A: Cryst. Phys. Diffr. Theor. Gen. Crystallogr., 32, (1976) 751.

[2] S. Han, D.Z. Shen, J.Y. Zhang, Y.M. Zhao, D.Y. Jiang, Z.G. Ju, D.X. Zhao, and B. Yao, J. Alloys Compd., 485 (2009) 794.

[3] V. Assuncao, E. Fortunato, A. Marques, H. Aguas, I. Ferreira, M.E.V. Costa, and R. Martins, Thin Solid Films, 427 (2000) 401.

[4] H. Zhu, J. Hupkes, E. Bunte, A. Gerber, and S.M. Huang, Thin Solid Films, 518 (2010) 4997.

[5] L.C. Feldman and J.W. Mayer, “Fundamentals of Surface and Thin Film Analysis” (Elsevier, North-Holland, 1986) Chap. 3, pp. 55.

[6] S. Kumar, V. Gupte, and k. Sreenivas, J. Phys. Condens. Matter, 18 (2006) 3343.

[7] X. Wu, A. Bek, A.M. Bittner, C. Eggs, C. Ossadnik, and S. Veprek, Thin Solid Films, 425 (2003) 175.

Chapter 5

Fabrication and characterization of nanostructured ZnO thin films

5.1 Introduction

Zinc oxide (ZnO), a wide direct band gap semiconductor with large exciton binding energy (60 meV) at room temperature, is one of the most promising II-VI compound semiconductors for optoelectronic devices [1]. Among the various ZnO-related nanostructures, one dimensional ZnO nanostructures have received increasing attention due to their properties and their potential application for nanodevices [2, 3]. Currently ZnO nanostructure for optoelectronic device applications is one of the major nanoscience researches.

In terms of commercial applications, the crystalline morphology, orientation and shape of ZnO nanostructures should be well controlled during the treatment processes. ZnO nanostructures are grown using several methods [4-6], such as pulsed laser deposition, chemical vapor deposition, and electrochemical deposition. However, the preparation of ZnO nanostructures always suffers the complex processes, high temperatures, and small area fabrication, which unable for industrial applications. It is well-known that high temperature processing is not suitable for glass substrates due to the low glass transition temperatures. Although the aqueous chemical method is usually carried out at very low temperature, the reproducibility of ZnO nanostructures is a big issue by this method. Therefore, a technique for producing well-arrayed and controllable nanostructured ZnO thin film is still needed.

In our previous research [7], we succeeded in forming ZnO nanostructures using reducing annealing. In this chapter, nanostructured ZnO thin films were formed by optimizing the post-treatment time in reducing gas. The following study is to control the number of ZnO nanostructures by modulating the thickness of as-deposited ZnO thin film. In order to further control and produce well-arrayed ZnO nanostructures, we developed a novel low temperature multi-annealing process, which combines a reducing annealing process and oxygen annealing process. Multi-annealing processes were investigated for further understanding of the growth and luminescent mechanisms of ZnO nanostructures. The high crystallinity and big surface of nanostructured ZnO films were formed by the firstly optimized condition in reducing ambient. The effects of single or multiple

post-treatment on the structural and optical properties of ZnO nanostructures were investigated. This study may give significant impetus to produce well-arrayed ZnO nanostructures for future industrial applications.

5.2 Nanostructured ZnO thin films formed by single post-treatment process

5.2.1 Effects of annealing time on the structural and optical properties of ZnO thin film

5.2.1.1 Experiments

ZnO thin film with the thickness of 500 nm was deposited onto quartz glasses substrate by an RF magnetron sputtering system. A ZnO (5N) ceramic target was located on a cathode 88 mm away from the substrate stage. The substrate on an anode was heated and kept at 150 ºC before and during deposition and the chamber was evacuated to 10^{-5} Pa with a turbo molecular pump. Argon as the only working gas was introduced into the chamber at a flow rate of 30 scm and was kept at 7 Pa during all the depositions. During the sputtering process, an RF power was set consistently at 180 W. The deposition and post-treatment parameters of ZnO thin films annealed for different time are shown in Table 5.1.

Table 5.1 Deposition and post-treatment parameters of ZnO thin films annealed for different time.

Target	ZnO (5N, 4 inch)
Substrates	Quartz glass
Temperature	150 ºC
Deposition pressure	7 Pa
Ar gas flow rate	30 sccm
RF power	180 W (2.4 W/cm^2)
Annealing gas	Forming gas (H_2 in N_2: 1.9%)
Temperature	430 ºC
Annealing time	2, 5, 8 h

Following the deposition process, the deposited films were annealed in a reducing gas ambient (H_2 in N_2: 1.9%) with a conventional furnace system. The annealing temperature was

increased from room temperature to 430 ^{o}C with a rising rate of 10 ^{o}C/min at a stable annealing pressure of 50 kPa, and then cooled down to room temperature in the vacuum chamber. In order to investigate the effects of different annealing time on the properties of ZnO films, the ZnO films were annealed for 2, 5 and 8 h, respectively.

5.2.1.2 Results and discussion

Figure 5.1(a) shows the XRD patterns of ZnO thin film and ZnO nanostructures obtained by different annealing time. It is obvious that the (002) diffraction peak is oriented highly perpendicular to the plane of the substrate for as-deposited ZnO film and nanostructures. The (002) peak intensity is gradually increased up to the film annealed for 5 h, and then slightly decreases after annealing for 8 h. Fig. 5.1(b) shows the position and the full width at half-maximum (FWHM) of the (002) diffraction peaks varied with different annealing time. The peak position of as-deposited film shifts from 34.37° to higher angle of 34.54°, 34.54° and 34.52° after annealing for 2, 5 and 8 h, respectively. According to the (002) peak position of unstrained ZnO powder (2θ = 34.42°), the compressive stress suffered as-deposited ZnO thin film releases the stress to tensile along the interfaces after annealing. The FWHM values of (002) diffraction peak sharply decreases from 0.37° of as-deposited film to 0.29° after annealing for 5 h, and then slightly increases to 0.33° after annealing for 8 h, which indicates the crystallinity of the ZnO films is significantly improved after annealing for 5 h.

The morphologies of the as-deposited ZnO thin film and ZnO nanostructures were examined using a FE-SEM system, as shown in Fig. 5.2. It can be clearly observed that the as-deposited ZnO film has a uniform and smooth surface. The average grain size of as-deposited film is about 60 nm. After annealing in forming gas, ZnO nanostructures are formed on the ZnO films. It is clearly observed that the only small amount of ZnO nanostructures appear after annealing for 2 h, furthermore, the density of ZnO nanostructures is slightly increased after annealing for 5 h, and then slightly decrease after annealing for 8 h. After annealing, formed ZnO nanorods obtained from 2 and 8 h exhibit the uniform hexagonal heads (about 100 nm and 120 nm in diameter respectively) and height (about 350 nm and 700 nm, respectively). The average diameter of the stems of the ZnO nanostructures increased from 100 nm at the bottom to about 300 nm at the top hexagonal heads from 5 h annealing. Thus, it is confirmed that the regrowth of ZnO nanostructures are much efficient than that from 2 h annealing. However, It is also noticed that there is etching phenomenon happens after annealing for 8 h, which is the reason why the diameter of nanostructures decreases. Because the over etching happened in the first step annealing, the etching is also observed from ZnO thin film in the SEM image for 8 h, the shape of nanostructures changes to nanorods. In our experiences, the regrowth of ZnO

nanostructures relies on the several parameters during annealing processes, in which the annealing time is one of the important parameters for optimizing ZnO nanostructures. It is found that the annealing time of 5 h is suitable to form big surface nanostructures.

Figure 5.3 shows the PL spectra of as-deposited ZnO film and ZnO nanostructrures annealed with different annealing time. The intensity of UV emission at about 378 nm significantly increases after annealing for 2 h compared with as-deposited ZnO film, and then further increases after 5 h annealing, finally slightly decreases after annealing for 8 h. It is well-known that the UV emission is related to the crystalline quality, corresponds to the exciton emission from near conduction band to valence band. This result is in well agreement with XRD measurements. Moreover, little visible range luminescence is observed from the as-deposited ZnO film due to its poor crystallinity. After annealing for 2 h, a broad green emission with a peak centered at about 497 nm is obtained, which means that the oxygen vacancies are introduced by the reducing ambient annealing. Furthermore, the intensity of green emission is significantly enhanced after annealing for 5 h while the peak position little shifts, which indicates that much more oxygen vacancies remain on the bigger hexagonal heads and greater height. However, the intensity of deep level emission decreases after annealing for 8 h without peak position shifting.

It is well-accepted that the green emission from ZnO thin films arises from oxygen vacancy related defect centers in the films. Comparing the ZnO nanostructures formed in the different annealing time, it is obvious that the PL properties strongly depend on the nanostructures formed by different annealing time. After annealing in the reducing gas for 3 h, the oxygen vacancies are slightly introduced by the reducing reaction, which remain into the formed ZnO nanorods. Furthermore, ZnO nanostructures with bigger surface are formed after annealing for 5 h, which means the much more oxygen vacancies are introduced into the film, contributing to the higher PL intensity. Consequently, ZnO nanorods with slightly increasing height appear again after annealing 8 h, which result in the lower intensity of green emission compared to that of 5 h annealing.

5.2.1.3 Summary

In this study, the highest green emission peak centered at 497 nm is obtained from the ZnO nanostructures annealed for the optimum annealing time of 5 h. Therefore, it can assume that the much more oxygen vacancies might be produced and existed on the ZnO nanostructures which have much larger appearance area, result in the enhancement of PL peak in the visible range. The ZnO film annealed for optimizing annealing time of 5 h also exhibit the better crystallinity, which is in well agreement with XRD measurements.

5.2.2 Influence of thickness on the structural and optical properties of ZnO thin film

5.2.2.1 Experiments

ZnO films were prepared onto quartz glasses by an RF magnetron sputtering system using a 4-inch ZnO (99.999% purity) ceramic target. The substrate on an anode was heated and kept at 150 ºC before and during deposition. Before the deposition the chamber was evacuated to 8×10^{-5} Pa with a turbo molecular pump. During the sputtering process, argon as the only working gas was introduced into the chamber at a flow rate of 30 sccm. An RF power was set consistently at 180 W for the target under a deposition pressure of 7 Pa.

In order to investigate the effects of different thicknesses on the properties of ZnO films, the ZnO films were prepared with the thickness of 250, 500, 750, and 1000 nm, respectively. Following the depositions, the deposited films were annealed in a reducing gas ambient (H_2 in N_2: 1.9%) with a conventional furnace system. The annealing temperature was increased from room temperature to 430 ^{o}C with a rising rate of 10 ^{o}C/min and kept for 8 h at a stable annealing pressure of 50 kPa, and then cooled down to room temperature in the vacuum chamber. The deposition and post-treatment parameters of ZnO thin films deposited with different thickness are shown in Table 5.2.

Table 5.2 Deposition and post-treatment parameters of ZnO thin films deposited with different thickness.

Target	ZnO (5N, 4 inch)
Substrates	Quartz glass
Temperature	150 ^{o}C
Deposition pressure	7 Pa
Ar gas flow rate	30 sccm
RF power	180 W (2.4 W/cm^2)
Thickness	250, 500, 750, 1000 nm
Annealing gas	Forming gas (H_2 in N_2: 1.9%)
Temperature	430 ^{o}C
Annealing time	8 h

5.2.2.2 Results and discussion

Figure 5.4(a) shows the XRD patterns of the as-deposited ZnO films with different thicknesses. All films exhibit a (002) diffraction peak at about 34.3^{o}, indicating that as-deposited films have a hexagonal wurtzite structure and are preferentially oriented along the c-axis perpendicular to the plane of the substrates. The intensity of (002) peak is significantly increased with the increase of film thickness. Correspondingly, the full width at half-maximum (FWHM) of the (002) peak decreases as the film thickness increases. In addition, the crystallite sizes in the c-axis, calculated using Scherrer's formula, increases from 17.6 to 20.6 nm, as shown in of Fig 5.4(b). The XRD result indicates that the crystallinities of the as-deposited ZnO films are improved with the film thickness increase. Fig. 5.4(c) shows the ZnO films with different thicknesses annealed in forming gas at 430 ^{o}C for 8 h in the conventional furnace, the (002) peak position of annealed films shifts to the angle at about 34.5^{o}. The FWHM values of (002) diffraction peak of annealed films decreases from 0.31^{o} to 0.23^{o} as the film thickness increases from 250 to 1000 nm, which indicate the crystallinities of the ZnO films are not only enhanced with the increasing of film thickness but also improved by annealing treatment.

Figure 5.5 shows the morphologies of the as-deposited and annealed ZnO films are examined using an FE-SEM system. It is clearly observed that the as-deposited ZnO films have a uniform surface. Fig. 5.5(a)-(d) exhibit that the average grain size of the as-deposited films increases from 120 to 280 nm with the film thickness increases from 250 to 1000 nm. After annealing in reducing gas ambient for 8 h, as shown in Fig. 5.5(e)-(h), ZnO nanorods with uniform hexagonal heads at a diameter of 120 nm have been distributed on all annealed ZnO films. The average length of ZnO nanorods gradually increases from 600 to 800 nm as the films thickness increases from 250 to 1000 nm. Furthermore, the quantity of ZnO nanorods increases with the increase of film thickness. The most quantity of ZnO nanorods is prosperously formed from the film with the thickness of 1000 nm.

The growth mechanisms of the nanostructured ZnO thin film might be described as below. During the annealing temperature increases from room temperature to the melting point of Zn (420 ^{o}C) in furnace, the un-reacted zinc atoms existed on the as-deposited films will be evaporated and condensed as nuclear islands distributed on the surface of ZnO films. The formed nuclear islands are the criteria of quantity of ZnO nanostructures, which contribute to the re-growth of the ZnO nanostructures afterwards. Figure 5.6 shows the resistivity of as-deposited ZnO films with different thicknesses. The film resistivity decreases from 8.35 × 10^{3} to 8.28 × 10^{1} Ω cm when the film thickness increases from 250 to 1000 nm. The increase of film thickness results in decreasing the film resistivity due to the much more un-reacted zinc atoms remained in formed film with the only argon gas sputtering ambient during the deposition

process. Correspondingly, during annealing process, the more quantity of ZnO nanorods formed in the thicker film in which the more un-reacted zinc atoms remained, which correlates with the results of SEM measurement.

Figure 5.7(1-a) shows the transmittance spectra of the as-deposited ZnO films with different thicknesses. The transmittance of as-deposited films on the quartz glass gradually decreases from 87 to 78% in the visible region corresponding to the film thickness increases from 250 to 1000 nm. The absorption edge of the ZnO films shifts to higher wavelengths with the increase of the thickness. The shift of absorption edge is attributed to the changing of grain size and/or carrier concentration. It is observed that the all as-deposited films have a sharp absorption in the UV region. The energy gap (E_g) of as-deposited films with different thicknesses can be evaluated from the plots of $(\alpha h\upsilon)^2$ versus the photon energy ($h\upsilon$), as shown in Fig. 5.7(1-b). The evaluated band gaps of the as-deposited ZnO films are 3.245, 3.248, 3.254, and 3.257 eV corresponding to the thickness of 250, 500, 750, and 1000 nm, respectively, which indicates that the band gap energy of the ZnO films increases with increasing the film thickness. The changing of band gap can be attributed to the modulation of the interatomic spacing of semiconductors. Figure 5.7(2-a) and 4(2-b) show the transmittance spectra and the calculated band gap energies of the annealed ZnO films with different thicknesses, respectively. The transmittance of annealed films on the quartz glass further decreases from 85 to 63% in the visible region as the film thickness increases from 250 to 1000 nm. The blue-shift is also observed at absorption edge of the annealed ZnO films with the increasing of the thickness. However, the slope gradually becomes less acute near the absorption edges as the thickness increases. The evaluated band gaps of annealed ZnO films are 3.264, 3.264, 3.267, and 3.272 eV corresponding to the thickness of 250, 500, 750, 1000 nm, respectively, which indicates that the band gap energy of the ZnO films slightly increases after annealing.

PL spectra of the as-deposited ZnO films with different thicknesses are shown in Fig. 5.8(a). The PL spectra of the as-deposited films have exhibited two part peaks: a sharp peak of UV emission and a broad peak of deep level emissions (DLE) in visible region, respectively. It is well-known that the UV emission is related to the crystalline quality, which corresponds to the exciton emission from near conduction band to valence band. The intensity of UV emission at around 378 nm increases with the increase of the thickness, which indicates that the optical crystallinity enhanced with the increasing of film thickness. This result is in well agreement with XRD measurements. However, the DLEs in visible region are due to intrinsic defects. The defects in as-deposited film are unavoidable during the deposition process. For the annealed films with different thicknesses, as shown in Fig 5.8(b), the intensity of UV emission in the PL spectra of annealed ZnO films is considerably improved with the increase of the thickness. Meanwhile, the green emission with a peak centered at about 500 nm is obtained from all

annealed films. It is well accepted that the green emission is due to the oxygen vacancies (V_o) in the ZnO films. After annealing in reducing ambient, the reducing gas annealing effect contributes not only to increasing the oxygen vacancies but also to forming ZnO nanorods. The PL intensity of the green emission increases as the increase of film thickness. The strongest intensity of green emission is obtained from the film with the thickness of 1000 nm due to the formed much dense ZnO nanorods on which there are much more oxygen vacancies remained.

5.2.2.3 Summary

ZnO films were deposited onto quartz glass substrates with different film thicknesses. The as-deposited ZnO films had a hexagonal wurtzite structure and the crystallinity of as-deposited films was improved with increasing film thickness. ZnO nanorods from different thickness films were formed by annealing ZnO films in reducing ambient at a low temperature of 430 ^{o}C. The quantity of ZnO nanorods increased with the thickness increased, which was due to the quantity of un-react zinc atoms introduced by deposition process. PL spectra obtained from annealed films exhibited an intense deep level emission with a peak centered at about 500 nm. The strongest green luminescence was observed from the annealed film with the thickness of 1000 nm, which was attribute to the dense ZnO nanostructures which supplies much larger surface area where more oxygen vacancies existed.

5.3 Nanostructured ZnO thin films formed by multiple annealing processes

5.3.1 Well-arrayed nanostructured ZnO thin film formed by multiple annealing processes

5.3.1.1 Experiments

ZnO thin films (1 μm in thickness) were deposited on quartz glass by an RF (13.56 MHz) magnetron sputtering system using a sintered ZnO (5N) target. The substrate was heated and kept at 150 ºC before and during deposition. Ar with a flow rate of 30 sccm was introduced into the chamber as the working gas. The deposition pressure was kept at 7 Pa with an RF power of 180 W. Following deposition, the deposited films were annealed at 430 ºC in a conventional furnace in a series of steps: (I) forming gas (H_2 in N_2: 2%) for 3 h, (II) oxygen for 1 h, (III) forming gas for 5 h. For safety, N_2 gas was introduced into the chamber for 5 min between step (I) and (II), and step (II) and (III). The deposition and post-treatment parameters of ZnO thin films annealed by multiple annealing processes are shown in Table 5.3.

Table 5.3 Deposition and post-treatment parameters of ZnO thin films annealed by multiple annealing processes.

Target	ZnO (5N, 4 inch)
Substrates	Quartz glass
Temperature	150 ^{o}C
Deposition pressure	7 Pa
Ar gas flow rate	30 sccm
RF power	180 W (2.4 W/cm^2)
Processes	I) Forming gas (H_2 in N_2: 1.9%) for 3 h, II) Oxygen for 1 h, III) Forming gas (H_2 in N_2: 1.9%) for 5 h
Temperature	430 ^{o}C

5.3.1.2 Results and discussion

The morphologies of the as-deposited ZnO thin film and ZnO nanostructures were examined using an FE-SEM system, as shown in Fig. 5.9. It can be observed that the as-deposited ZnO thin film has a uniform and flat surface with an average grain size of about 300 nm. However, ZnO nanorods with uniform hexagonal heads have been vertically distributed on the ZnO films after annealing in the reducing ambient for 3 h. The evaluated diameter and height of nanorods are about 140 nm and 350 nm, respectively. After annealing in the oxygen ambient for 1 h, ZnO nanorods have grown slightly due to oxidation, without any change in the density of the nanostructures. The diameter and length of nanorods has increased to about 160 nm and 400 nm, respectively. Un-expectedly, higher density ZnO nanostructures of the reversed cones type with large hexagonal heads can be observed after annealing in the reducing ambient again for 5 h, as shown in the top view and cross-section of Fig. 5.9(d). The average diameter of the stems of formed ZnO nanostructures increases gradually from 160 nm at the bottom to 470 nm at the top. The average height of nanostructures is about 650 nm.

Figure 5.10(1) shows the XRD patterns of ZnO thin film and ZnO nanostructures obtained at each step of the multi-annealing processes. It is clear that the (002) diffraction peak is oriented highly perpendicular to the plane of the substrate for as-deposited ZnO film and nanostructures. Firstly, the (002) peak intensity of ZnO nanostructures is significantly increased after step I compared with as-deposited film, then substantially increases after step II and step III. Fig. 5.10(2) shows the position and the full width at half-maximum (FWHM) of the (002) diffraction

peaks on post-treatment process. The peak position of as-deposited film shifts from 34.35^{o} to a higher angle of 34.47^{o}, 34.48^{o} and 34.48^{o} after annealing step I, II and III, respectively. According to the (002) peak position of unstrained ZnO powder ($2\theta = 34.42^{o}$), the compressive stress is confirmed to be released after annealing processes. The FWHM values of (002) diffraction peak sharply decrease from 0.39^{o} of as-deposited film to 0.28^{o}, 0.24^{o} and 0.22^{o} after annealing step I, II and III, which indicates the crystallinity of the ZnO films is first significantly improved and then obviously enhanced with the post-treatment processes.

The growing mechanisms of formed well-arrayed ZnO nanostructures are described as below. When the temperature increases, nuclear islands are quickly formed by the un-reacted zinc atoms on the surface of as-deposited thin film. Meanwhile, a reduction reaction, according to the reducing equation, $H_2 + ZnO = Zn + H_2O$, occurs on the surface of ZnO thin film when H_2 is introduced to the furnace. With the temperature increased to over 420 ^{o}C (the melting point of the zinc atom), the reduced Zn atoms would evaporate and adhere to the formed ZnO nuclei, serving as self-catalyst to form ZnO nanostructures along the preferential orientation path. During annealing in sufficient oxygen atmosphere (step II), Zn atoms produced from reduction reaction in step I would be oxidized to form ZnO, which contributes to slight regrowth of ZnO nanostructures as well as the introduction of oxygen into the ZnO thin film. Consequently, the crystallinity of nanostructures on thin films is significantly improved. During annealing again in reducing gas (step III), the growth mechanism is similar to that in step I. However, oxygen annealing in step II might increase the amount of oxygen in the surface of thin film and nanostructures. Therefore, the ZnO nanostructures could be regrown quickly in prioritized c-axis direction. When the reducing annealing time is further increased, the reduction product, i. e: formed H_2O vapor, will be increased as well. This vapor would be absorbed on the top of the ZnO nanorods, and suppress the H_2 reducing effect on the top of ZnO nanorods. Consequently, the lateral growth of ZnO nanostructures will be enhanced. Finally, the ZnO nanostructures appeared as fluted reverse cones with hexagonal heads.

Figure 5.11 shows the PL spectra of as-deposited ZnO thin film and ZnO nanostructures. It is difficult to find visible range emission in as-deposited ZnO thin film. The intensity of UV peak increases at each post-treatment step, which indicates that optical crystallinity is significantly improved. A broad green PL peak is obtained from the ZnO nanostructures after step I, which means that the oxygen vacancies are introduced by the reducing atmosphere annealing. This corresponds with the well-accepted green emission principle in ZnO thin film. It is reasonable to assume that, due to the oxidation reaction, there is a remarkable yellow shift with degraded intensity of visible light emission after step II. This shift leads to a quantity of oxygen vacancies being partially neutralized in both the formed nanostructures and thin film during annealing in pure oxygen ambient. Furthermore, the much enhanced PL peak shifts back to 504 nm after

annealing step III. According to the morphology of ZnO nanostructures that have bigger size hexagonal heads and greater height, it is possible to assume that many more oxygen vacancies are produced by the lengthier annealing time and are present in the nanostructures with a larger surface area.

5.3.1.3 Summary

The effects of multi-annealing processes on forming ZnO nanostructures on the ZnO thin films were investigated. Well-arrayed ZnO nanostructures with the appearance of fluted reverse cones capped with hexagonal heads were obtained via a novel multi-annealing process. The crystallinity of ZnO nanostructures was also improved. ZnO nanorods with oxygen vacancies contribute to green luminance after treatment in reducing gas. Oxygen annealing between the two reducing gas annealing processes contributed to efficiently introduce the oxygen into the ZnO thin films, leading to ZnO nanostructures regrown quickly. An intense green emission centered at 504 nm was obtained, ascribable to the large amount of oxygen vacancies on the formed enlarged surface of ZnO nanostructures after multi-annealing processes at a low temperature of 430 ^{o}C.

5.3.2 Effects of multiple annealing processes with different annealing time on fabrication of nanostructured ZnO thin films

5.3.2.1 Experiments

ZnO thin films (1 μm in thickness) were deposited on quartz glass by an RF (13.56 MHz) magnetron sputtering system using a sintered ZnO (5N) target. The substrate was pre-heated and kept at 150 ºC before and during deposition. Ar with a flow rate of 30 sccm was introduced into the chamber as the working gas. The deposition pressure was kept at 7 Pa with an RF power of 180 W. Following the deposition, the ZnO films were annealed at 430 ºC in a conventional furnace with multi-steps: (I) forming gas (H_2 in N_2: 2%) for 5 h (II) oxygen for 1 h, (III) forming gas (H_2 in N_2: 2%) for 5 h. For safety, the N2 gas was introduced in the chamber for 10 min each time between every two processes. In order to obtain the optimized condition, the first process was also carried in 3 h and 8 h. The deposition and post-treatment parameters of ZnO thin films annealed by multiple annealing processes with different annealing time are shown in Table 5.4.

Table 5.4 Deposition and post-treatment parameters of ZnO thin films annealed by multiple annealing processes with different annealing time.

Target	ZnO (5N, 4 inch)
Substrates	Quartz glass
Temperature	150 ^{o}C
Deposition pressure	7 Pa
Ar gas flow rate	30 sccm
RF power	180 W (2.4 W/cm^2)
Processes	I) Forming gas (H_2 in N_2: 1.9%) for 3, 5, 8 h, II) Oxygen for 1 h, III) Forming gas (H_2 in N_2: 1.9%) for 5 h
Temperature	430 ^{o}C

5.3.2.2 Results and discussion

Figure 5.12 shows the XRD patterns of ZnO thin film and ZnO nanostructures obtained by each step of multiple post-treatment for the ZnO film for which annealed in reducing ambient for 5 h in step (I). It is obvious that the (002) diffraction peak is oriented highly perpendicular to the plane of the substrate for as-deposited ZnO film and nanostructures. The (002) peak intensity is gradually increased with the three annealing steps. Fig. 5.12(b) shows the position and the full width at half-maximum (FWHM) of the (002) diffraction peaks varied with the each post-treatment process. The peak position of as-deposited film shifted from 34.36° to higher angle of 34.48°, 34.50° and 34.51° after annealing step I, II and III, respectively. According to the (002) peak position of unstrained ZnO powder ($2\theta = 34.42°$), the compressive stress suffered as-deposited ZnO thin film releases the stress to tensile along the interfaces after annealing. The FWHM values of (002) diffraction peak sharply decreases from 0.32° of as-deposited film to 0.27° after annealing in step III, which indicated the crystallinities of the ZnO films were significantly improved with the post-treatment processes.

Based on the mechanism of ZnO nanostructures in our previously research [7,8], the beginning of ZnO nuclei formed in the first reducing annealing is much important for the regrowth of nanostructures, so that we investigated the difference reducing time effects on the properties of ZnO film. The only first step I of annealing was set respectively at 3, 5 and 8 h, following by the same annealing step II and III. The comparison results of XRD patterns were shown in Fig. 5.13. It was found that the crystallinities of annealed ZnO films were improved with the annealing time increase in the step I. Correspondingly, the annealed ZnO films after the

multi-step showed much better crystallinity comparing to that of step I, meanwhile, it was observed the intensity of XRD peak followed the same order of the step I. This result shows the multi-step is efficient method to improve the crystallinity of ZnO nanostructure.

Figure 5.14 shows the SEM images for the ZnO films annealed from the step I and multiple steps. It was found that the nanostructures were formed on the ZnO films after both step I and multi-step reducing annealing. It was clearly observed that the only small amount of ZnO nanostructures appeared after annealing for 3 h, however, the density of ZnO nanostructures was significantly increased after annealing for 5 h; slightly decrease after annealing for 8 h in the step I. It was also noticed that there was etching phenomenon occurred after annealing for 8 h, which was the reason why the quantity of nanostructures decreased. After the multi-step annealing, it was very interested that the ZnO nanostructures grown flourishingly on the ZnO film, it was found that the nanostructures obtained from 3 and 5 h exhibited the uniform hexagonal heads (about 400nm and 600 nm in diameter respectively) and height (about 800 nm and 1200 nm, respectively). The average diameter of the stems of the ZnO nanostructures increased from 90 nm at the bottom to 1200 nm at the top hexagonal heads from 5 h annealing. Thus, it is confirmed that the regrowth of ZnO nanostructures are much efficient than that from 3 h in step I. Because the over etching happened in the first step annealing, the etching was also observed by the cross-section plot inserted in the SEM image for 8 h, the shape of nanostructures changed to nanorods. As our known, the regrowth of ZnO nanostructures relies on the several parameters in which the oxygen is the most important for re-crystallize of ZnO nanostructures. The oxygen annealing step II between the step I and III could introduce much oxygen into the surface of ZnO film, which help on the quickly reaction during reducing annealing in step III, resulting in the quickly regrowth of ZnO nanostructures.

Figure 5.15 shows the PL spectra of ZnO thin films annealed followed the each steps. A broad weak green PL peak was obtained from the ZnO nanostructures after step I, which meant that the oxygen vacancies were introduced by the reducing atmosphere annealing. It is reasonable for observing that, due to the oxidation reaction, there was a remarkable yellow shift with degraded intensity of visible light emission after step II. This shift led to a quantity of oxygen vacancies being partially neutralized in both the formed nanostructures and thin film during annealing in pure oxygen ambient. Furthermore, the much enhanced PL peak shifted back to 504 nm after annealing step III. According to the morphologies of ZnO nanostructures after the step III, the ZnO nanostructures showed the bigger hexagonal heads and greater height, it was possible to assume that much oxygen introduced by step II contributed to the regrowth of ZnO nanostructures.

The green emission of ZnO thin films arises from oxygen vacancy related defect centers in the films [9,10]. Comparing the ZnO nanostructures formed in the different annealing steps, it

was obviously that the PL properties strongly depend on the nanostructures formed by each steps. After annealing in the reducing gas ambient step I, the oxygen vacancies were slightly introduced by the reducing reaction. During annealing in the oxygen ambient, much more oxygen was introduced into the film, consequently, the reducing reaction was enhanced during the third step annealing process, result at the ZnO nanostructures further re-growth. Therefore, it can assume that the much more oxygen vacancies might be produced and existed on the ZnO nanostructures which have much larger appearance area, result in the enhancement of PL peak in the visible range.

In order to investigate the optimum annealing condition, we also compared the different annealing time in the first process. The PL spectra obtained from annealed ZnO films in step I and multi-step were shown in Fig. 5.16. It was obviously that the first reducing annealing step contributed to the green emission which attribute to the oxygen vacancies exist on the small amount formed ZnO nanostructures. The highest green emission peak centered at 505 nm was obtained from the ZnO nanostructures annealed for 5 h in step I. After annealing for multi-step, it was found that the intensity of PL peaks were significantly enhanced comparing to the first step annealing. It was confirmed that the green emission peak after the multi-steps followed the same order of that in Step I, still, the highest green emission peak was obtained from 5 h annealing.

5.3.2.3 Summary

Based on the multiple annealing processes on forming well-arrayed ZnO nanostructures, we investigated the effects of the time dependence in first step of multiple annealing processes on fabrication of nanostructured ZnO thin films. It is found that the optimized condition for forming nanostructured ZnO films in reducing ambient first for 5 h. The ZnO nanostructures with uniform hexagonal head with diameter of 600 nm and average height of 1200nm were formed after multi-step annealing. The intense PL emission peak centered at 505 nm was obtained from the well-arrayed ZnO nanostructures, The PL intensity of nanostructured ZnO thin film formed from multi-step annealing of first annealing for 5 h was much higher than those of annealing time.

5.4 Conclusions

In this chapter, ZnO thin films with different deposition parameters were prepared by using RF magnetron sputtering. Following the preparation, nanostructured ZnO thin films were formed by different post-treatment processes. The effects of different post-treatment processes

on the structural and optical properties on nanostructured ZnO thin films were investigated. The conclusions of each part in this chapter will be generally expressed one by one.

1) As we described in our previous research, nanostructured ZnO thin films with much large appearance area were fabricated using reducing annealing. In this study, nanostructured ZnO thin films were formed by optimizing the post-treatment time in reducing gas. The highest green emission peak centered at 497 nm is obtained from the ZnO nanostructures annealed for the optimum annealing time of 5 h. Therefore, it can assume that the much more oxygen vacancies might be produced and existed on the ZnO nanostructures. XRD measurements indicated that the ZnO thin film annealed for optimizing annealing time of 5 h also exhibited the better crystallinity.

2) ZnO nanorods from different thickness films were formed by annealing ZnO films in reducing ambient at a low temperature of 430 ^{o}C. The quantity of ZnO nanorods increased with the thickness increased, which was due to the quantity of un-react zinc atoms introduced by deposition process. PL spectra obtained from annealed films exhibited an intense deep level emission with a peak centered at about 500 nm. The strongest green luminescence was observed from the annealed film with the thickness of 1000 nm, which was attribute to the dense ZnO nanostructures which supplies much larger surface area where more oxygen vacancies existed. Therefore, this study is an efficient method to control the density of ZnO nanostructures by simply adjusting film thickness.

3) In order to further control and produce well-arrayed ZnO nanostructures, we developed a novel low-temperature multi-annealing process, which combines a reducing annealing process and oxygen annealing process. The effects of multi-annealing processes on forming ZnO nanostructures on the ZnO thin films were investigated. Well-arrayed ZnO nanostructures with the appearance of fluted reverse cones capped with hexagonal heads were obtained via a novel multi-annealing process. The crystallinity of ZnO nanostructures was also improved. ZnO nanorods with oxygen vacancies contribute to green luminance after treatment in reducing gas. Oxygen annealing between the two reducing gas annealing processes contributed to efficiently introduce the oxygen into the ZnO thin films, leading to ZnO nanostructures regrown quickly. Therefore, the multi-annealing process is an efficient method to form well-arrayed ZnO nanostructures.

4) As we exhibited above, the well-arrayed ZnO nanostructures could be fabricated controllably on the ZnO film after multiple treatments at a low temperature of 430 °C. In order to optimize the processes for forming nanostructured ZnO thin film with intense visible luminescence, the annealing time of first step in multi-annealing processes was modulated. It was confirmed that the first step in the reducing ambient was most important process for nanostructured ZnO thin film formation. The oxygen annealing between the two reducing

annealing steps contributed to introduce the much oxygen into the ZnO film to help the regrowth of the ZnO nanostructures afterwards. The crystallinity of ZnO nanostructures was significantly improved after multi-step annealing. The optimized condition for form the nanostructure was found for the annealing in reducing ambient first for 5 h. The ZnO nanostructures with uniform hexagonal head with diameter of 600 nm and average height of 1200 nm were formed after multi-step annealing. The intense PL emission peak centered at 505 nm was obtained from the well-arrayed ZnO nanostructures. PL intensity of nanostructured ZnO thin film formed from multi-step annealing was much stronger than that obtained from only reducing annealing process. Therefore, the multi-step post-treatment process is efficient method to not only form ZnO nanostructures but also adjust oxygen vacancies in the films.

It is expected that the nanostructured ZnO thin films formed by above methods might be potentially applied in optoelectronic devices in the future.

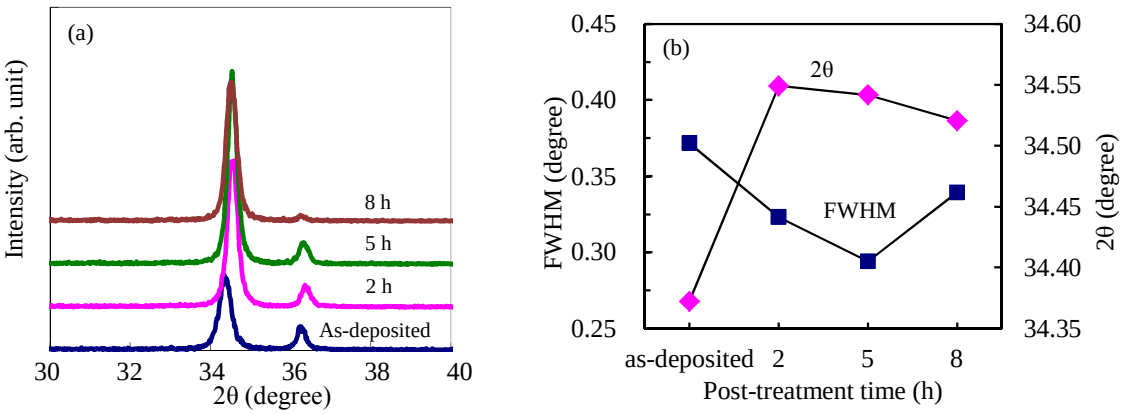

Fig. 5.1 (a) XRD patterns and (b) FWHM and c-axis crystalline size of as-deposited ZnO film and ZnO nanostructrures annealed with different annealing time.

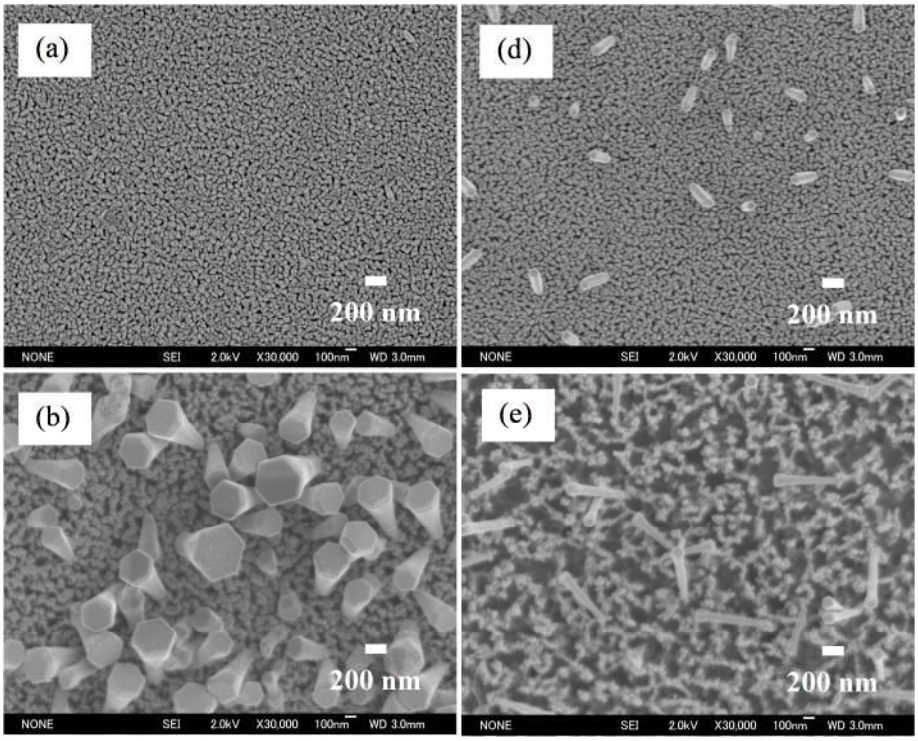

Fig. 5.2 SEM images of (a) as-deposited ZnO film and ZnO nanostructrures annealed with different annealing time (b) 2 h (c) 5 h (d) 8 h.

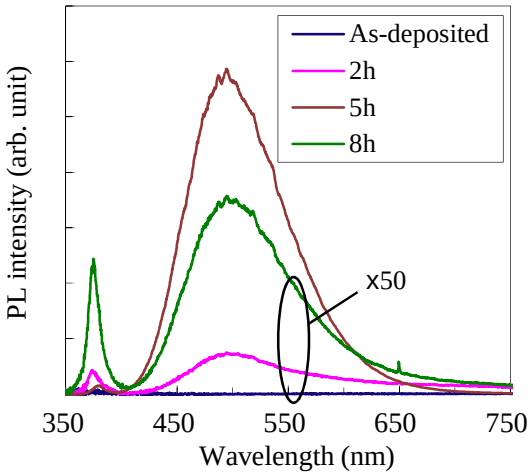

Fig. 5.3 PL spectra of as-deposited ZnO film and ZnO nanostructrures annealed with different annealing time.

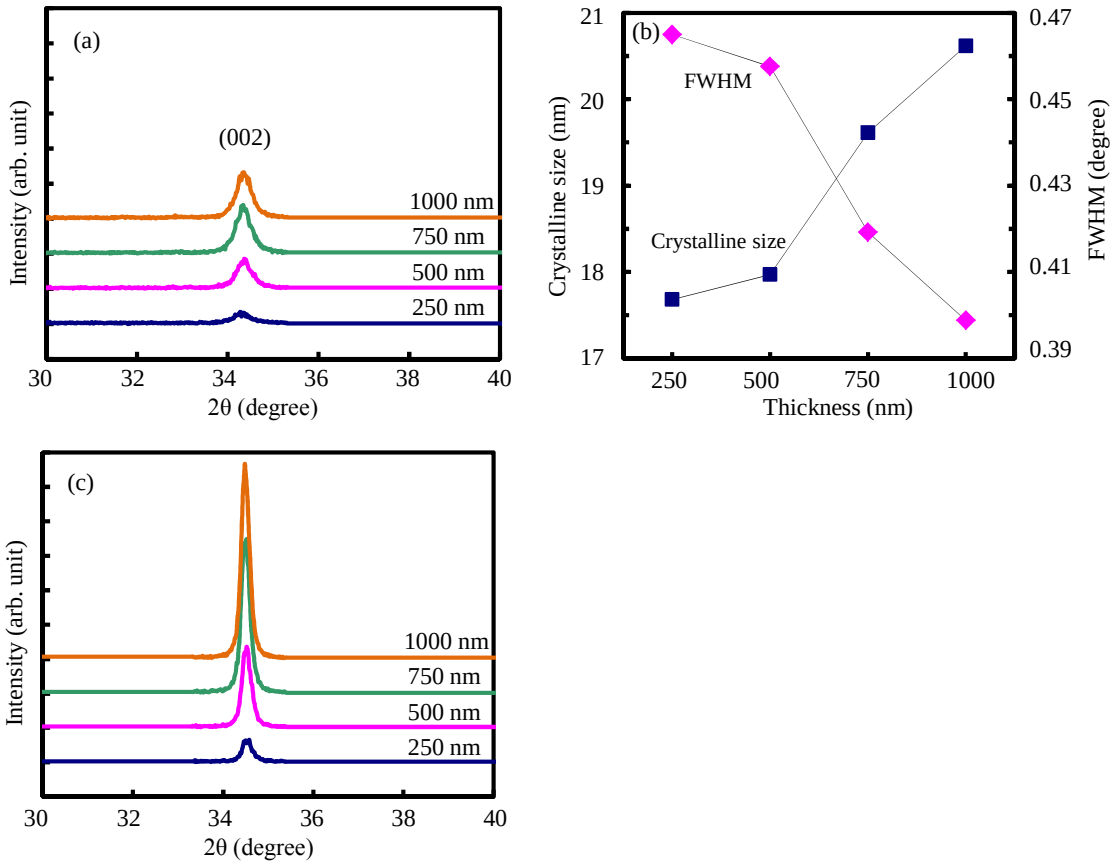

Fig. 5.4 XRD patterns of (a) as-deposited ZnO films with different thicknesses deposited on quartz substrates. (b) the c-axis crystalline size and FWHM in the (002) direction for the films with different thicknesses. (c) ZnO nanorods obtained from ZnO films after annealing in forming gas.

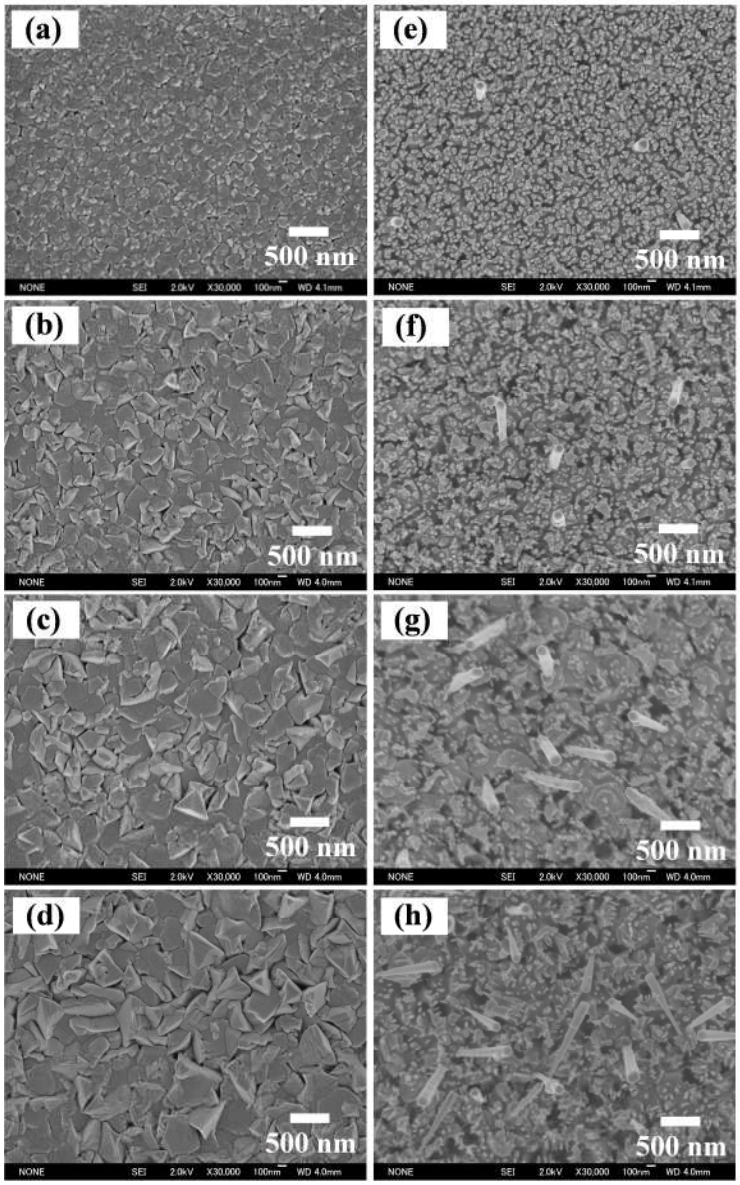

Fig. 5.5 SEM images of as-deposited ZnO films with the thickness of (a) 250 nm, (b) 500 nm, (c) 750 nm, (d) 1000 nm and annealed films with the thickness of (e) 250 nm, (f) 500 nm, (g) 750 nm, and (h) 1000 nm.

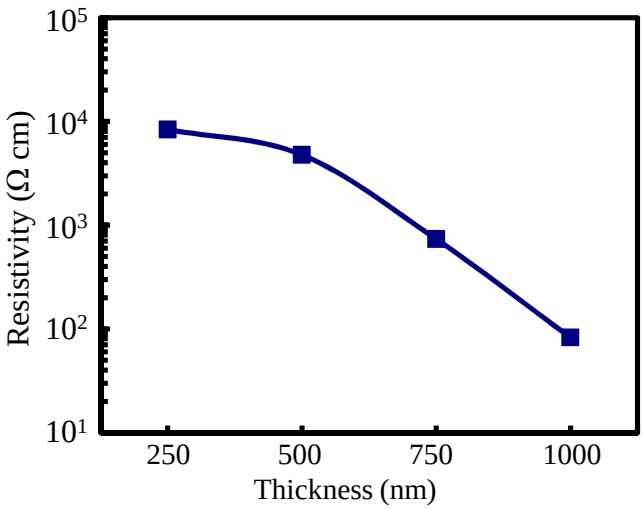

Fig. 5.6 Resistivity of as-deposited ZnO films with different thicknesses.

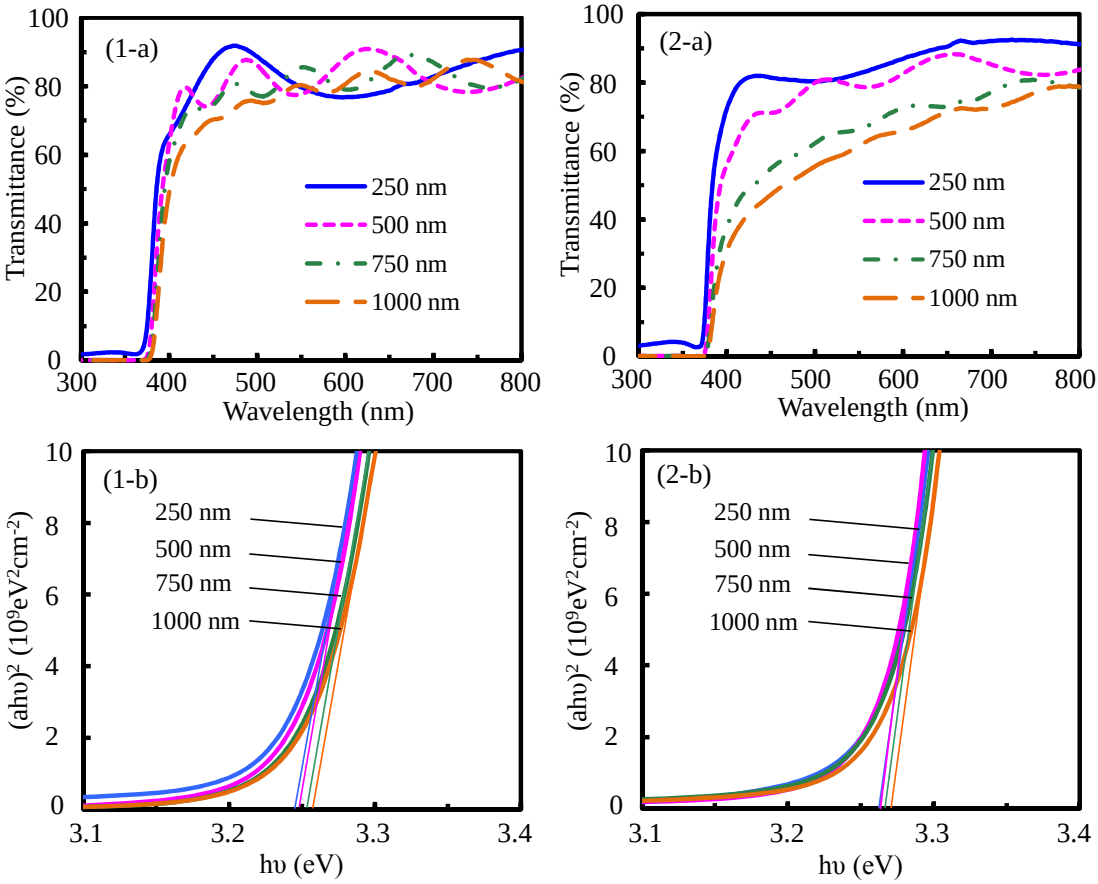

Fig. 5.7 Transmittance spectra of (1-a) as-deposited and (2-a) annealed ZnO films with different thicknesses. The variation of $(\alpha h\upsilon)^2$ of (1-b) as-deposited and (2-b) annealed ZnO films as a function of the photon energy ($h\upsilon$), respectively.

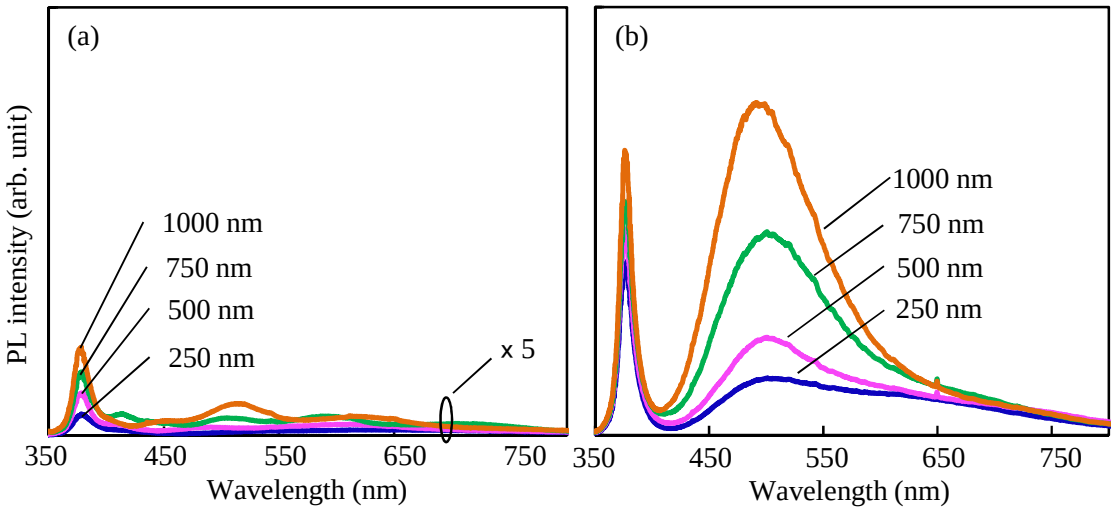

Fig. 5.8 PL spectra of (a) as-deposited and (b) annealed ZnO films with different thicknesses.

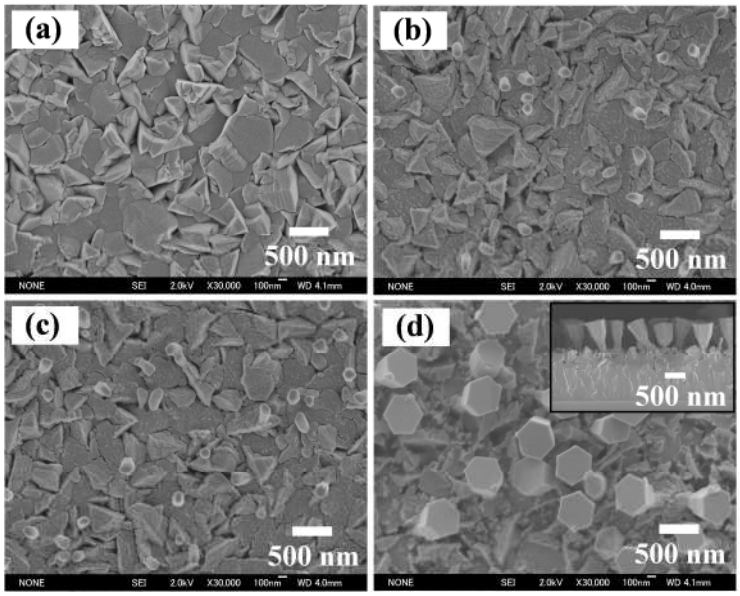

Fig. 5.9 SEM images of ZnO films (a) as-deposited and nanostructures obtained from annealed in (b) step I, (c) step I + II, and (d) step I + II + III. The inset SEM image is the cross section of ZnO nanostructures after the multi-annealing processes.

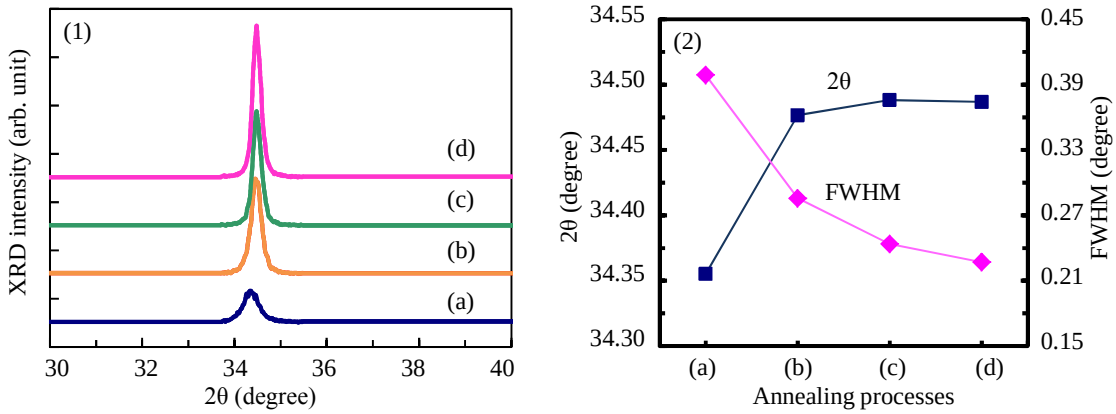

Fig. 5.10 (1) XRD patterns, (2) variation of peak position and the FWHM values obtained from ZnO films (a) as-deposited and annealed in (b) step I, (c) step I + II, and (d) step I + II + III.

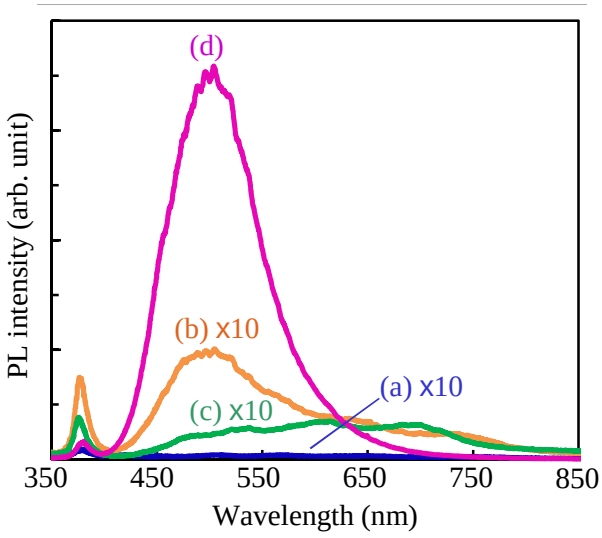

Fig. 5.11 PL spectra of ZnO films (a) as-deposited and annealed in (b) step I, (c) step I + II, and (d) step I + II + III, measured with the excitation power of 1 mW at room temperature.

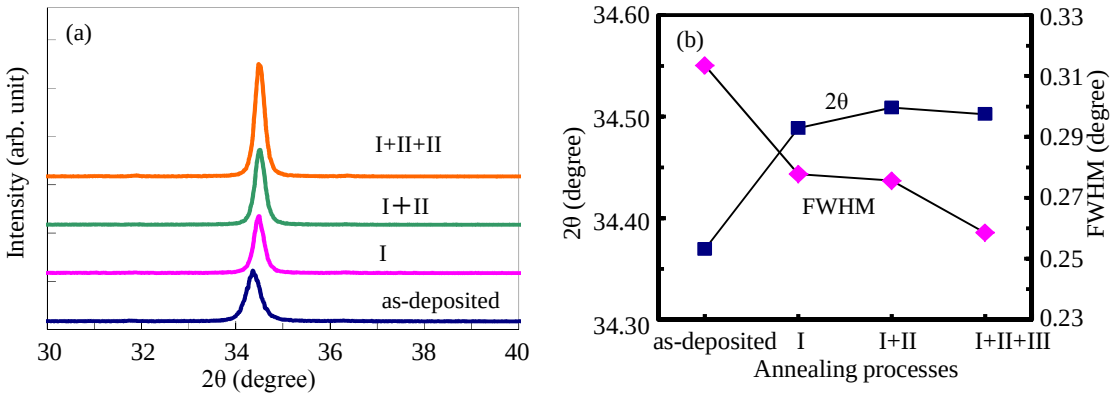

Fig. 5.12 (a) XRD patterns of ZnO films (a) as-deposited and annealed in (b) step I, (c) step I + II, and (d) step I + II + III. (b) Comparison of peak position and the FWHM values of XRD patterns varied with ZnO films (a) as-deposited and annealed in (b) step I, (c) step I + II, and (d) step I + II + III.

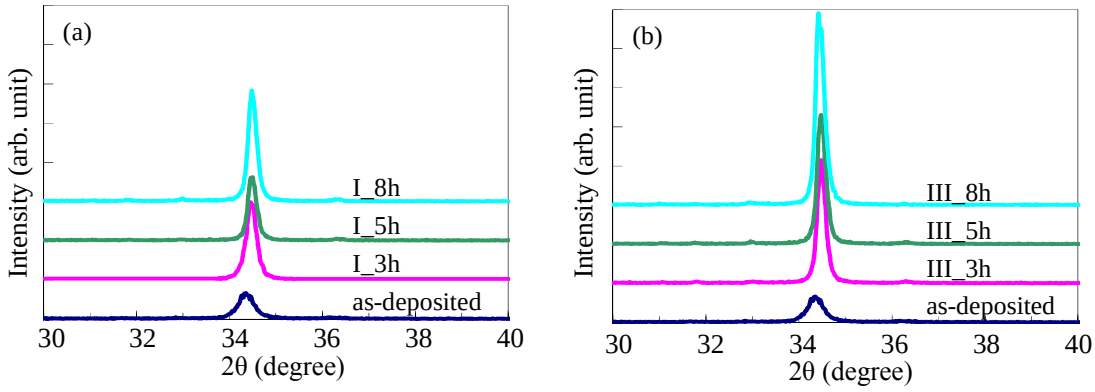

Fig. 5.13 XRD patterns of ZnO films for (a) as-deposited and annealed in different time in the step I (b) annealed after three steps.

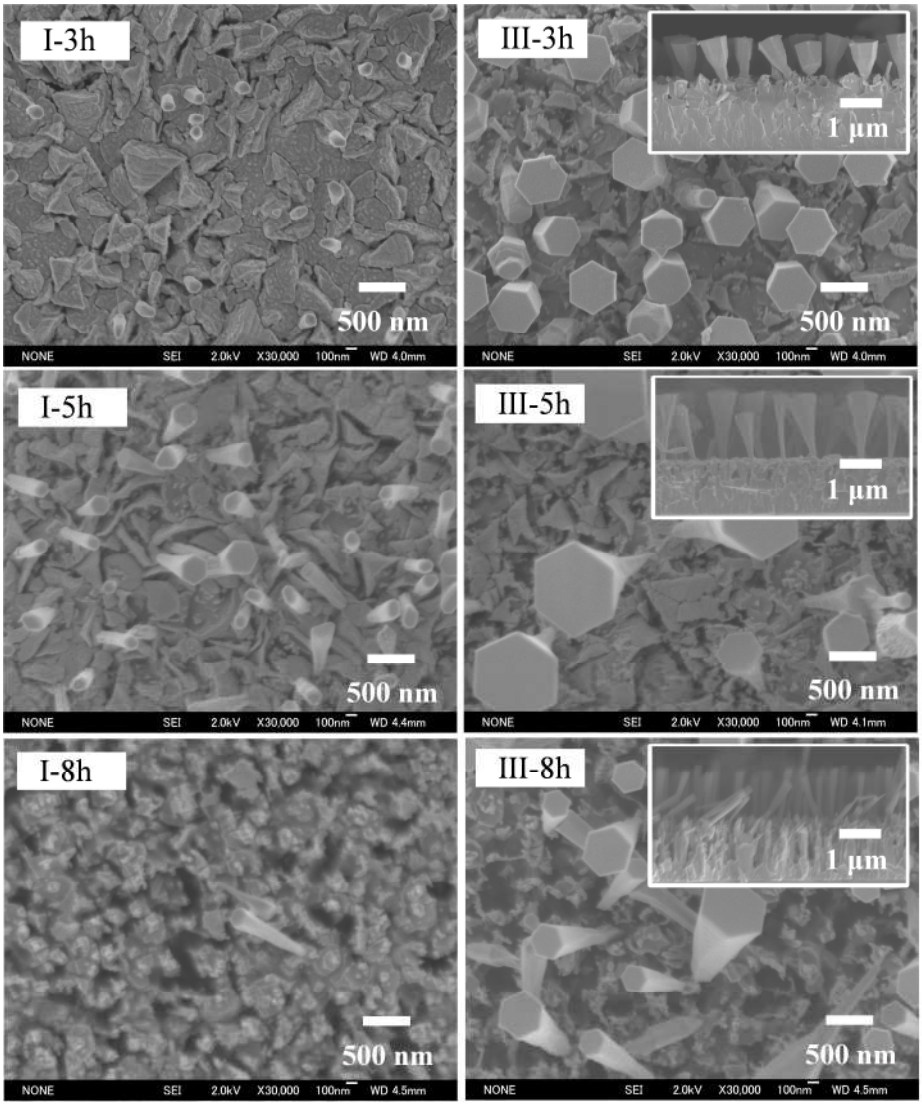

Fig. 5.14 SEM images of ZnO nanostructures obtained from step I with different annealing time and annealed in multi-steps, the only difference is the first step with different time. The inset SEM images are the cross section of ZnO nanostructures after the multi-annealing processes.

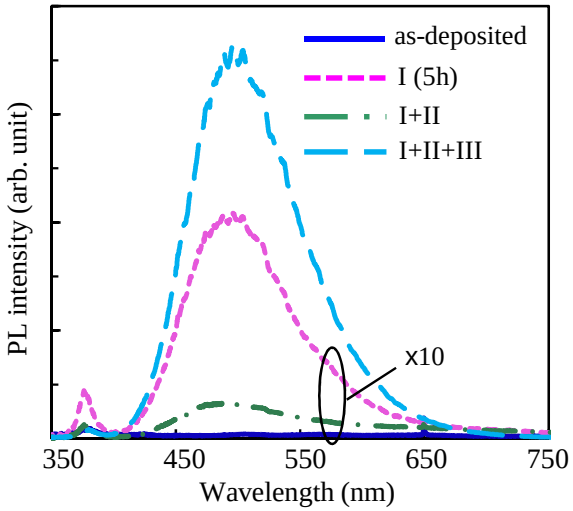

Fig. 5.15 PL spectra of as-deposited ZnO film and annealed in step I, step I + II, and step I + II + III with the first step set at 5 h.

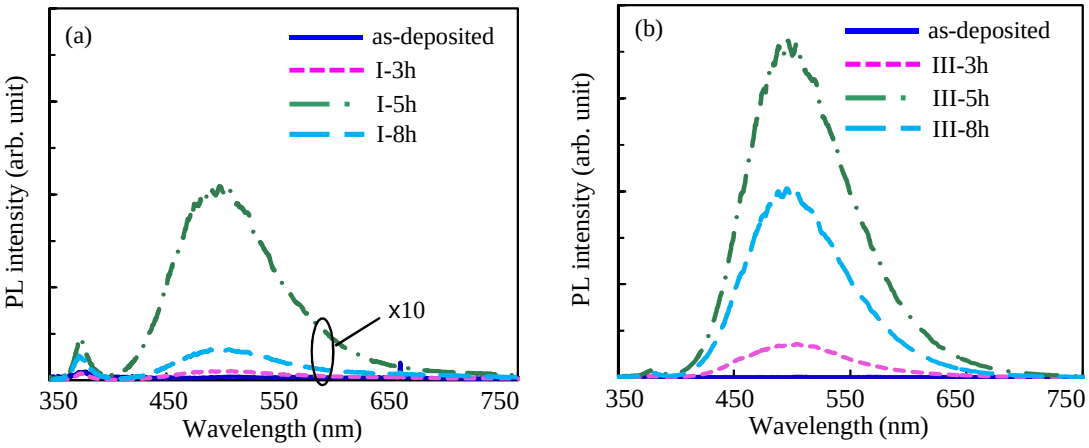

Fig. 5.16 PL spectra of ZnO nanostructures obtained from step I with different annealing time and (b) annealed in multi-steps, the only difference is the first step set with different time.

5.5 References

[1] Z. Zhang, S.J. Wang, T. Yu, and T. Wu, J. Phys. Chem. C, 111 (2007) 17500.

[2] C. Li, T. Kawaharamura, T. Matsuda, H. Furuta, T. Hiramatsu, M. Furuta, and T. Hirao, Appl. Phys. Express, 2 (2009) 091601-1.

[3] C. Li, T. Matsuda, T. Kawaharamura, H. Furuta, M. Furuta, T. Hiramatsu, T. Hirao, Y. Nakanishi, and K. Ichinomiya, J. Vac. Sci. Technol. B, 28 (2010) C2B51.

[4] P.X. Gao and Z.L. Wang, J. Phys. Chem. B, 108 (2004) 7534.

[5] B.L. Zhu, X.H. Sun, S.S. Guo, X.Z. Zhao, J. W, R. W, and J. L, Jpn. J. Appl. Phys., 45 (2006) 7860.

[6] S.T. Tan, B.J. Chen, X.W. Sun, W.J. Fan, H.S. Kwok, X.H. Zhang, and S.J. Chua, J. Appl. Phys., 98 (2005) 013505-1.

[7] T. Kawaharamura, H. Orita, T. Shirahata, A. Yoshida, S. Fujita, and T. Hirao, Phys. Status. Solidi C, 9 (2012) 190.

[8] D. Wang, Z. Li, T. Kawaharamura, M. Furuta, and T. Narusawa, Phys. Status. Solidi C, 9 (2012) 194.

[9] X.L. Wu, G.G. Siu, C.L. Fu, and H.C. Ong, Appl. Phys. Lett., 78 (2001) 2285.

[10] H.S. Hsu, J.C. Huang, Y.H. Huang, Y.F. Liao, M.Z. Lin, C.H. Lee, J.F. Lee, S.F. Chen, L.Y. Lai, and C.P. Liu, Appl. Phys. Lett., 88 (2006) 242507.

Chapter 6

Applications

6.1 Introduction

Currently ZnO based optoelectronic devices have advanced considerably due to low cost and fabrication techniques. Based on the investigation of ZnO-related materials thin films and nanostructured ZnO thin films discussed in above chapters, I tried to combine them into thin film transistors (TFTs) and vacuum fluorescent display (VFD), respectively.

1) Transparent electronics are an emerging technology for the next generation of optoelectronic devices. Oxide semiconductors are one of most interesting materials for a variety of applications. Recently non-doped ZnO has been proposed as active channel in thin film transistors [1-5]. One of the important advantages is high electron mobility, which cater to the requirements of higher drive currents and faster device operating speeds for thin film transistors. So far, ZnO channel layers have been deposited using substrate heating or annealed in order to increase the crystallinity of ZnO layer and film's mobility. Besides above mentioned advantage, ZnO is a wide band gap material of 3.3 eV at room temperature and transparent in the visible region of the spectra, which is less sensitive under light. In this chapter, ZnO thin film was deposited as channel layer of TFTs by RF sputtering. The characterizations of TFTs were also evaluated.

2) The development of new and high efficient phosphor has been an important technology for the display industry. In order to overcome the remained problems of powder phosphor and lower the fabrication cost, we developed a novel technique for fabricating ZnO thin film phosphor on the glass substrate directly at the low temperature. This fabricated ZnO thin film phosphor has the promising features including higher coherency, uniformity, flatness regarding to the disadvantage of the power phosphor. Particularly, the ZnO thin film phosphor, showing high luminance of blue-green, was easily and precisely patterned on large area by wet etching method. This method will be an exciting prospect to consider the application for VFD.

6.2 ZnO thin film for TFTs application

6.2.1 History of TFTs

As early as in 1962, Weimer demonstrated the first functional working TFT by using polycrystalline cadmium sulfide as channel layer [6]. In the middle of 1960's, a variety of TFT semiconductor materials, such as CdSe, Te, InSb and Ge were investigated. In the 1970s, the crystalline silicon was dramatically developed due to the low cost for miniaturization. In 1979, LeComber, Spear and Ghaith described a TFT using a-Si:H as the active semiconductor material. Since the middle of 1980s the silicon-based TFTs become the most important devices for active matrix liquid crystal displays (AMLCDs) and have successful dominated the large area LCD product market [7]. In 1990 the organic semiconductor active layer material was firstly utilized for TFTs [8]. Recently ZnO, a new generation of oxide semiconductors, has been studied and applied as active material to TFTs.

ZnO is a wide band gap (3.3 eV at room temperature) transparent oxide semiconductor. In 2006, the researcher first demonstrated AMLCDs addressed by ZnO TFTs. The mobility of ZnO based TFTs has been demonstrated to be over one order of magnitude higher than that of a-Si:H TFTs, which is a particular advantage for higher drive currents and faster device operating speeds. The one of the advantages is that ZnO with a wide band gap does not to degrade on exposure to visible light. In recent years, there has been significant interest in the reliability of transparent flexible TFTs under low temperature fabrication.

6.2.2 Experiments

Figure 6.1 shows a schematic cross–sectional view of the bottom-gate ZnO TFT. A SiO_x/SiN_x (50/100nm) stacked gate insulator was deposited on a chromium (Cr) gate electrode at 350 °C by conventional plasma-enhanced chemical vapor deposition (PECVD). Following that, a ZnO film with the thickness of 40 nm for an active channel was deposited at 150°C with O_2 and Ar as working gases by RF magnetron sputtering. The deposition pressure and O_2/Ar gas flow ratio during ZnO deposition were 1.0 Pa and 30/10 sccm, respectively. The RF power density applied to the ZnO target was set at 2.3W/cm^2. After definition of an active channel, a 200 nm thick SiN_x film as the interlayer was deposited by PECVD. The contact holes for the source and drain electrodes were opened, and source and drain electrodes were formed by indium tin oxide (ITO) deposited using DC magnetron sputtering technique. A 200 nm thick SiN_x passivation film was deposited by PECVD. During the fabrication processes, source, drain, gate contacts and a gate insulator were defined by standard photolithography and lift-off techniques. Before electrical measurements, the ZnO TFTs were annealed at 375 ^oC for 3 h in N_2 ambient.

6.2.3 Characteristics of bottom-gate ZnO TFT

Figure 6.2 shows the typical transfer characteristic of ZnO TFTs. The channel width (W) and length (L) of the ZnO TFTs were 50 and 20 μm, respectively. Transfer characteristics were measured at a drain voltage of 0.1, 10.1, and 20.1 V with a double-sweep gate voltage (V_{gs}) mode. The hysteresis is defined by the difference between the V_{gs} where a drain current of 1 nA flows (V_{gs} at an I_{ds} of 1 nA) obtained from V_{gs} sweeps of off-to-on and on-to-off. The hysteresis is defined by the difference between the V_{gs} where a drain current of 1 nA flows (V_{gs} at an I_{ds} of 1 nA) obtained from V_{gs} sweeps of off-to-on and on-to-off. The hysteresis of ZnO TFT is 0.68 V. The gate voltage swing, S, defined as the voltage required to increase the drain current by a factor of 10, is given by [9]

$$S = \frac{dV_G}{d(\log I_D)} \tag{6.1}$$

the S is 1.67 V/decade. The S is given by the maximum slope in the transfer curve. The transfer characteristic shows that a low off-current of the order of 10^{-13} A, and an on-to-off current ratio of 10^8 are obtained.

The saturation mobility (μ_{sat}) is obtained from the I_{DS}-V_{DS} curves in the saturation region using the equation

$$I_{ds} = \frac{1}{2}\mu_{sat} c_i \frac{W}{L}\left(V_{gs} - V_{th}\right)^2 \tag{6.2}$$

where C_i, V_{th}, W and L denote the gate capacitance, threshold gate voltage, channel width and length, respectively. The estimated μ_{sat} value is 1.98 cm^2/Vs. Similarly, the field-effect mobility (μ_{lin}) estimated from the linear region in the I_{DS}-V_{DS} curve by the equation

$$I_{ds} = c_i \mu_{lin} \frac{W}{L}(V_{gs} - V_{th})V_{ds} \tag{6.3}$$

the field-effect mobility is about 2.62 cm^2/Vs at V_{ds} = 0.1 V.

6.2.4 Summary

The present study demonstrates that the bottom-gate TFT was fabricated based on the ZnO semiconductor. ZnO TFT displayed good performance, such as saturation mobility of 1.98 cm^2/Vs, field-effect mobility of 2.62 cm^2/Vs, a low leak current of 10^{-13} A, and on-to-off current ratio of 10^8. The results indicate that the combination of transparency, high channel mobility and low temperature processing makes the ZnO TFT a promising low cost optoelectronic device.

6.3 Nanostructured ZnO thin film for VFD application

6.3.1 Overview of VFD

A vacuum fluorescent display (VFD) is a display device used commonly on electronics applications such as video cassette recorders, car radios, automobiles, and microwave ovens [10]. Since invented in Japan in 1967, the displays became more and more common on calculators and other consumer electronics devices [11]. Actually, the working principle of VFD tubes is in the same way as cathode-ray tubes (CRTs). Electrons emitted from a cathode are accelerated towards an anode with controllable bombardment, which excite the phosphor on the anode, contributing to light emitting. The different between VFDs and CRTs is that the latter use much higher accelerating voltage raging from kilovolts to tens of kilovolts. However, VFDs are commonly driven by a low voltage of from about 10 to 100 V.

Figure 6.3 shows the basic schematic sketch of VFD. It consists of cathode (filaments), anodes (phosphor) and grids encased in a glass envelope under a high vacuum condition [12]. The cathode is made up of fine tungsten wires, which emit electrons when heated by an electric current. These electrons are controlled and diffused by the grids, which are made up of thin metal. If electrons impinge on the phosphor-coated plates, they fluoresce, emitting light.

The VFD characteristics include the cathode characteristics, the on characteristics, the cut-off characteristics, and the luminescence characteristics. In the vacuum tubes, the cathodes of VFDs are designed to operate in the space-charge limited region. When the display is excited, the voltages on the grid and on the anodes are about the same. The luminance of L (cd m^{-2}) in the on state is represented as follows:

$$L \cong 3.2E_p \cdot J_p \cdot D_u \cdot \eta \qquad (6.1)$$

where E_p is the anode voltage (V), J_p is the anode current density (mA cm^{-2}), D_u is the duty cycle, and η is the luminous efficiency of the phosphor (lm W^{-1}).

6.3.2 Experiments

ZnO thin film with the thickness of 1 μm was deposited onto quartz glass substrate (diameter of 100 mm) by RF magnetron sputtering system. The substrate on an anode was heated and kept at 150 ºC before and during deposition and the chamber was evacuated to 7 × 10^{-5} Pa with a turbo molecular pump. Argon as the only working gas was introduced into the chamber at a flow rate of 30 W and was kept at 7 Pa during all the depositions. During the sputtering process, an RF power was set consistently at 180 W.

Following deposition, the sample was washed by pure water. After cleaning, the photoresist was coated on the ZnO thin film at 105 ^{o}C using spin coating method. The next process was to make pattern on the sample by photolithography machine (PLA521F, Canon Inc.). And then the pattern was formed after developing in developing solution, baking at 120 ^{o}C. The sample was

etched in HCl (0.30 mol/L) for 90 s. Finally, the patterned ZnO thin film was cleaned again.

In order to investigate the effects of post-treatment on the properties of the patterned ZnO thin film, the deposited film was annealed in a reducing gas ambient (H_2 in N_2: 1.9%) with a conventional furnace system. The annealing temperature was increased from room temperature to 450 ^{o}C with a rising rate of 10 ^{o}C/min at a stable annealing pressure of 50 kPa, and then cooled down to room temperature in the vacuum chamber. The schematic of the processes for patterned nanostructured ZnO thin film is exhibited in Fig. 6.4.

6.3.3 Results and discussion

As mentioned in Chapter 5, it is confirmed that nanorod-like nanostructured ZnO thin film is formed after treatment in reducing gas. Figure 6.5 presents a comparison of the XRD patterns of the as-deposited and nanostructured ZnO films. Both films exhibited a preferential orientation along the c-axis direction. The peak position of as-deposited ZnO film shifted slightly from 34.35^{o} to 34.45^{o} after annealing. The intensity of (002) peak also enhanced with narrowed full-width at half maximum. This result indicates that the crystallinity of nanostructured ZnO film was improved compared with that of as-deposited film.

Figure 6.6 shows the PL spectra obtained from as-deposited and nanostructured ZnO films. The PL spectrum of nanostructured ZnO thin film exhibits a sharp peak of UV emission at around 378 nm and a broad peak of green emission centered at around 500 nm, respectively. The intensity of annealed ZnO film had a significantly improved. The green luminescence also can be observed under excited by a handy UV lamp (SLUV-6, AS ONE Corp.) with the wavelength of 365 nm and excitation power of 6 W, as shown in Fig. 6.7.

6.3.4 Summary

A technique for fabricating ZnO thin film phosphor on the quartz glass substrate was carried out directly at the low temperature. The ZnO thin film phosphor, showing high luminance of blue-green, was easily and precisely patterned on large area (diameter of 100 mm) by wet etching method. The result indicates that nanostructured ZnO thin film might be taken as thin film phosphor for the potential application of VFD with low excitation voltage. The future aim is to optimize nanostructured ZnO thin film with large surface exhibiting high luminescence. We believe the experiences from this trial pave the way for further research.

6.4 Conclusions

Two kinds of potential applications were investigated based on the ZnO semiconductor. ZnO thin film and nanostructured ZnO thin film were applied into TFT and potentially treated for VFD, respectively. The characterization of as-deposited and annealed ZnO thin film were evaluated.

1) Bottom-gate TFT was fabricated based on the ZnO thin film as the channel layer, which was carried out with relatively simple processing technology. The results indicated that ZnO TFT displayed good performance, such as field-effect mobility of 2.62 cm^2/Vs, a low leak current of 10^{-13} A, and on-to-off current ratio of 10^8. There is no denying that combination of transparency, high channel mobility and low temperature processing makes the ZnO TFT a promising low cost optoelectronic device.

2) In order to overcome the remained problems of powder phosphor and lower the fabrication cost, we developed a novel technique for fabricating ZnO thin film phosphor on the glass substrate directly at the low temperature of 450 ^oC. After the preparation of ZnO thin film, the patterned thin film was easily and precisely formed on large area by wet etching method. This fabricated ZnO thin film phosphor by annealing in reducing gas has the promising features including higher coherency, uniformity, and flatness. The results mean that this method will be an important technology to develop the new and high efficient phosphor for VFD application.

It is hoped that the methods and results presented in this thesis can help the field move, even a small step, towards ZnO-related materials device fabrication and industrial applications.

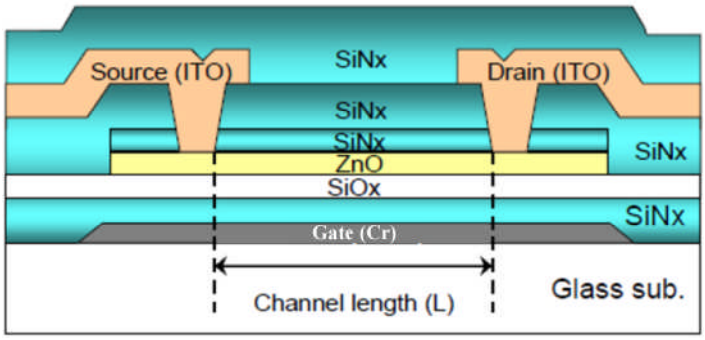

Fig. 6.1 schematic cross-sectional view of the bottom-gate ZnO TFT.

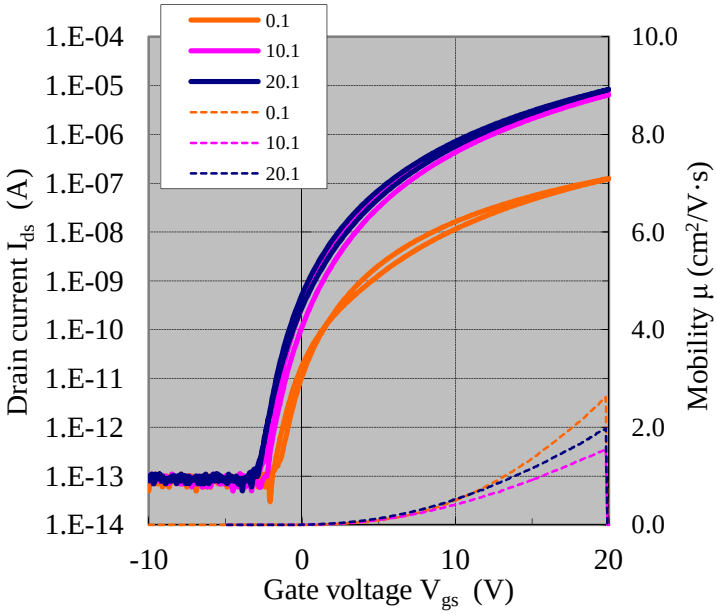

Fig. 6.2 Transfer characteristics of the bottom-gate ZnO TFT.

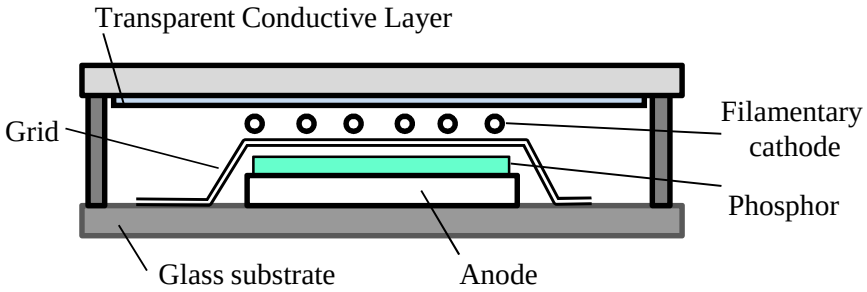

Fig. 6.3 The basic schematic sketch of VFD.

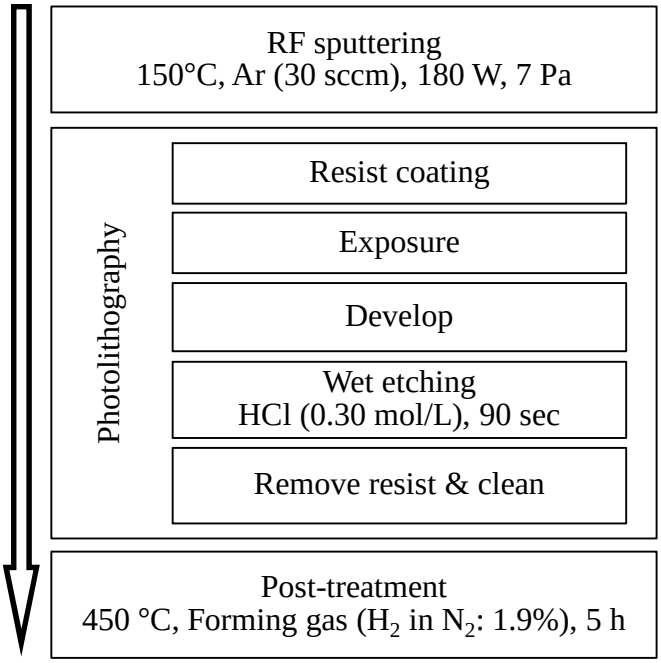

Fig. 6.4 The schematic of the processes for patterned nanostructured ZnO thin film..

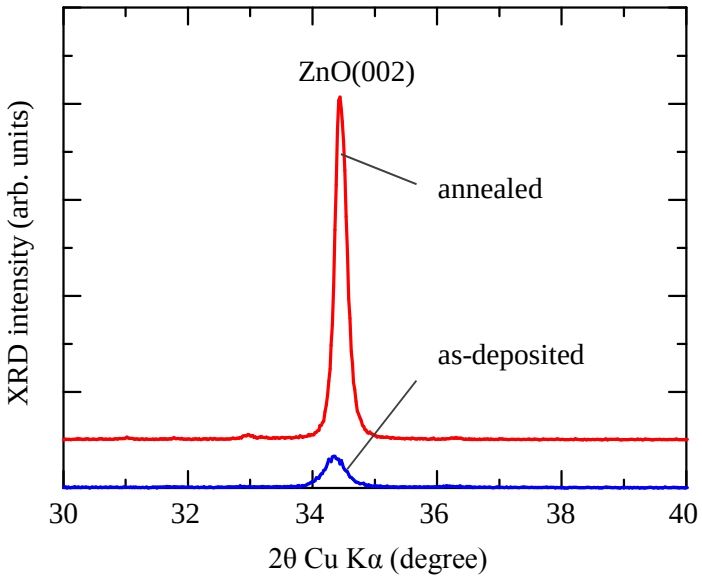

Fig. 6.5 XRD patterns of the as-deposited and nanostructured ZnO films.

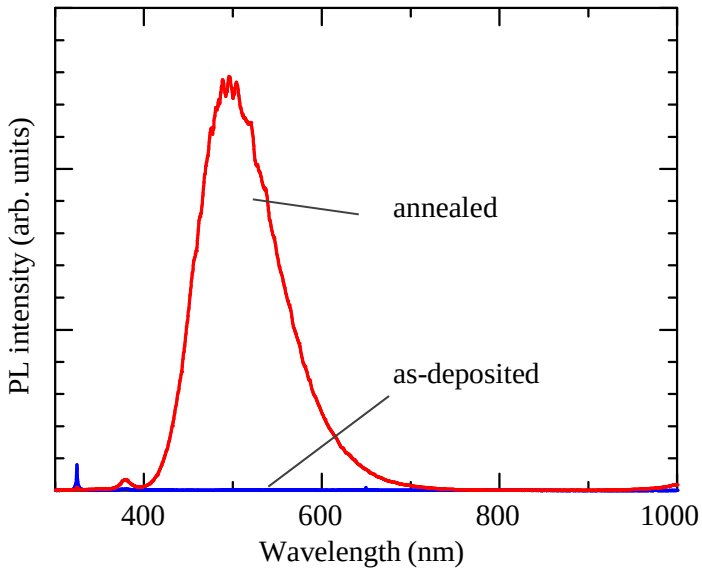

Fig. 6.6 PL spectra of as-deposited and nanostructured ZnO films.

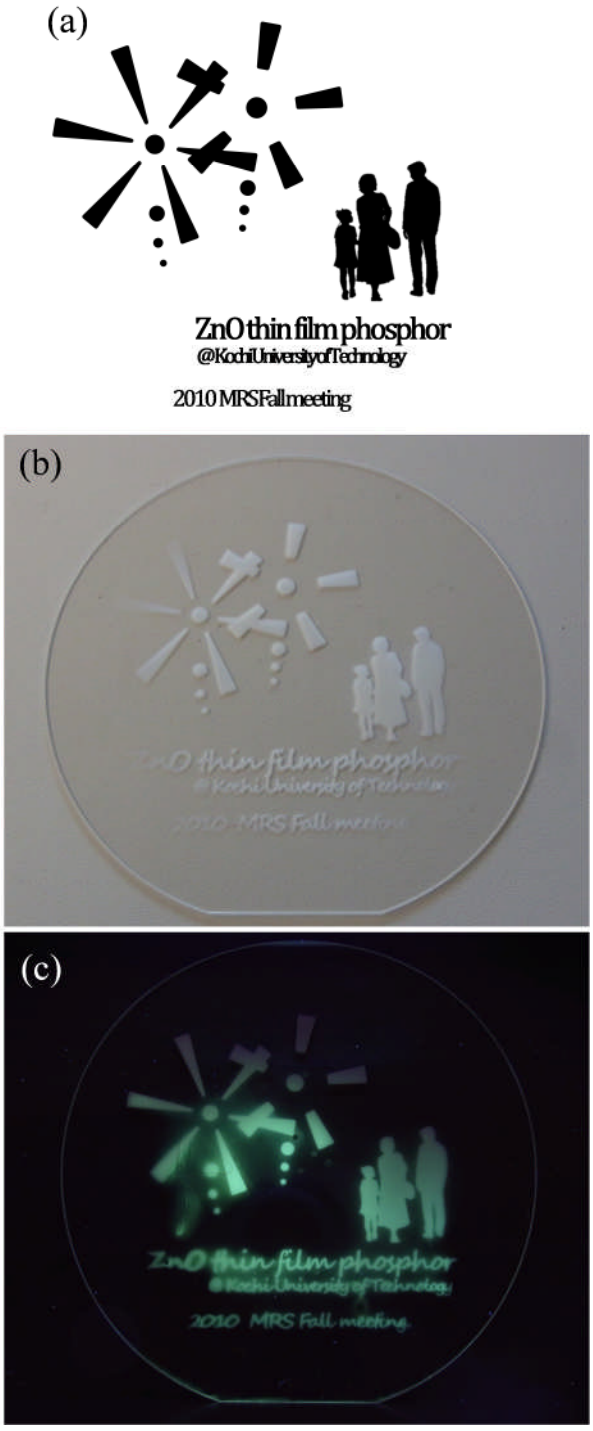

Fig 6.7 (a) the mask image for ZnO thin film phosphor fabrication, (b) patterned ZnO thin film annealed in reducing gas, (c) patterned ZnO thin film phosphor excited by UV lamp with the wavelength of 365 nm and excitation power of 6 W.

6.5 References

[1] Y. Ohya, T. Niwa, T. Ban, and Y. Takahashi, Jpn. J. Appl. Phys., 40 (2001) 297.

[2] R.L. Hoffman, B.J. Norris, and J.F. Wager, Appl. Phys. Lett., 82 (2003) 733.

[3] B.J. Norris, J. Anderson, J.F. Wager, D.A. Keszler, J. Phys. D: Appl. Phys., 36 (2003) L105.

[4] J. Nishii, F.M. Hossain, S. Takagi, T. Aita, K. Saikusa, Y. Ohmaki, I. Ohkubo, S. Kishimoto, A. Ohtomo, T. Fukumura, F. Matsukura, Y. Ohno, H. Koinuma, H. Ohon, and M. Kawasaki, Jpn. J. Appl. Phys., 42 (2003) L347.

[5] S. Masuda, K. Kitamura, Y. Okumura, and S. Miyatake, J. Appl. Phys., 93 (2003) 1624.

[6] J.E. Lilienfeld, U.S. Patent 1745175 (1930).

[7] Y. Kuo, “Thin Film Transistors – Materials and Processes”, Kluwer Academic Publishers (2004).

[8] F. Garnier, Adv. Mat., 2 (1990) 592.

[9] C.R. Kagan and P. Andry, “Thin-Film Transistors”, Marcel Dekker, Inc., New York (2003).

[10] K. Morimoto, and T.L. Pykosz, Trend in vacuum fluorescent display, in Electronic Display and Information Systems and On-board Electronics, P103, 820264 (1982) 69.

[11] M. Ohkubo, Japanese Patent Publication (Kokoku) 45-20223 (1970).

[12] C.H. Aaronson, H. Amekura, Y. Sato, and N. Kishimoto, J. Appl. Phys., 109 (2011) 024506.

Chapter 7

Conclusions

ZnO and its related materials thin films including ZnO:Mg films with different Mg ratio and multiple layers, were fabricated using RF magnetron sputtering system. The synthesis of ZnO and its related materials thin films were investigated in detail under the various deposition conditions (gas ratio, pressure, and power) on different substrates at low temperature. Their structural, optical, and electrical properties were also evaluated. It was found that the properties of ZnO related materials thin films were highly dependent on the deposition conditions. The crystallinity and the band gap of thin films can be simply adjusted by controlling the deposition parameters during sputtering processes. Nanostructured ZnO thin films were formed by single post-treatment in reducing ambient and a novel multiple post-treatment processes in reducing ambient combining with oxygen annealing. The density and shape of well-arrayed ZnO nanostructures can be controlled by modulating post-treatment conditions.

For the applications of ZnO related semiconductors, I focus on ZnO related thin films for TFTs application and nanostructured ZnO thin films phosphor due to its particular advantages. ZnO related materials thin film phosphor potentially applied for vacuum fluorescent display were discussed. The main conclusions of this thesis are summarized as follows:

I. Effects of deposition parameters on structural and optical properties of ZnO thin films

ZnO thin films were deposited onto quartz glass substrates by RF magnetron sputtering. The structural and optical properties of as-deposited ZnO films were strongly dependent on the Ar/O_2 ratio, puttering power, and deposition pressure.

1) The effects of gas ratio on the properties of ZnO films were investigated. The ZnO films had a hexagonal wurtzite structure and the crystallinity improved whereas the *c*-axis crystalline size increases with the increase of oxygen ratio. The film resistivity decreases with decreasing of oxygen ratio. The optical absorption edge is found to shift to the shorter wavelength with the increase of the oxygen ratio. Based on the investigation of properties of ZnO films deposited under different Ar/O_2 ratio, the Zn-rich or O-rich thin films can be adjusted simply during sputtering.
2) The deposition power was varied from 60 to 240 W at an interval of 60 W during sputtering process. The crystallinity of films improved whereas the *c*-axis crystalline size decreases with the increase of sputtering power. All the ZnO thin films show about 80% optical transmissions in the visible region. Based on the investigation of properties of ZnO films

deposited under different sputtering power, the crystallinity and band gap of thin films can be adjusted simply during sputtering.

3) The deposition pressure was varied from 1 to 7 Pa at an interval of 2 Pa. The *c*-axis crystalline size increases with the increase of sputtering pressure. The optical absorption edge is found to shift to the shorter wavelength with the increase of the sputtering pressure. The results indicate that the band gap of thin films can be adjusted from 3.244 to 3.271 eV with sputtering pressure increase from 1 to 7 Pa.

II. Fabrication and characterization of ZnO:Mg thin films

ZnMgO thin films with different Mg concentrations had been deposited on quartz or silicon substrates by using RF magnetron sputtering.

1) $Zn_{1-x}Mg_xO$ (x = 0.3) thin films were prepared under deposition pressure from 1 to 9 Pa at an interval of 2 Pa. The crystal structure varied from hexagonal wurtzite to cubic rock-salt with decreasing deposition pressure from 9 to 1 Pa. Corresponding to the Mg concentration in the ZnMgO thin films increased from 0.467 to 0.531 due to the scattering effect. Furthermore, the band gap of the ZnMgO films increased from 4.30 to 5.23 eV significantly while the deposition pressure decreased.
2) $Zn_{1-x}Mg_xO$ (x = 0.1) thin film was deposited on p-type Si (100) substrate. After the preparation, the effects of post-annealing in H_2/N_2, N_2, or O_2 atmospheres on structural and optical properties of ZnMgO films were studied. The most improved crystallinity was found from the film annealed in H_2/N_2 ambient at 500 °C for 5 h, corresponding to the increased grain size. Moreover, the PL intensity with peak range around 520-620 nm was increased remarkably for the film annealed in reducing gas.
3) $Zn_{1-x}Mg_xO$/ZnO (x = 0.1) thin film were prepared on p-type Si (100) substrate with ZnO thin film as buffer layer. The hexagonal naorods were formed vertically on the ZnMgO after annealing in a reducing ambient at a low temperature. The crystallinity of ZnMgO/ZnO was improved due to Mg substitution in the ZnO film. A broaden PL emission peak from 480 to 700 nm was observed from ZnMgO/ZnO multiple layer.

III. Fabrication and characterization of nanostructured ZnO thin films

Based on ZnO thin films fabrication, the novel post-treatment processes were carried out on forming nanostructured ZnO thin films. The effects of different post-treatment processes on the structural and optical properties on nanostructured ZnO thin films were investigated.

1) Nanostructured ZnO thin films were formed by optimizing the post-treatment time in reducing gas. The highest green emission peak centered at 497 nm is obtained from the ZnO nanostructures annealed for the optimum annealing time of 5 h. Therefore, it can assume that the much more oxygen vacancies might be produced and existed on the ZnO

nanostructures. XRD measurements indicated that the ZnO thin film annealed for optimizing annealing time of 5 h also exhibited the better crystallinity.

2) ZnO nanorods from different thickness films were formed by annealing ZnO films in reducing ambient at a low temperature. The quantity of ZnO nanorods increased with the thickness increased, which was due to the quantity of un-react zinc atoms introduced by deposition process. PL spectra obtained from annealed films exhibited an intense deep level emission with a peak centered at about 500 nm. The strongest green luminescence was observed from the annealed film with the thickness of 1000 nm, which was attribute to the dense ZnO nanostructures which supplies much larger surface area where more oxygen vacancies existed.
3) In order to further control and produce well-arrayed ZnO nanostructures, we developed a novel low-temperature multi-annealing process, which combines a reducing annealing process and oxygen annealing process. The effects of multi-annealing processes on forming ZnO nanostructures on the ZnO thin films were investigated. Well-arrayed ZnO nanostructures with the appearance of fluted reverse cones capped with hexagonal heads were obtained via a novel multi-annealing process. The crystallinity of ZnO nanostructures was also improved. ZnO nanorods with oxygen vacancies contribute to green luminance after treatment in reducing gas. Oxygen annealing between the two reducing gas annealing processes contributed to efficiently introduce the oxygen into the ZnO thin films, leading to ZnO nanostructures regrown quickly. Therefore, the multi-annealing process is an efficient method to form well-arrayed ZnO nanostructures.
4) Based on the results exhibited above, the well-arrayed ZnO nanostructures could be fabricated controllably on the ZnO film after multiple treatments at a low temperature. In order to optimize the processes for forming nanostructured ZnO thin film with intense visible luminescence, the annealing time of first step in multi-annealing processes was modulated. It was confirmed that the first step in the reducing ambient was most important process for nanostructured ZnO thin film formation. The optimized condition for form the nanostructure was found for the annealing in reducing ambient first for 5 h. The ZnO nanostructures with uniform hexagonal head with diameter of 600 nm and average height of 1200 nm were formed after multi-step annealing. The intense PL emission peak centered at 505 nm was obtained from the well-arrayed ZnO nanostructures.

IV. Device demonstration of obtained ZnO thin fim and nanostructures

Two kinds of potential applications were investigated based on the ZnO semiconductor. ZnO thin film was applied into TFT and nanostructured ZnO thin film potentially treated for VFD, respectively. The characterization of as-deposited and annealed ZnO thin film were evaluated.

1) Bottom-gate TFT was fabricated based on the ZnO thin film as the channel layer, which was

carried out with relatively simple processing technology. The results indicated that ZnO TFT displayed good performance. It indicates that combination of transparency, high channel mobility and low temperature processing makes the ZnO TFT a promising low cost optoelectronic device.

2) In order to overcome the remained problems of powder phosphor and lower the fabrication cost, we developed a novel technique for fabricating ZnO thin film phosphor on the glass substrate directly at a low temperature of 450 ^{o}C. After the preparation of ZnO thin film, the patterned thin film was easily and precisely formed on large area by wet etching method.

Therefore, it is possible to apply ZnO-related materials thin films and nanostructured ZnO thin films for optoelectronic devices.

List of publications

(A) Reviewed journal papers

Fist author:

1) Well-arrayed ZnO nanostructures formed by multi-annealing processes at low temperature
Dapeng Wang, Zeming Li, Toshiyuki Kawaharamura, Mamoru Furuta, Tadashi Narusawa, Chaoyang Li
Physica Status Solidi C, 9 (2012) 194-197.

2) Influence of sputtering pressure on band gap of $Zn_{1-x}Mg_xO$ thin films prepared by radio frequency magnetron sputtering
Dapeng Wang, Chaoyang Li, Toshiyuki Kawaharamura, Mamoru Furuta, Takashi Hirao, Tadashi Narusawa
Journal of Vacuum Science and Technology B, 29 (2011) 051205-1-051205-4.

3) Thickness effects on the structural and optical properties of sputtered ZnO films
Dapeng Wang, Toshiyuki Kawaharamura, Mamoru Furuta, Tadashi Narusawa, Chaoyang Li
Surface and Coatings Technology, (Under review)

Co-author:

4) Study on oxygen source and its effect on film properties of ZnO deposited by radio frequency magnetron sputtering
Yudai Kamada, Mamoru Furuta, Takahiro Hiramatsu, Toshiyuki Kawaharamura, **Dapeng Wang**, Shin-ichi Shimakawa, Chaoyang Li, Shizuo Fujita, and Takashi Hirao
Applied Surface Science, 258 (2011) 695-699.

5) Photocurrent and Persistent Photoconductivity in Zinc Oxide Thin-Film Transistors under UV-light Irradiation
Mamoru Furuta, Yudai Kamada, Mutsumi Kimura, Shin-ichi Shimakawa, Toshiyuki Kawaharamura, **Dapeng Wang**, Chaoyang Li, Shizuo Fujita, and Takashi Hirao
Japanese Journal of Applied Physics, 50 (2011) 110204-1-110204-3.

6) Photo-leakage current of TFTs with ZnO channels formed at various oxygen partial pressures under visible light irradiation
Shin-ichi Shimakawa, Yudai Kamada, Toshiyuki Kawaharamura, **Dapeng Wang**, Chaoyang Li, Shizuo Fujita, and Takashi Hirao, Mamoru Furuta
Japanese Journal of Applied Physics, (accepted)

(B) International and domestic conferences

International conferences with proceeding as first author:

1) Effects of thickness on the optical properties of zinc oxide films prepared by radio frequency magnetron sputtering (Oral, PA28O, pp. 43-44)
Dapeng Wang, Chaoyang Li, Toshiyuki Kawaharamura, Mamoru Furuta, Takashi Hirao, Tadashi Narusawa
The 11th Plasma-based Ion Implantation and Deposition (PBIID 2011)
Sept. 8-12, 2011. Harbin, China.

2) Effects of Thickness on the Structural and Optical Properties of ZnO:Zn Thin Films Prepared by Radio Frequency Magnetron Sputtering (Oral, pp. 173-176)
Dapeng Wang, Chaoyang Li, Toshiyuki Kawaharamura, Mamoru Furuta, Takashi Hirao, Tadashi Narusawa
The 3rd International Symposium on Frontier Technology (ISFT 2011)
July 29-30, 2011. Kochi University of Technology, Kochi, Japan.

3) Effects of multiple post-treatments on the structural and optical properties of ZnO thin films (Poster - P2. 17, pp. 84-85)
Dapeng Wang, Chaoyang Li, Toshiyuki Kawaharamura, Mamoru Furuta, Takashi Hirao, Tadashi Narusawa
The 38th International Symposium on Compound Semiconductors (ISCS 2011)
May 22-26, 2011. Berlin, Germany, Maritim proArte Hotel.

4) Low Temperature Post-annealing Effects on Structural and Optical Properties of $Zn_{0.9}Mg_{0.1}O$ Thin Film Prepared by Radio Frequency Magnetron Sputtering (Poster- P-24, pp. 187-190)
Dapeng Wang, Chaoyang Li, Toshiyuki Kawaharamura, Tokiyoshi Matsuda, Mamoru Furuta, Takashi Hirao, Tadashi Narusawa

The Seventeenth International Workshop on Active-Matrix Flatpanel Displays and Devices (AM-FPD 10)
July 5-7, 2010. Tokyo Institute of Technology O-okayama Campus, Tokyo, Japan

5) Effects of Deposition Pressure on Structural and Optical Characteristics of ZnMgO Thin Films Prepared by Radio Frequency Magnetron Sputtering (Poster-Mop56, pp. 58)
Dapeng Wang, Chaoyang Li, Toshiyuki Kawaharamura, Tokiyoshi Matsuda, Takashi Hirao,Tadashi Narusawa
The 37th International Symposium on Compound Semiconductors (ISCS 2010)

International conferences with proceeding as co-author:

6) Amorphous InGaZnO Thin-Film Transistor with solution-based atmospheric pressure deposited IGZO/AlOx Gate Dielectric Stack (Oral)
Mamoru Furuta, Toshiyuki Kawaharamura, **Dapeng Wang**
8th International Thin-Film Transistor Conference (ITC 2012).
Jan. 30-31, 2012, Lisbon, Portugal.

7) Photo-induced Bias Instability of Zinc Oxide Thin-Film Transistors (Poster)
Shin-ichi Shimakawa, **Dapeng Wang**, Mamoru Furuta
8th International Thin-Film Transistor Conference (ITC 2012).
Jan. 30-31, 2012, Lisbon, Portugal.

8) Multiple-annealing Process Effects on Fabrication of Well-aligned ZnO Nanostructures (Poster-PHp-7, pp. 763-766)
Chaoyang Li, **Dapeng Wang**, Toshiyuki Kawaharamura, Zeming Li, Mamoru Furuta
The 18th International Display Workshops (IDW'11)
Dec. 7-9, 2011. Nagoya Congress Center, Nagoya, Japan

9) Development of High Photoluminescence Nanostructured ZnO Thin Film Phosphor at Low Temperature (No. 65-3, pp.)
Chaoyang Li, **Dapeng Wang**, Toshiyuki Kawaharamura, Mamoru Furuta, Akimitsu Hatta
11th International Meeting on Information Display (IMID 2011)
Oct. 11-15, 2011. Kintex, Seoul, Korea.

10) Effect of annealing on the structural and photoluminescence properties of ZnO/$Zn_{0.9}Mg_{0.1}O$ heterostructures (No.Ph3-3, pp.)
Chaoyang Li, **Dapeng Wang**, Toshiyuki Kawaharamura, Hiroshi Furuta, Takahiro Hiramatsu, Mamoru Furuta, Takashi Hirao
The 17th International Display Workshops (IDW'10)
Dec. 1-3, 2010. Fukuoka International Congress Center, Fukuoka, Japan.

11) Effects of high pressure water vapor annealing on photoluminescent and structural properties of nano structured ZnO/ZnMgO multiple layers prepared by radio frequency magnetron sputtering (No.16-1, pp. 106-107)
Chaoyang Li, **Dapeng Wang**, Toshiyuki Kawaharamura, Hiroshi Furuta, Takahiro Hiramatsu, Mamoru Furuta, Takashi Hirao
10th International Meeting on Information Display (IMID 2010)
Oct. 11-15, 2010. Kintex, Seoul, Korea.

12) Characterization of ZnMgO/ZnO Thin Films Prepared by Radio Frequency Magnetron Sputtering (Poster-P-23, pp. 183-186)
Chaoyang Li, **Dapeng Wang**, Toshiyuki Kawaharamura, Mamoru Furuta, Takashi Hirao
The Seventeenth International Workshop on Active-Matrix Flatpanel Displays and Devices (AM-FPD 10)
July 5-7, 2010. Tokyo Institute of Technology O-okayama Campus, Tokyo, Japan.

Domestic conferences as first author

13) ZnO 薄膜を還元雰囲気下で熱処理した時の表面ナノ構造及び PL 特性の時間依存
Effects of annealing time on the surface structural & photoluminescent properties of ZnO thin film
Dapeng Wang, Chaoyang Li, Toshiyuki Kawaharamura, Mamoru Furuta, Takashi Hirao, Tadashi Narusawa
The 58th Spring Meeting of Applied Physics Academic Meeting
Mar. 24-27, 2011. Kanagawa Institute of Technology, Kanagawa, Japan.

14) ガラス基板上へのパターン化に成功した酸化亜鉛(ZnO)薄膜蛍光体
～スパッタリングによる薄膜成長、ウェットエッチング、熱処理を経て～
Precisely patterned Zinc Oxide (ZnO) thin film phosphor fabricated directly on glass substrate
－after thin film fabrication with sputtering, wet etching, annealing－

Dapeng Wang, Toshiyuki Kawaharamura, Chaoyang Li, Takashi Hirao
映情学技報, Vol. 35, No. 4, pp. 1-3. (映像情報メディア学会技術報告) (発光型/非発光型ディスプレイ合同研究会、高知)
Jan. 28-29, 2011. Kochi University of Technology, Kami, Japan.

15) 還元雰囲気熱処理を施した酸化亜鉛薄膜の膜厚と構造及び光学特性の関係
The thickness of ZnO thin film with post treatment in reduction condition effects on structural and optical properties
Dapeng Wang, Chaoyang Li, Toshiyuki Kawaharamura, Tokiyoshi Matsuda, Mamoru Furuta, Takashi Hirao, Tadashi Narusawa
The 71st Fall Meeting of Applied Physics Academic Meeting
Sep. 14-17, 2010. Nagasaki University Bunkyo Campus, Nagasaki, Japan.

Domestic conferences as co-author

16) ミスト CVD 法による IGZO TFT の作製
Fabrication of IGZO TFT prepared by mist CVD
Toshiyuki Kawaharamura, **Dapeng Wang**, Giang T. Dang, Mamoru Furuta
Thin film materials & devices meeting. (薄膜材料デバイス研究会、第 8 回研究集会「新しいデバイス材料」)
Nov. 4-5, 2011. 龍谷大学アバンティ響都ホール１００年会館（京都市）、日本。

17) ZnO 薄膜蛍光体の形成とその発光中心導入過程
Fabrication of ZnO thin film phosphot and its luminescence center
Chaoyang Li, Tokiyoshi Matsuda, Toshiyuki Kawaharamura, **Dapeng Wang**, Hiroshi Furuta, Mamoru Furuta, Keiji Ichinomiya, Yoichiro Nakanishi, Takashi Hirao
Thin film materials & devices meeting. (薄膜材料デバイス研究会、第 7 回研究集会「薄膜材料デバイスの理解と解析」)
Nov. 5-6, 2010. 奈良１００年会館（奈良市）、日本。

(C) Best paper award

1) ミスト CVD 法による IGZO TFT の作製
Fabrication of IGZO TFT prepared by mist CVD
Toshiyuki Kawaharamura, **Dapeng Wang**, Giang T. Dang, Mamoru Furuta
Thin film materials & devices meeting. (薄膜材料デバイス研究会、第 8 回研究集会「新しいデバイス材料」)
Nov. 4-5, 2011. 龍谷大学アバンティ響都ホール１００年会館（京都市）、日本。

2) ZnO 薄膜蛍光体の形成とその発光中心導入過程
Fabrication of ZnO thin film phosphot and its luminescence center
Chaoyang Li, Tokiyoshi Matsuda, Toshiyuki Kawaharamura, **Dapeng Wang**, Hiroshi Furuta, Mamoru Furuta, Keiji Ichinomiya, Yoichiro Nakanishi, Takashi Hirao
Thin film materials & devices meeting. (薄膜材料デバイス研究会、第 7 回研究集会「薄膜材料デバイスの理解と解析」)
Nov. 5-6, 2010. 奈良１００年会館（奈良市）、日本。